Two–particle azimuthal correlation in d+Au and p+p collision at $\sqrt{s_{NN}}$=200 GeV in STAR

Azimutale twee–deeltjescorrelaties in d+Au en p+p botsingen met $\sqrt{s_{NN}}$=200 GeV in STAR

(met een samenvatting in het Nederlands)

Proefschrift

ter verkrijging van de graad van doctor aan de Universiteit Utrecht op gezag van de rector magnificus, prof.dr. J.C. Stoof, ingevolge het besluit van het college voor promoties in het openbaar te verdedigen op maandag 8 september 2008 des ochtends te 10.30 uur

door

Federica Benedosso

geboren op 1 maart 1978 te Conegliano, Italië

Promotor: Prof. dr. Th. Peitzmann

Co–promotor: Dr. A. Mischke

Contents

Chapter 1

Heavy–ion physics

Nuclei are built from protons and neutrons which themselves are composed of quarks and gluons. The strong force is responsible for binding protons and neutrons together in nuclei. Quarks have never been observed in isolation, but only in quark–antiquark pairs (mesons) or triplets (baryons). While isolated quarks carry a color charge, mesons and baryons are color neutral.

Colliding heavy ions permits to reach conditions of density and temperature typical of the universe in the first microseconds after the Big Bang.

1.1 The Standard Model and Quantum Chromodynamics

Hadrons are particles subject to the strong interaction. In the standard model of particle physics, hadrons consist of strongly interacting quarks. The standard model knows also the existence of other point–like particles like leptons and force mediators, listed in table 1.1. Quarks carry *color*, a property that plays the role of "charge" in the strong interaction.

Quantum Chromodynamics (QCD) [2] is the quantum field theory of the strong interaction. Unlike the electric charge, which is a simple scalar, the color charge is a SU(3) group representation. Quarks (antiquarks) belong to the basic triplet (antitriplet) representation, while gluons carry one of eight color charges in the conjugate representation. Since gluons carry charge, the color fields constituted by them interact with other color fields. This makes it very difficult, in general, to solve problems in QCD.

In QCD, the coupling strength depends on the interaction distance, which is equivalent to the inverse of the transverse transferred momentum. For small distances, or large momentum transfers (*hard processes*), the coupling is weak: this property is referred to as asymptotic freedom. In this case, the

	Quarks						Leptons		
Flavor	Mass (GeV/c^2)	Q	S	C	B	T		Mass (GeV/c^2)	Q
Down, d	0.008	$-\frac{1}{3}$	0	0	0	0	e	0.0005	-1
Up, u	0.004	$+\frac{2}{3}$	0	0	0	0	ν_e	$<3{\cdot}10^{-9}$	0
Strange, s	0.15	$-\frac{1}{3}$	-1	0	0	0	μ^-	0.105	-1
Charm, c	1.2	$+\frac{2}{3}$	0	1	0	0	ν_μ	< 0.00019	0
Bottom, b	4.7	$-\frac{1}{3}$	0	0	-1	0	τ^-	1.8	-1
Top, t	174	$+\frac{2}{3}$	0	0	0	1	ν_τ	< 0.018	0

Table 1.1: The flavor quantum numbers of three different generations of quarks and leptons. Q, S, C, B, T are charge, strangeness, charm, beauty and truth. Free quarks are not seen and the mass represents the current calculated mass. Antiparticles have opposite quantum numbers. Each flavor of quark comes in three colors (red, green and blue) [1].

interaction can be treated using perturbation theory. On the other side, at large distance or small transferred momentum, the coupling is strong and higher order processes involving the exchange of more than one gluon contribute with a magnitude similar to the single gluon exchange, therefore, a perturbative approach is no longer suitable.

The potential between colored objects increases with distance, thus, an infinite amount of energy is needed to separate two colored objects. For this reason all colored objects are confined into color–neutral states. This property is called *confinement*. To study the coupling at large distance, lattice gauge theory, based on a discrete space–time lattice, is used. However, the calculations on the lattice are limited to systems in thermodynamic equilibrium and with baryon densities much lower than in nuclear matter and they provide only a first approximation for the real case.

Since hard processes can be calculated in perturbative QCD (pQCD), they are both a unique probe for matter constituents and a testing ground for QCD validity. In these processes, *partons* (quarks and gluons) carrying a color charge will move apart with a large relative momentum. Momentum conservation will make the partons propagate back–to–back in the plane perpendicular to the collision axis. Due to color confinement the partons will fragment into jets, whose propagating directions are also back–to–back. Perturbative QCD is in agreement with jet p_T spectra from hard processes as shown in figure 1.1.

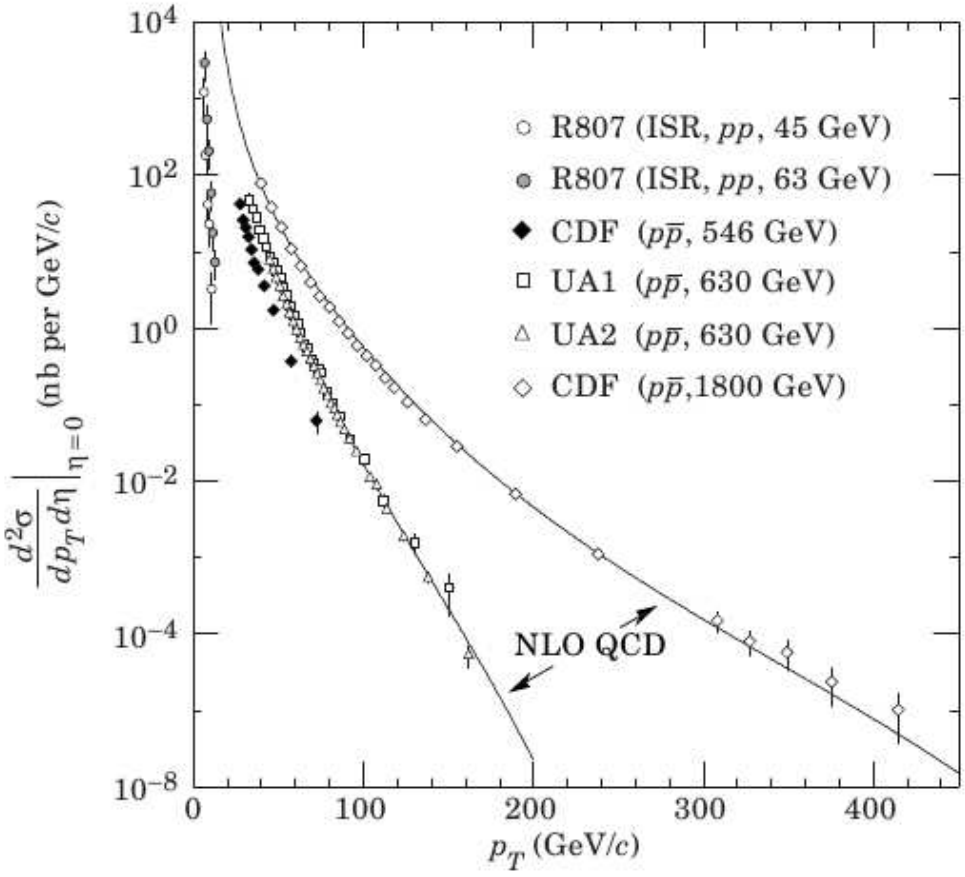

Figure 1.1: Differential cross sections for the observation of a single jet of pseudorapidity η=0 as a function of the jet transverse momentum. The lines through the data are next-to-leading order (NLO) QCD curves for 630 GeV and 1800 GeV $p + \bar{p}$ collisions [1].

1.2 Quark–Gluon Plasma

Isolated quarks have never been observed (*confinement*). Crudely spoken, a deconfined quark is one that can move in a volume much larger than the volume of a proton. QCD predicts [3] that, at a sufficiently large temperature and density, a regime can be reached where quarks and gluons become deconfined, so that color degrees of freedom become manifest over nuclear, rather than merely nucleonic, volumes. This state of the matter in which the quarks are deconfined is called Quark–Gluon Plasma (QGP).

A deconfined system could exist at much higher density than the regular nuclear matter, such as in neutron stars, where gravity can compress the

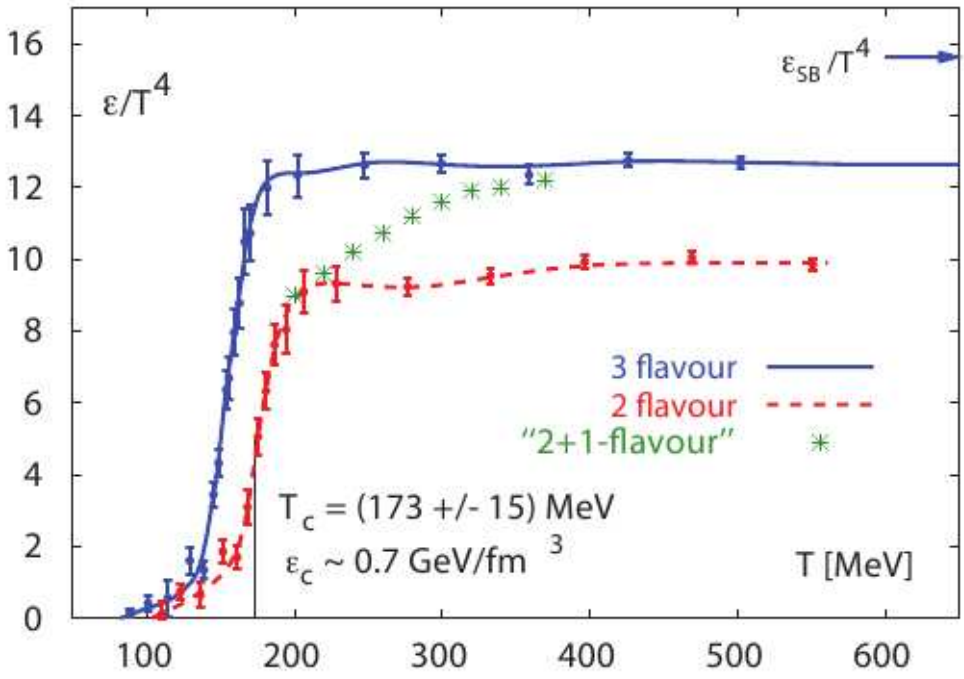

Figure 1.2: Lattice QCD calculations for energy density (ε) divided by temperature (T) to the 4^{th} power versus temperature. ε_{SB}/T^4 is the Stephan-Boltzmann-Limit for an ideal gas. The two different curves are for 2 and 3 light quark flavors, while the stars are an estimate for realistic quark masses [3].

nucleons to the point where they start to overlap. Hence, it is not possible to assign anymore a parton to a specific nucleon. It is believed that in the early stages of the universe a similar condition was reached as a consequence of the high temperature or high density.

For a system of quarks and gluons in thermodynamic equilibrium, the value of energy density as a function of temperature has been calculated using lattice QCD. The system exhibits a phase transition from a hadron gas to a phase where the confinement of quarks and gluons into hadrons vanishes, as shown in figure 1.2. The phase transition is expected to happen at a temperature of about 170 MeV and at an energy density of about 0.7 GeV/fm^3.

A schematic phase diagram of strongly interacting matter is shown in figure 1.3. It shows the phases as a function of the temperature and the baryo–chemical potential μ_B of a system. The baryo–chemical potential of

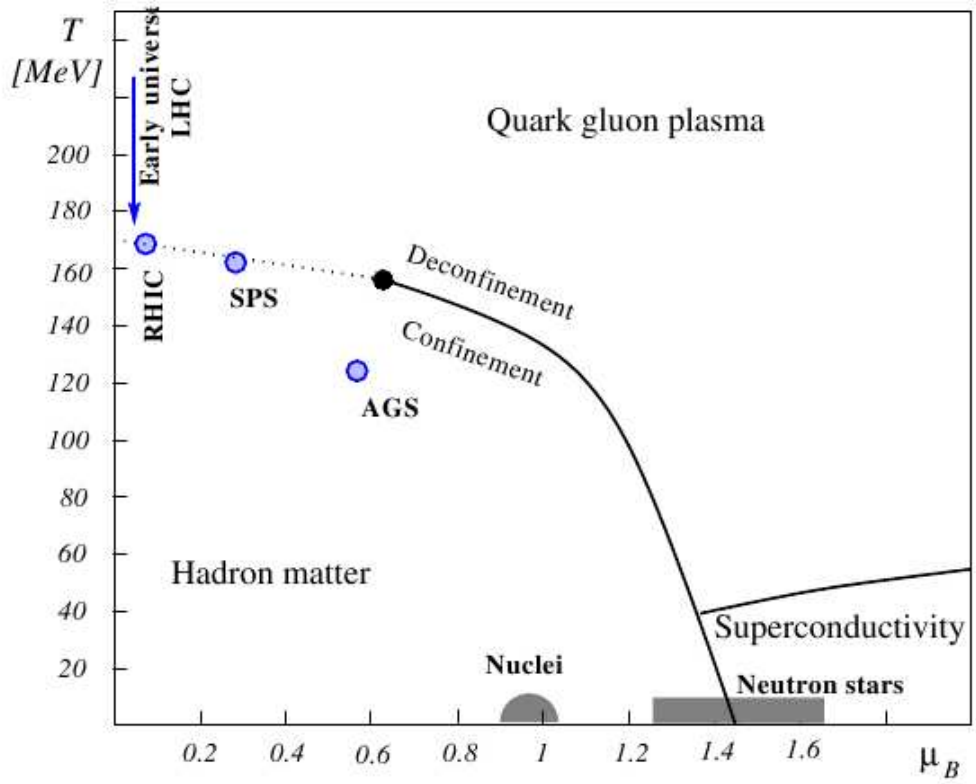

Figure 1.3: Schematic phase diagram of QCD [7].

normal nuclear matter at low temperatures is $\mu_B = m_N \approx 1$ GeV*. For high temperatures or much higher baryon densities, a phase transition from hadronic matter to a Quark–Gluon Plasma is expected [5]. This phase transition has been studied for $\mu_B = 0$ MeV using lattice gauge theory, and it was found to be a rapid cross over. This seems to persist for slightly higher values of μ_B up to a critical point, when it changes through a first order phase transition [6].

After the Big Bang, the universe was expanding and cooling down rapidly. Up to $\sim$10 μs the energy density was still much higher than 1 GeV/fm^3 and, thus, the predominant form of matter could not have been hadronic matter but rather a Quark–Gluon Plasma. The trajectory the matter in the universe was going through at that stage is indicated by the arrow in the top left corner of the phase diagram (figure 1.3). Nowadays a Quark–Gluon Plasma might

*The mass of a nucleon is $m_N = 938.272029 \pm 0.000080$ for protons and $m_N = 939.565360 \pm 0.000081$ for neutrons [4]

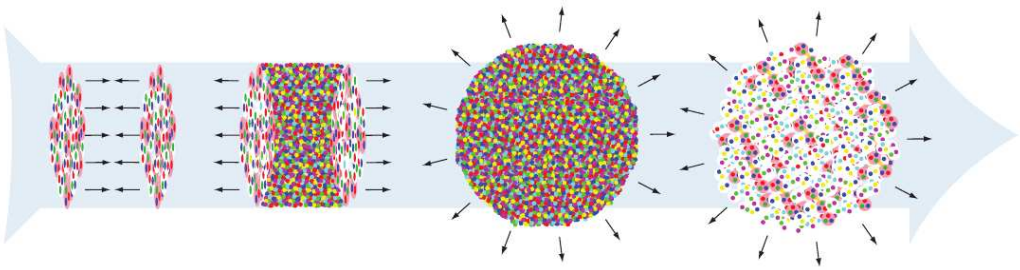

Figure 1.4: Schematic view of a heavy ion collision at ultra–relativistic energies. The different stages of the collision are shown: the approaching nuclei, the interpenetration and creation of a new matter phase, the expansion of a quark gluon plasma, the expansion of hadronic matter.

still be found at the core of compact astronomic objects like neutron stars, where the baryon density is very high and the temperature very low. This is indicated in the lower right corner of the phase diagram (c.f. figure 1.3).

1.3 Heavy Ion Collisions

In a high energy heavy ion collision, the colliding nuclei are relativistically contracted and have the shape of flat discs (figure 1.4). The highest energy density is reached when the two discs overlap. After that, a multitude of particles is created. Being the participating entities and the interactions between them are a number large enough to allow for the use of thermodynamics terminology. Size and kinetic energy of the accelerated nuclei determine the initial conditions of the hot and dense state of matter which is created when they collide.

Several processes contribute to particle production in the collision. In the earliest moments of the collision, the nucleons of the two incoming nuclei collide as if they were independent particles. It is in this phase that hard scatterings occur and produce heavy quarks and the most energetic partons that will later fragment into jets. Multiple collisions among nucleons make them lose kinetic energy creating a high energy density region, filled with quarks and gluons. The system tends, after this, to a thermal equilibrium, and if the energy density is high enough the QGP phase is reached. The energy density causes a pressure which makes the system expand and cool down. At some point, the temperature drops below the critical one, and partons cannot remain deconfined anymore. The following hadronization still

allows for interactions among the newly created particles, until the medium cools down even more and the hadrons stop interacting and leave the region.

Different properties of the system can be probed at different stages of the collision. Since hadrons interact until the kinetic freeze out of the system, it is difficult to obtain experimental information on the early stages after thermalization and only model descriptions are available. Never the less, several properties of the QGP can be studied by the observation of the final state particles.

Elliptic flow

In non–central heavy–ion collisions the anisotropy of pressure gradients inside the system causes an anisotropy in the momentum distribution. The interaction region has an elliptical shape in the plane perpendicular to the beam direction. Particles have a higher momentum along the minor axis of the ellipse (momentum anisotropy), thus, the spatial anisotropy is reduced until it disappears. As soon as it is gone, the momentum anisotropy does not change any longer, and it should be preserved in the final state of the collision. In this way the *elliptic flow* is a probe for the early stages of the collision.

The anisotropy of particle production is usually parameterized by the coefficients v_n of the Fourier decomposition of the azimuthal distribution of particles relative to the reaction plane. At mid–rapidity, the first azimuth–dependent term v_1 vanishes. The first non–trivial term is then v_2, which is often referred to as elliptic flow. At low transverse momenta, the asymmetry is well described by hydrodynamical calculations, that treat the medium as an expanding fluid [8].

Due to the asymmetry of the hot and dense phase in the collision, energetic partons created in hard initial scatterings will traverse different path lengths to leave the medium. This path length depends on the emission angle relative to the reaction plane. The average energy loss of a parton in the QGP is then a function of the azimuthal angle, which introduces further anisotropies in the production of high–p_T particles, apart from hydrodynamical flow. The energy loss of these partons can be combined with hydrodynamical calculations, to account for the evolution of the hot phase, and the path length of energetic partons inside this phase, to predict the anisotropy of high–p_T particle production. The energy loss leads to a smaller v_2 at high–p_T compared to a pure hydrodynamical calculation [9].

Particle spectra and high–p_T physics

Inclusive hadron spectra describe the late stages of the collision. The ratios of different particle types are sensitive to the chemical freeze out, after which the types of the particles are fixed. The shape of the transverse momentum distribution is sensitive to the thermal freeze out, after which particle momenta no longer change.

Nuclear effects on hadron production have been studied in d+Au and Au+Au collisions through comparison to the p+p spectrum using the ratio

$$R_{AB} = \frac{d^2N/dp_T d\eta}{T_{AB} d^2\sigma^{pp}/dp_T d\eta} \tag{1.1}$$

where $d^2N/dp_T d\eta$ is the differential yield per event in the nuclear collision A+B, $T_{AB} = \langle N_b^C \rangle / \sigma_{inel}^{pp}$ describes the nuclear geometry, and $d^2\sigma^{pp}/dp_T d\eta$ for p+p is the measured p+p differential cross section [10]. In the absence of nuclear effects, hard processes are expected to scale with the number of binary collisions (R_{AB}=1).

The hard scattering in the early stages of heavy ion collisions produces particles with momentum high enough to traverse the medium, while it is still at a high energy density. Particles interact with the medium transferring part or all their energy and momentum to the medium before leaving it. Finally, they fragment into a jet of hadrons. In heavy–ion collisions a complete jet reconstruction is not possible yet, due to the large particle multiplicity. It is therefore more convenient to use high transverse momentum (p_T) to probe the initial parton.

The production of high-p_T particles occurs only at large momentum transfers. In this kinematic region a good reference from perturbative QCD calculations and data from p+p collisions is available. A comparison of heavy–ion and p+p collisions can, therefore, isolate effects that are specific to the conditions found in presence of heavy nuclei.

R_{AB} for central Au+Au collisions exhibits a large suppression in hadron production at high p_T [11]. This suppression is attributed to medium induced parton energy loss (jet quenching) because the fragmentation of hard partons is the primary source of these high–p_T hadrons.

All the previus aspects of heavy–ion physics are studied at STAR. The present work focuses on jet characterization in p+p and d+Au collisions. It provides a baseline for analog studies in heavy–ion collisions. In particular

the the choosen analysis method link this work to the study of γ–jet events which are particularly significative in order to understand the interaction of jet particles with their surrounding medium.

Chapter 2

Jets

2.1 Jet production

The production of hadrons in heavy ion collisions can be described in QCD by the interaction of quarks and gluons. Figure 2.1 shows the Feynman diagrams of a few examples of leading order processes that can lead to the production of high–p_T partons or jets. Figure 2.1(a), 2.1(b) and 2.1(c) show typical di–jet production, where two jets are created from a single collision. Figure 2.1(d) and 2.1(e) involve also the emission of a single photon.

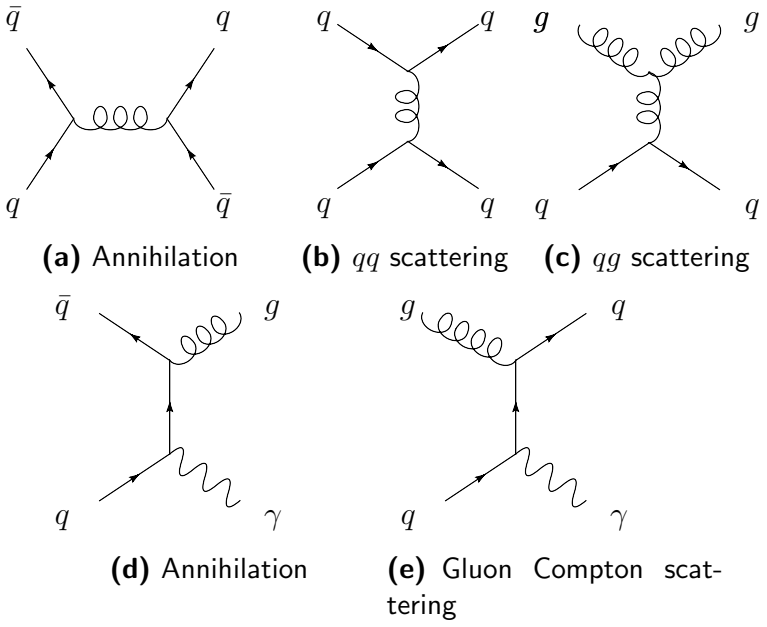

(a) Annihilation **(b)** qq scattering **(c)** qg scattering

(d) Annihilation **(e)** Gluon Compton scattering

Figure 2.1: Feynman diagrams of typical processes generating jets.

As discussed in section 1.1, quarks and gluons can not exist freely, but only in colorless states. Partons emerging from the collisions fly apart creating additional quark–anti–quark pairs. While the electro–weak potential decreases with distance, the potential of the strong force increases with distance. Thus, the energy between two partons increases with distance as long as the color field contains enough energy to produce a new $q\,\bar{q}$ pair. For a high initial energy this process can be repeated several times and the momentum directions of the hadrons so produced result correlated.

The so obtained cluster is called *jet*. Figure 2.2 shows a typical di–jet event in a $e^+ + e^-$ collision: two clusters of particles are observed opposite in azimuth.

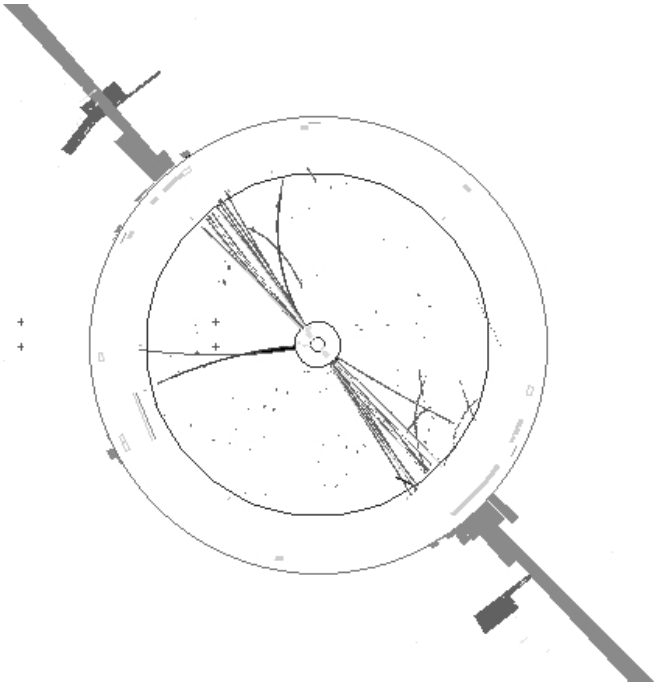

Figure 2.2: Di–jets event in a e^+e^- collisions observed in the OPAL [12] experiment.

In a heavy ion collision, the parton from the hard scattering can interact with soft particles in the medium while traversing it before producing a jet [13]. The corresponding loss of energy is referred to as jet–quenching. The initial partonic scattering processes in nucleus–nucleus interactions should be similar to those occuring in proton–proton interactions, which have been extensively studied at various collision energies. Their production probabilities can be calculated using perturbative QCD. The energy loss depends on the

traversed distance in the medium, and could be seen in the suppression of high–p_T particles from jets. While the partons produced in the initial hard scattering interact with the medium, prompt photons (shown in figure 2.1(d) and 2.1(e)) pass through the medium without interaction.

2.2 Jet azimuthal correlation

Jets are oriented back–to–back in the plan transverse to the beam axis and are thus separated by a relative azimuthal angle $\Delta\phi \sim \pi$. A simple way to study a jet is to use a trigger particle with high transverse momentum and then look at the associated particles from that same event and their azimuthal correlation.

One of the clear signatures of jet quenching at RHIC is the disappearance of the jet in the direction opposite to the trigger particle [10, 14]. This is a phenomenom typical of heavy ion collision, while p+p and d+Au collisions show a regular away–side jet. Figure 2.3 shows the two–particle azimuthal distribution $D(\Delta\phi)$, defined as

$$D\left(\Delta\phi\right) = \frac{1}{N_{\text{trigger}}} \frac{1}{\varepsilon} \frac{dN}{d(\Delta\phi)} \tag{2.1}$$

where N_{trigger} is the number of particles with momentum $4 < p_T^{\text{trigger}} < 6\ \text{GeV}/c$, referred to as trigger particles, and ε is the tracking efficiency of the associated particles. Each trigger particle is associated to all the other particles in the same event having $2 < p_T < p_T^{\text{trigger}}$. The plots in figure 2.3(a) are fitted according to the distribution

$$D(\Delta\phi) = Y_N \frac{e^{-(\Delta\phi)^2/2\sigma_N^2}}{\sqrt{2\pi}\sigma_N} + Y_A \frac{e^{-(|\Delta\phi|-\pi)^2/2\sigma_A^2}}{\sqrt{2\pi}\sigma_A} + P. \tag{2.2}$$

Figure 2.3(b) shows the azimuthal distributions for p+p and central d+Au collisions after uncorrelated background subtraction and the distribution for Au+Au collision after uncorrelated background and elliptic flow subtraction. While the near–side peak is similar in the three systems, the away–side peak in central Au+Au collisions shows a significant suppression relative to p+p and d+Au collisions.

It has also been shown that the away–side correlation peak reappears in Au+Au collisions, if the energy of trigger and associated particles increases sufficiently, as shown in figure 2.4 [15, 16]. This shows how the most energetic jets can still penetrate the medium. The reappearance of the away–side peak is also compatible with the suppression and the complete disappearance in older analysis can be explained with the low statistic available.

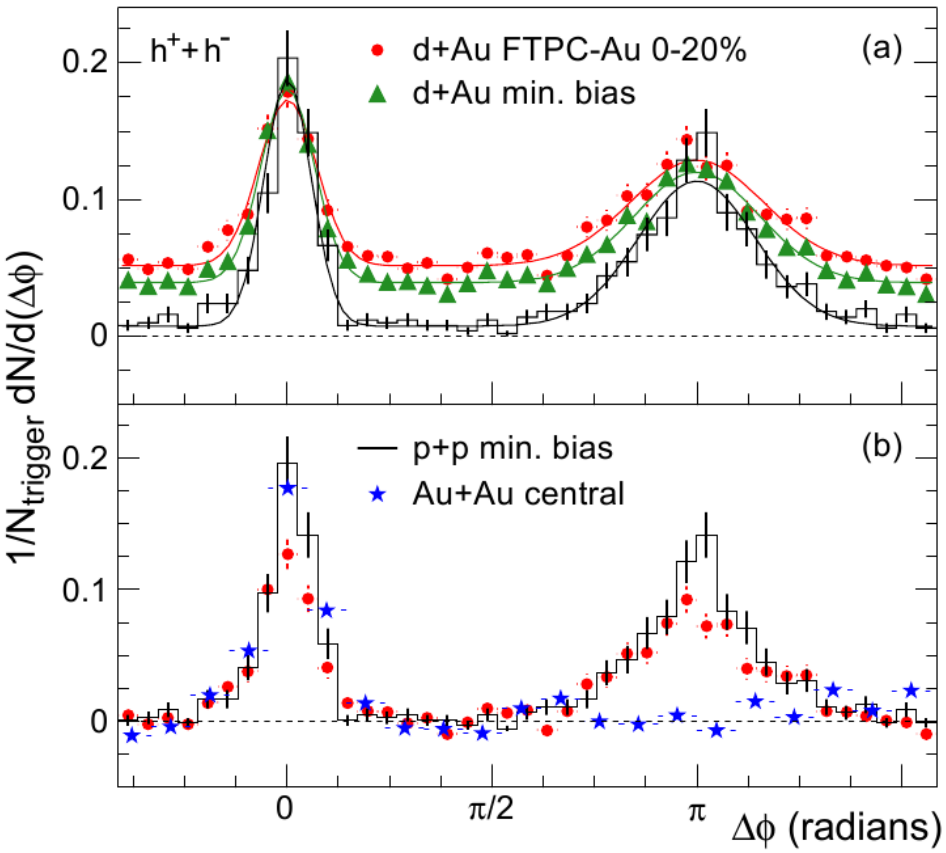

Figure 2.3: (a) Two–particle azimuthal correlation distributions for minimum bias and central d+Au collisions, and for p+p collisions [10]. (b) Comparison of two-particle azimuthal distributions for central d+Au collisions to those seen in p+p and central Au+Au collisions [10]. Figure taken from [14].

These correlations can in principle be used to quantitatively study parton energy loss in heavy-ion collisions. Large uncertainties do however remain in the interpretation, because the initial energy of the partons is unknown.

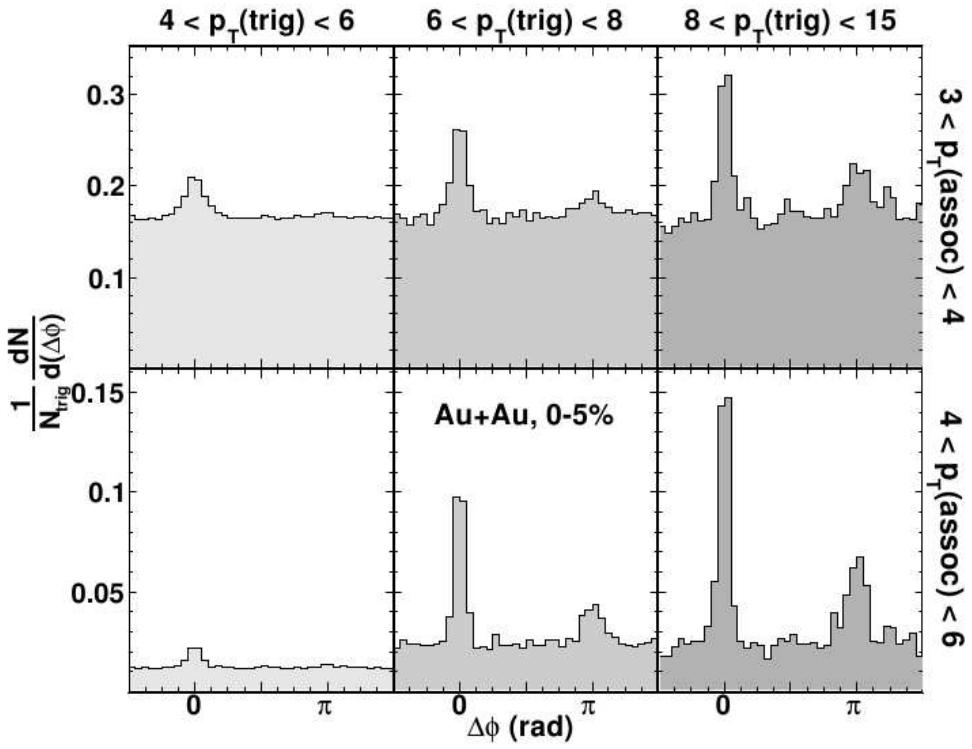

Figure 2.4: Azimuthal correlation of high–p_T charged hadron pairs for central Au+Au events for various p_T^{trig} and p_T^{assoc} ranges. In the lower left panel the yield is suppressed due to the constraint $p_T^{\text{assoc}}<p_T^{\text{trig}}$. All p_T values in this figure have units GeV/c. Figure taken from [15].

2.3 Photon production and jet angular correlation

In the processes depicted by diagrams 2.1(d) and 2.1(e) the emission of one jet is balanced by a single photon, called *prompt photon*. These are called γ–jet events. Jet quenching shows that hadronic jets are modified by the medium. On the other side, a single photon will traverse the Quark–Gluon Plasma without interacting with the medium. The energy of the exiting photon is equal to the initial energy of the hadronic jet. In contrast to two–hadron correlation, γ–jet study provides thus a calibrated measurement. Therefore, γ–jet correlation allows to quantitatively estimate the energy loss of the jet in the medium.

In addition to prompt photons there are also *bremsstrahlung photons*. They are radiated off a parton before the jet fragments. An example of

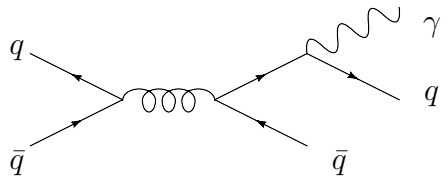

Figure 2.5: Feynman diagram of quark–antiquark scattering with Bremsstrahlung radiation.

the process is shown in the diagram in figure 2.5. Bremsstrahlung photon emission can occur in the vacuum and can as well be induced by the scattering of the parton in the medium. In contrast to prompt photons these photons do not carry the full momentum transferred in a hard collision but can be part of a jet and are thus not as usefull as clear γ–jet events.

Unfortunately, photons are also decay products of several mesons and resonances. In the final state of the collision several meson species decay electromagnetically into photons. The largest contribution comes from the π^0 meson decays $\pi^0 \rightarrow \gamma\gamma$ and $\pi^0 \rightarrow e^+e^-\gamma$ with a branching ratio of 98.8% and 1.2%, respectively. The η–meson decays $\eta \rightarrow \gamma\gamma$ with a branching ratio of 39.43%. These two sources produce about 99% of the photons coming from the decay of particles.

Thus, the main contribution to photon spectra is not due to prompt production, but to π^0 and other particle decays. Several other studies of photon production and γ–jet correlation are needed to complete the picture. In particular a study of π^0 spectra [17], prompt photon spectra [18] and γ–jet correlation [19] have already been performed.

The aim of the present analysis is to obtain information about inclusive photon–charged hadron azimuthal correlation in p+p and d+Au collisions, which serves as a baseline measurement for further studies in the more complex system of Au+Au collisions.

2.4 Jet properties

The hard scattering of two partons results in jet production [20, 21, 22, 23]. The cross section of the process is

$$\frac{d^3\sigma}{dx_1 dx_2 d\cos\theta^*} = \frac{1}{s}\sum_{ab} f_a(x_1)\, f_b(x_2)\, \frac{\pi\alpha_s^2(Q^2)}{2x_1x_2}\Sigma^{ab}(\cos\theta^*) \qquad (2.3)$$

The parton distribution function $f_a(x_1)$ gives the probability for a parton a to carry a momentum fraction x_1 of the initial colliding protons, being $f_b(x_2)$

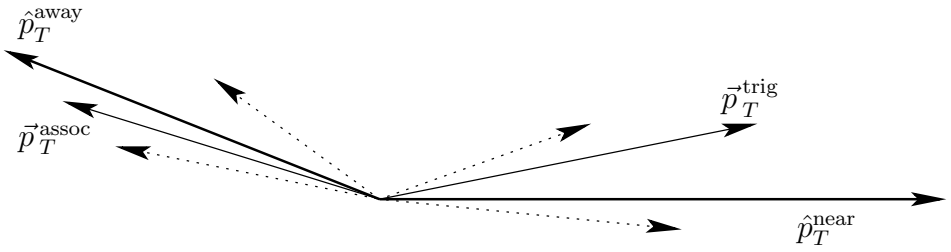

Figure 2.6: Schematic view of a hard scattering event in the plane perpendicular to the beam. Two scattered partons are seen in the laboratory frame to have momenta $\hat{p}_T^{\text{near}}$ and $\hat{p}_T^{\text{away}}$. The partons fragment producing a trigger and an associated jet.

the same for b. The parton-parton energy in the center of mass is $\hat{s} = x_1 x_2 s$ where $\sqrt{s}$ is the energy in the center of mass for the protons. In the center of mass frame, θ^* is the scattering angle of the considered partons and thus $\Sigma^{ab}(\cos\theta^*)$ describes their angular distribution.

Equation (2.3) gives the p_T spectrum of an outgoing parton c (emitted at θ^*), which then fragments into hadrons, e.g. a π^0. The fragmentation function $D_c^{\pi^0}(z)$ is the probability for a π^0 to carry a fraction $z = p^{\pi^0}/p^c$ of the momentum of the outgoing parton c. The fragmentation function can be seen as the probability of "finding a hadron in a parton". Fragmentation functions express intrinsic properties of the hadronization mechanism, therefore, they are subject to non-perturbative physics and cannot be calculated from first principles in QCD at present [24]. The shape of fragmentation functions can be determined by experiments. As an example, to calculate π^0 production equation (2.3) must be summed over all subprocesses leading to a π^0 in the final state.

In this formulation, $f_a(x_1)$ and $f_b(x_2)$ and $D_c^{\pi^0}(z, \mu^2)$ represent the "long–distance phenomena" that are to be determined experimentaly; while the characteristic subprocess angular distributions, $\Sigma^{ab}(\cos\theta^*)$, and the coupling constant, $\alpha_s^2(Q^2)$, are fundamental predictions of QCD [25] for the short–distance phenomena.

Figure 2.6 shows a schematic view of a hard–scattering event. The two scattered partons, carrying transverse momentum $\hat{p}_T^{\text{near}}$ and $\hat{p}_T^{\text{away}}$, propagate nearly back–to–back in azimuth from the collision point. Then they fragment in the final state particles with a jet–like shape.

Figure 2.7 shows a more detailed scheme of a hard–scattering event. The momentum perpendicular to the jet axis is denoted as $\vec{j}_T$. This vector has two components: one perpendicular to $\hat{p}_T^a$ in the transverse plane, and one in the longitudinal plane (defined by the jet axis and the beam axis). The

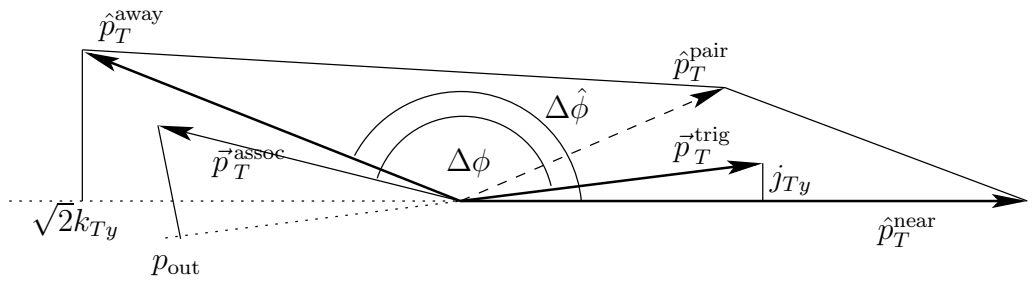

Figure 2.7: Detailed schematic view of a hard scattering event in the plane perpendicular to the beam. Two scattered partons are seen in the laboratory frame to have momenta $\hat{p}_T^{\text{near}}$ and $\hat{p}_T^{\text{away}}$. The partons fragment producing a trigger and an associated jet. Only two particles carrying momenta $\vec{p}_T^{\text{trig}}$ and $\vec{p}_T^{\text{assoc}}$ are represented. $\sqrt{2}k_{Ty}$ is the projection of $\vec{k}_T$ perpendicular to $\hat{p}_T^{\text{near}}$. The component of $\vec{p}_T^{\text{assoc}}$perpendicular to $\vec{p}_T^{\text{trig}}$is p_{out}. j_{Ty} is the transverse momentum component of the trigger jet.

first will be denoted as j_{Ty}, the latter as j_{Tx}. At lower energies, it has be found $\langle j_{Ty}\rangle \approx 400$ MeV/c [26], independent on p_T and consistent with measurements for e^+e^- collisions [27].

In a di–je event, the trigger particle with momentum $\vec{p}_T^{\text{trig}}$ is a fragmentation product of the trigger jet carrying momentum $\hat{p}_T^{\text{near}}$. The associated particle with momentum $\vec{p}_T^{\text{assoc}}$ may also be a fragment of the trigger jet leading to the near–side correlation, or it may be from the away–side jet of momentum $\hat{p}_T^{\text{away}}$. If the jet transverse fragmentation momentum j_T is negligible compared to the trigger $\vec{p}_T^{\text{trig}}$, from figure 2.7 the following relations can be deduced

$$p_{out} = |\vec{p}_T^{\text{assoc}}| \sin(\pi - \Delta\phi) = |\vec{p}_T^{\text{assoc}}| \sin(\Delta\phi) \tag{2.4}$$

$$\sqrt{2}k_{Ty} = |\hat{p}_T^{\text{away}}| \sin\left(\pi - \Delta\hat{\phi}\right) = |\hat{p}_T^{\text{away}}| \sin\left(\Delta\hat{\phi}\right) \tag{2.5}$$

being p_{out} the component of $\vec{p}_T^{\text{assoc}}$ perpendicular to $\vec{p}_T^{\text{trig}}$. For small angles the sinus can be approximated with the angle, therefore, the following relations

$$\langle\frac{p_{out}}{|\vec{p}_T^{\text{assoc}}|}\rangle = \langle\sin(\Delta\phi)\rangle \simeq \langle\Delta\phi\rangle = \langle\Delta\hat{\phi}\rangle \simeq \langle\sin\left(\Delta\hat{\phi}\right)\rangle = \langle\frac{\sqrt{2}k_{Ty}}{|\hat{p}_T^{\text{away}}|}\rangle \tag{2.6}$$

are valid and, hence,

$$\sqrt{2}k_{Ty} = p_{out}\frac{|\hat{p}_T^{\text{away}}|}{|\vec{p}_T^{\text{assoc}}|}. \tag{2.7}$$

The jet shape is naturally quantified by momenta of the jet particles measured in the parallel and perpendicular direction with respect to the jet

axis. The variable $z{=}p_T/\hat{p}_T$ is parallel to the jet axis, and it is equivalent to the jet fragmentation variable [28]. Equation 2.7 can therefore be written as

$$\sqrt{2}k_{Ty} = p_{out}\frac{\hat{p}_T^{\text{away}}}{p_T^{\text{assoc}}} \equiv \frac{p_{out}}{z_a}. \tag{2.8}$$

In this way, knowing the fragmentation variable z_a, the measure of p_{out} determines the magnitude of k_T. Unfortunately the fragmentation variable can not be measured since $\hat{p}_T^{\text{away}}$ is unknown, anyway it can be evaluated from the fragmentation function. Fragmentation functions from e^+e collisions, weighted by the appropriate hard–scattering constituent cross–sections, could in principle be used for this purpose.

It was originally thought that the shape of the fragmentation function could be deduced from measurements using the combined analysis of the inclusive trigger p_T and associated particle p_T distributions. It has been seen [29] that the average momentum of the parton fragmenting into a trigger particle, $\langle z_t \rangle$, changes as a function of p_T^{assoc} when if p_T^{trig} is fixed. This kind of trigger bias causes the value of $\hat{p}_T$ to be not fixed for the case where p_T^{trig} is fixed but p_T^{assoc} varies. For a more detailed discussion of this problem see section 6.4.

2.4.1 Intra–jet transverse momentum (j_T)

A closer look to a jet schematic in the near–side (figure 2.8) shows the relations (2.9).

$$\begin{aligned}
\sin\phi_t &= \frac{j_{Ty}^{\text{trig}}}{p_T^{\text{trig}}} \equiv x_t \\
\sin\phi_a &= \frac{j_{Ty}^{\text{assoc}}}{p_T^{\text{assoc}}} \equiv x_a \\
\sin\Delta\phi &= \frac{p_{\text{out}}}{p_T^{\text{assoc}}} \\
\Delta\phi &= \phi_t + \phi_a
\end{aligned} \tag{2.9}$$

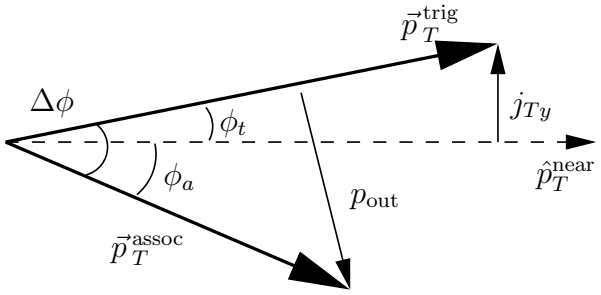

Figure 2.8: Schematic view of near–side jet fragmentation. The angle ϕ_t (ϕ_a) is the angle between the trigger (associated) particle and the jet axis, in the plane perpendicular to the beam axis. For the whole event scheme refer to figure 2.7.

Assuming ϕ_t and ϕ_a to be statistically independent, the relation

$$\langle \sin^2 \Delta\phi \rangle = \langle \sin^2 \phi_t \cos^2 \phi_a \rangle + \langle \sin^2 \phi_a \cos^2 \phi_t \rangle \tag{2.10}$$

is valid. Substituting (2.9) in (2.10) and with the hypothesis $j_{Ty}^{\text{assoc}} \approx j_{Ty}^{\text{trig}} = j_{Ty}$ it can be written

$$\langle \left(\frac{p_{\text{out}}}{p_T^{\text{assoc}}} \right)^2 \rangle = \langle \left(\frac{j_{Ty}}{p_T^{\text{trig}}} \right)^2 \rangle + \langle \left(\frac{j_{Ty}}{p_T^{\text{assoc}}} \right)^2 \rangle - 2 \langle \left(\frac{j_{Ty}}{p_T^{\text{trig}}} \right)^2 \left(\frac{j_{Ty}}{p_T^{\text{assoc}}} \right)^2 \rangle. \tag{2.11}$$

Remembering the assumption of p_T^{assoc} and p_T^{trig} being statistically independent it is possible to multiply all terms by $(p_T^{\text{assoc}})^2$. Defining $x_h = |\vec{p}_T^{\text{assoc}}|/|\vec{p}_T^{\text{trig}}|$ and rearranging the terms, equation (2.11) becomes

$$\langle j_{Ty}^2 \rangle = \frac{\langle p_{\text{out}}^2 \rangle}{1 + \langle x_h^2 \rangle - 2\langle x_t^2 \rangle}. \tag{2.12}$$

Assuming a Gaussian shape for the near–side azimuthal distribution, it is possible to express p_{out} as a function of the peak width

$$\begin{aligned} \langle p_{\text{out}}^2 \rangle &= \langle p_{T,\text{assoc}}^2 \sin^2 \Delta\phi \rangle \\ &\approx \langle p_{T,\text{assoc}}^2 \rangle \left(\sin \langle \Delta\phi^2 \rangle - \frac{\langle \Delta\phi^4 \rangle}{3} \right) \\ &\approx \langle p_{T,\text{assoc}}^2 \rangle \left(\sin \sigma_N^2 - \sigma_N^4 \right). \end{aligned} \tag{2.13}$$

where in the first approximation the power series expansion of $\sin^2 \Delta\phi$ is truncated at the second term, while in the second approximation the equivalence $\langle \Delta\phi^2 \rangle \approx \sigma_N^2$ is used, where σ_N^2 is the width of the near–side peak of the azimuthal correlation distribution. If $p_T^{\text{trig}} \gg j_T$, then $x_t \approx 0$ and, taking in account also (2.13) and approximating $\sigma_N^4 \approx 0$, (2.12) can be rewritten as

$$\sqrt{\langle j_{Ty}^2 \rangle} \simeq \sigma_N \frac{\langle p_T^{\text{trig}} \rangle \langle p_T^{\text{assoc}} \rangle}{\sqrt{\langle p_T^{\text{trig}} \rangle^2 + \langle p_T^{\text{assoc}} \rangle^2}}. \tag{2.14}$$

2.4.2 Jet acoplanarity (k_T)*

It was originally thought that parton collisions were collinear with the p+p collision axis, so that the two emerging partons would have the same magnitude of transverse momentum pointing opposite in azimuth. However, it was found [30] that each of the partons carries initial transverse momentum k_T,

*This section is based on the discussion of [29] and adopts the same notation.

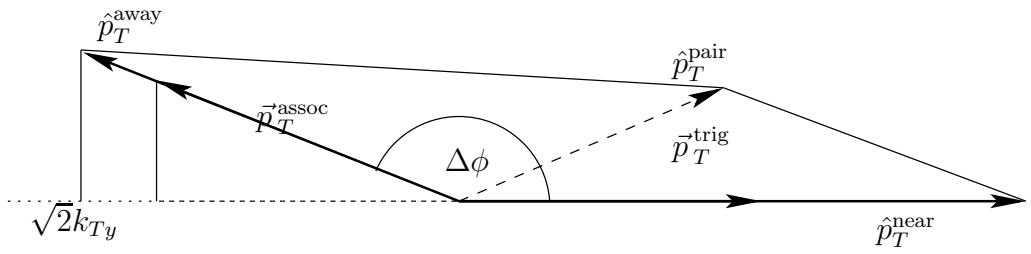

Figure 2.9: Schematic view of a hard scattering event in the plane perpendicular to the beam. The trigger and associated $\langle j_T \rangle$ are neglected.

originally described as "intrinsic" [31]. This results in a momentum imbalance (the partons momenta do not add up to p_T=0) and in an acoplanarity (the transverse momentum of one jet does not lie in the plane determined by the transverse momentum of the second jet and the beam axis). The jets are non–collinear having a net transverse momentum $\langle p_T^2 \rangle_{\text{pair}} = 2\langle k_T^2 \rangle$.

The magnitude of the acoplanarity momentum vector, $\vec{k}_T$, has been measured at ISR energies and it was found to be of the order of 1 GeV/c. The expected intrinsic parton transverse momentum, governed by hadron size, should be around 300 MeV. Additional gluon radiation before or after the hard scattering may be the cause for the larger observed acoplanarity [31].

In order to extract $\langle |k_{T_y}| \rangle$, or $\langle k_T^2 \rangle$[†], the variables p_{out} (see eq. (2.4)) and x_E are the starting point.

$$x_E = -\frac{\vec{p}_T^{\text{trig}} \cdot \vec{p}_T^{\text{assoc}}}{|\vec{p}_T^{\text{trig}}|^2} = -\frac{p_T^{\text{assoc}} \cos\Delta\phi}{p_T^{\text{trig}}} \simeq \frac{z_a \hat{p}_T^{\text{away}}}{z_t \hat{p}_T^{\text{near}}} \tag{2.15}$$

where z_a and z_t are the momentum fraction carried by the fragments on the away–side jet and the near–side jet respectively. The approximate formula to derive $\langle |k_{T_y}| \rangle$ from the measurement of p_{out} as a function of x_E is [31]

$$\langle |p_{out}| \rangle^2 = x_E^2 \left[2\langle |k_{T_y}| \rangle^2 + \langle |j_{T_y}| \rangle^2 \right] + \langle |j_{T_y}| \rangle^2 \tag{2.16}$$

Figure 2.9 shows a schematic view of a hard scattering event if both trigger and associated $\langle j_T \rangle$ are neglected. In this case the following relations

[†]Relations between $\sqrt{X^2}$ and $\langle |X_y| \rangle$, where X is any two–dimensional quantity, are found appendix A

are valid:

$$\langle|p_{out}|\rangle|_{j_T^{\rm trig}=0,j_T^{\rm assoc}=0} = \sqrt{2}\langle|k_{T_y}|\rangle\frac{p_T^{\rm assoc}}{\hat{p}_T^{\rm away}} = \tag{2.17}$$

$$= \sqrt{2}\langle|k_{T_y}|\rangle\langle z\rangle\frac{x_h}{\hat{x_h}} \tag{2.18}$$

$$\Rightarrow \sqrt{\langle p_{out}^2\rangle_{j_T^{\rm trig}=0,j_T^{\rm assoc}=0}} = \langle z\rangle\sqrt{\langle k_T^2\rangle}\frac{x_h}{\hat{x_h}} \tag{2.19}$$

where $\langle z\rangle = \langle p_T^{\rm trig}/\hat{p}_T^{\rm near}\rangle$ and x_h is the ratio of the associated particle transverse momentum to the trigger particle transverse momentum

$$x_h = \frac{|\vec{p}_T^{\rm assoc}|}{|\vec{p}_T^{\rm trig}|} \tag{2.20}$$

and $\hat{x}_h$ is the partonic equivalent which is a function of x_h and of $\langle k_T^2\rangle$

$$\hat{x}_h = \hat{x}_h(\langle k_T^2\rangle, x_h) = \frac{\langle|\hat{p}_T^{\rm away}|\rangle}{\langle|\hat{p}_T^{\rm near}|\rangle}. \tag{2.21}$$

where $\hat{p}_T^{\rm near}$ and $\hat{p}_T^{\rm away}$ are the transverse momentum of the trigger parton and the associated parton respectively. The relations in appendix A are used from (2.18) to (2.19).

The jet fragments are produced with finite jet transverse momentum $\vec{j}_T$. Considering the situation where the trigger particle is produced with $j_{T_y}^{\rm trigger}$ >0 GeV/c and the associated particle with $j_{T_y}^{\rm assoc}$=0 GeV/c as in figure 2.7, $\vec{p}_{\rm out}$ picks up an additional component

$$\langle p_{out}^2\rangle|_{j_T^{\rm trig}>0,j_T^{\rm assoc}=0} = \left[\langle p_{out}^2\rangle_{00} + \frac{\langle|\vec{j}_{T_y}^{\rm trig}|^2\rangle}{|\vec{p}_T^{\rm trig}|^2}\left(|\vec{p}_T^{\rm assoc}|^2 - \langle p_{\rm out}^2\rangle_{00}\right)\right]\frac{|\vec{p}_T^{\rm trig}|^2 - \langle|\vec{j}_{T_y}^{\rm trig}|^2\rangle}{|\vec{p}_T^{\rm trig}|^2} \tag{2.22}$$

$$= x_h^2\left[\langle z_t\rangle^2\langle k_T^2\rangle\frac{1}{\hat{x}_h^2} + \langle|\vec{j}_{T_y}^{\rm trig}|^2\rangle\right] \tag{2.23}$$

with the assumption $j_{T_y}^{\rm trig} \ll p_T^{\rm trig}$. Applying the same approximation for the away–side jet $j_{T_y}^{\rm assoc} \ll p_T^{\rm assoc}$, equation 2.23 becomes

$$\langle p_{out}^2\rangle = x_h^2\left[\langle z_t\rangle^2\langle k_T^2\rangle\frac{1}{\hat{x}_h^2} + \langle|\vec{j}_{T_y}^{\rm trig}|^2\rangle\right] + \langle|\vec{j}_{T_y}^{\rm assoc}|^2\rangle \tag{2.24}$$

and this can be solved for $\langle z_t\rangle\sqrt{\langle k_T^2\rangle}/\hat{x}_h$

$$\frac{\langle z_t\rangle\sqrt{\langle k_T^2\rangle}}{\hat{x}_h} = \frac{1}{x_h}\sqrt{\langle p_{out}^2\rangle - \langle|\vec{j}_{T_y}^{\rm assoc}|^2\rangle - x_h\langle|\vec{j}_{T_y}^{\rm trig}|^2\rangle} \tag{2.25}$$

Assuming $\langle|\vec{j}_{T_y}^{\text{assoc}}|^2\rangle \simeq \langle|\vec{j}_{T_y}^{\text{assoc}}|^2\rangle$ the final formula is

$$\frac{\langle z_t\rangle\sqrt{\langle k_T^2\rangle}}{\hat{x}_h} = \frac{1}{x_h}\sqrt{\langle p_{out}^2\rangle - \langle j_{T_y}^2\rangle(1+x_h)} \tag{2.26}$$

where $\langle j_{T_y}^2\rangle$ can be extracted from the correlation function as described in section 2.4.1 and the other variables can be measured directely. In the following chapters the notation

$$\kappa_T = \frac{\langle z_t\rangle\sqrt{\langle k_T^2\rangle}}{\hat{x}_h} \tag{2.27}$$

will be used.

Chapter 3

Experimental setup

3.1 Relativistic Heavy Ion Collider

The Relativistic Heavy Ion Collider (RHIC) at Brookhaven National Laboratory (BNL) in New York, USA, was built to study elementary p+p and nuclear collisions at various energies from $\sqrt{s_{NN}}$ ≈20 GeV up to $\sqrt{s_{NN}}$ ≈200 GeV. The main goal of the facility is to study the Quark–Gluon Plasma, and the spin structure of protons.

In figure 3.1, a schematic of the accelerator facility is shown. At the interaction points along the ring there are four detector systems for as many experiments. STAR*[32] and PHENIX†[33] are two large collaborations involved both in the heavy ion program and the spin physic program. PHOBOS‡[34] and BRAHMS§[35] are smaller experiments focused on the heavy ion program.

RHIC accelerates the ions to the final energy. Since it cannot accelerate particles from rest, other facilities are used for this purpose:

- In Tandem Van De Graff facility gold ions are accelerated to an energy of 1 MeV/u and stripped of electrons to a charge Q=+32.

- LINAC is the linear accelerator used to boost protons instead of the Tandem. From the LINAC the protons are injected into the Booster and then they follow the same way of the heavy ions.

*Solenoidal Tracker At RHIC

†Pioneering High Energy Nuclear Physics Experiment

‡The proposal for MARS (Modular Array for RHIC spectroscopy) was rejected, but later a similar proposal under the name PHOBOS, was accepted.

§Broad Range Hadronic Spectrometers Experiment at RHIC

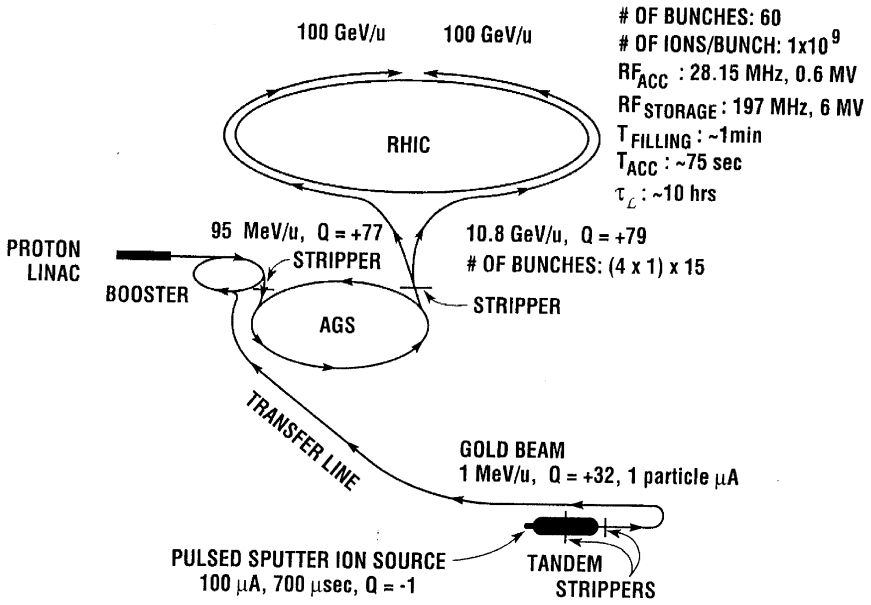

Figure 3.1: The RHIC accelerator complex.

- In the Booster accelerator gold ions are accelerated to an energy of 95 MeV/u. When the ions are extracted from the booster, they are stripped to Q=+77.
- The Alternating Gradient Synchrotron (AGS) accelerates the ions to 10.8 GeV/u. Before being injected into the RHIC, the ions are stripped of the last two electrons, to a charge Q=+79.

RHIC consists of two concentric independent rings with a circumference of 3834 m equipped with 1740 superconducting magnets and radio frequency (RF) cavities. The tubes are highly evacuated and kept to a temperature of 4.5 K. In each collider ring 60 bunches of $\sim 10^9$ ions are injected. This yields a design luminosity of $\mathcal{L} \approx 2 \cdot 10^{26} \mathrm{cm}^{-2} \mathrm{s}^{-1}$. It takes approximately 1 minute to fill the collider. The beam is usually stored for about 10 hours.

3.2 STAR detector

The Solenoidal Tracker At RHIC (STAR)[32] is built to measure the thousands of particles which can be produced by a single collision at RHIC.

The ability to measure decay products and large–angle correlations played a key role in the design of STAR. This goal was achieved by providing full az-

imuthal coverage in the mid–rapidity region, characteristic typical of STAR, and at the same time several other STAR detectors provide additional coverage in the forward region. The curvature of charged particle trajectories in a magnetic field allows the determination of their momentum. Therefore, the tracking detectors are surrounded by a solenoid magnet providing a uniform magnetic field up to 0.5 T. Figure 3.2 and 3.3 show a schematic layout.

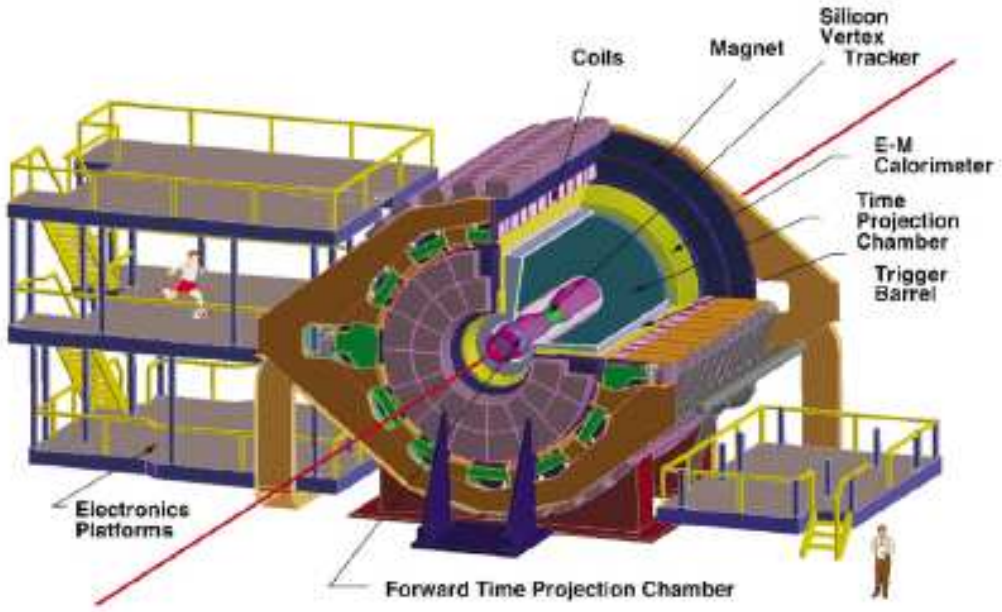

Figure 3.2: Perspective view of the STAR detector with a cutaway for viewing inner detector systems.

STAR is composed of the following subdetectors:

- The Time Projection Chamber (TPC) [36] is the central detector of STAR. It measures trajectories of charged particles with pseudorapidity η <1.8, and it provides tracking information and particle identification at mid–rapidity. A short overview will be given in section 3.3.

- The Barrel ElectroMagnetic Calorimeter (BEMC)[37] detects photons and electrons with pseudorapidity $|\eta|$ <1. An overview of it will be given in section 3.4.

- The Silicon Vertex Tracker (SVT) [38] is located inside the TPC and consists of three concentric barrels of silicon drift detectors situated at 5 cm, 10 cm and 15 cm from the beam. A very good vertex position resolution as well as a good momentum and two track resolution is

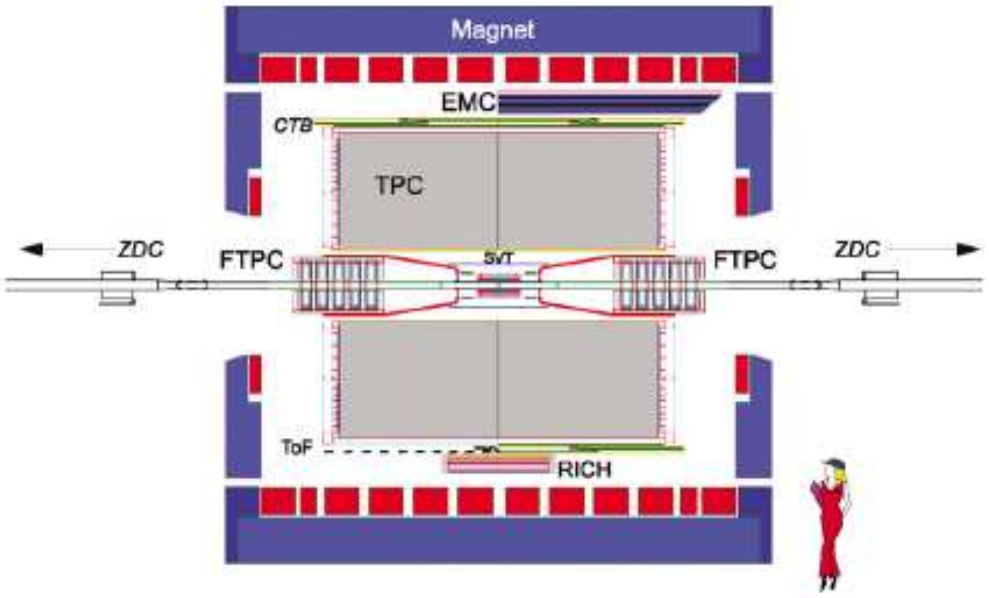

Figure 3.3: Cutaway side view of the STAR detector as configured in 2001.

achieved with this detector. Additionally, energy loss measurements improve the particle identification capabilities.

- The Silicon Strip Detector (SSD) [39] is another cylindric silicon detector located at 23 cm from the beam axis. It has a good momentum resolution and is also used for particle identification. Together with the SVT it is designed to reconstruct the secondary decay vertices of strange particles.

- The Endcap ElectroMagnetic Calorimeter (EEMC) [40] extends the coverage of the BEMC up to pseudorapidity η <2.

- The Forward Time Projection Chamber (FTPC) [41] is a radial drift TPC, which measures tracks with pseudorapidity 2.5< η <4.0 increasing the acceptance of STAR.

These detectors are enclosed in a solenoidal magnet providing a field B=0.5 T. In the present analysis only the TPC and the BEMC are used.

Other fast detectors are used for trigger purposes [42].

- Central Trigger Barrel (CTB): a barrel of 240 scintillator slats surrounding the main TPC, yields information about the multiplicity.

- Zero Degree Calorimeters (ZDC): two calorimeters close to the beam, but 18.25 m from the main event vertex, measure spectator neutrons. The measurements of the ZDC contain information about the z-coordinate of the event vertex and about the centrality. They are used to trigger minimum bias events in d+Au collisions. See also section 3.5.1.

- Beam-Beam Counters (BBC): these two sets of hexagonal scintillators are located at 3.7 m from the interaction point and provide a minimum bias trigger in p+p collisions. See also section 3.5.2.

3.3 Time Projection Chamber

The main tracking detector of the STAR experiment is the Time Projection Chamber (TPC) which covers the full azimuthal angle in a pseudorapidity region of -1.8< η <1.8. The TPC can track particles with momentum between 100 MeV/c and 30 GeV/c, and identify them via the characteristic energy loss up to 1 GeV/c. The reading out of an event creates a three–dimensional image of approximately 70 millions of points, enough to handle the high multiplicity of central Au+Au collisions.

The TPC is a hollow cylinder parallel to the beam line, with an inner radius of 0.5 m, an outer radius of 2 m and a overall length of 4.2 m. The cylinder is filled with P10 gas, a mixture of 90% argon and 10% methane, kept at 2 mbar positive pressure in order to prevent air to enter from outside. It sits in the homogeneous magnetic field which is generated by the solenoidal magnet and oriented along the beam axis.

A charged particle going through the TPC ionizes the gas molecules on average every few tenths of a millimeter along its path. A central membrane at the center of the TPC is kept at -28kV. The electric field makes the ionization electrons drift to the endcaps.

The endcap consists of 12 multi–wire proportional chambers (MWPCs), each of them covering an angle of 30^o. The MWPCs consist of three planes of wires (the gating grid, the ground grid and the anode grid) and a pad plane connected to the front–end electronics. A schematic layout of the read out region is shown in figure 3.5.

- During the event read-out, the gating grid is open to allow the drift of ionization electrons. After that, it closes to prevent positive ions from drifting to the TPC volume.

- The ground grid separates the homogeneous drift field from the strongly inhomogeneous amplification field surrounding the anode wires.

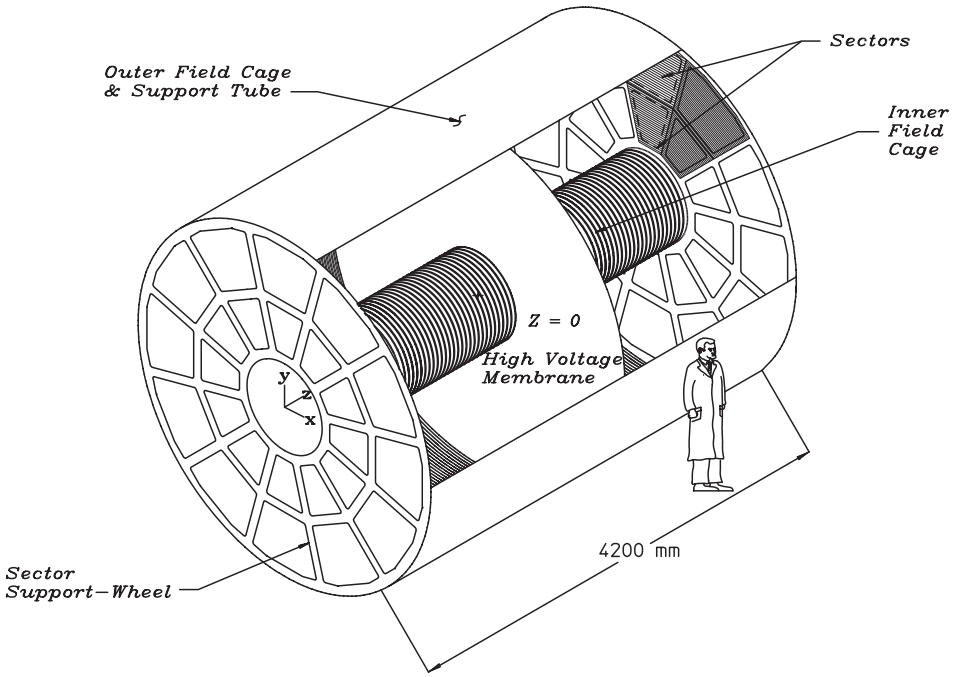

Figure 3.4: Schematic layout of the STAR TPC.

- The anode area is characterized by a strong inhomogeneus electric field which accelerates the drifting electrons and generates an electron avalanche. This allows a signal amplification, which is proportional to the initial number of the drifting electrons. Finally, the anode grid collects all the electrons.

The readout pads are divided into 12 super sectors on each TPC side. Each super sector is divided into an inner and an outer sector (figure 3.6). Each inner sector contains a large number of small pads, distributed in 13 pad rows, to maximize the position and two-track resolution in a region with high particle densities. The pads of the outer sectors are densely packed in 32 rows per sector to optimize the measure of energy loss by ionization in a region with lower particle densities.

The signals induced in several adjacent pads allow to identify the position where the particle ionized the gas. For each collision, each pad is read 512 times, giving the time information that allows to determine the distance covered by the drifting cloud. The drift velocity is known and it equal to

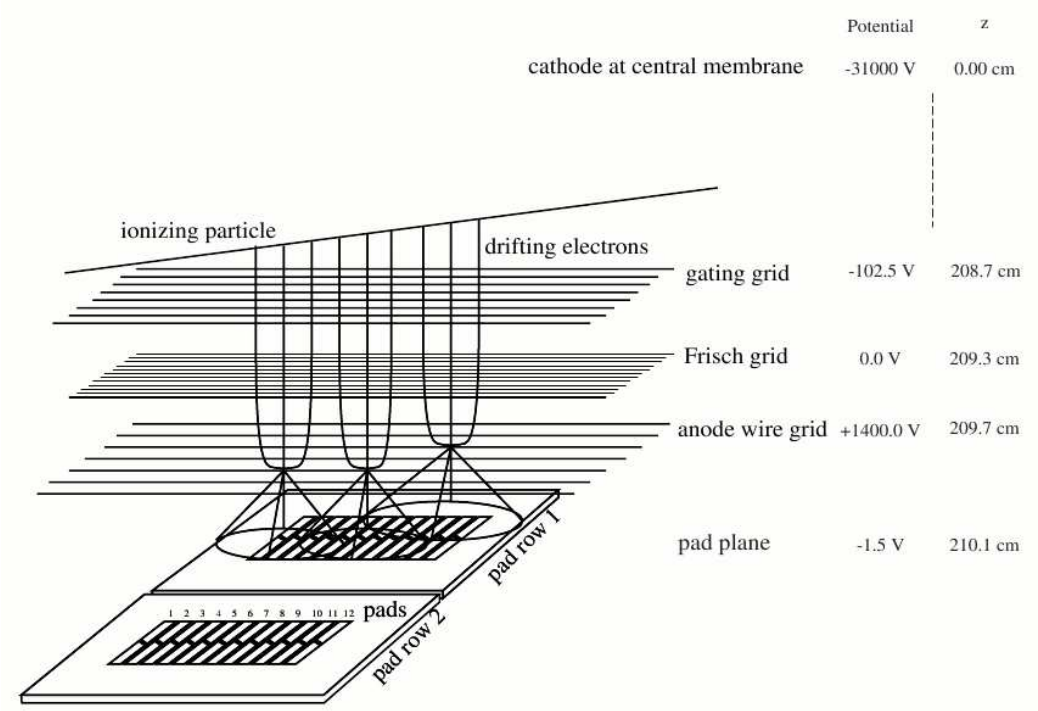

Figure 3.5: Principle of electron drift and signal amplification in a time projection chamber. The values on the right hand side for the potential and the distance to the central membrane z are typical values for the outer sector of the STAR TPC.

5.4 cm/μs. Putting the spatial information together with the time information, it is possible to reconstruct point by point the trajectory of a charged particle across the TPC volume.

The TPC allows also to identify particles via the specific energy loss, which can be calculated using the Bethe–Bloch formula:

$$\frac{dE}{dx} = -\frac{2\pi N_A z^2 e^4}{mc^2\beta^2}\frac{\rho Z}{A}\left\{\ln\frac{2mc^2\beta^2 E_M}{I^2(1-\beta^2)} - 2\beta^2\right\}. \tag{3.1}$$

In this formula, the properties of the particle are its charge z and its velocity β. Being Z, A, ρ and I the atomic number, the mass number, the density and the specific ionization of the drifting gas respectively. E_M is the maximum energy transfer in one interaction. The other constants are the mass m of the electron, the charge e of the electron, the speed of light c and the Avogadro number N_A[43]. The particle can be identified by its momentum dependence on the specific energy loss.

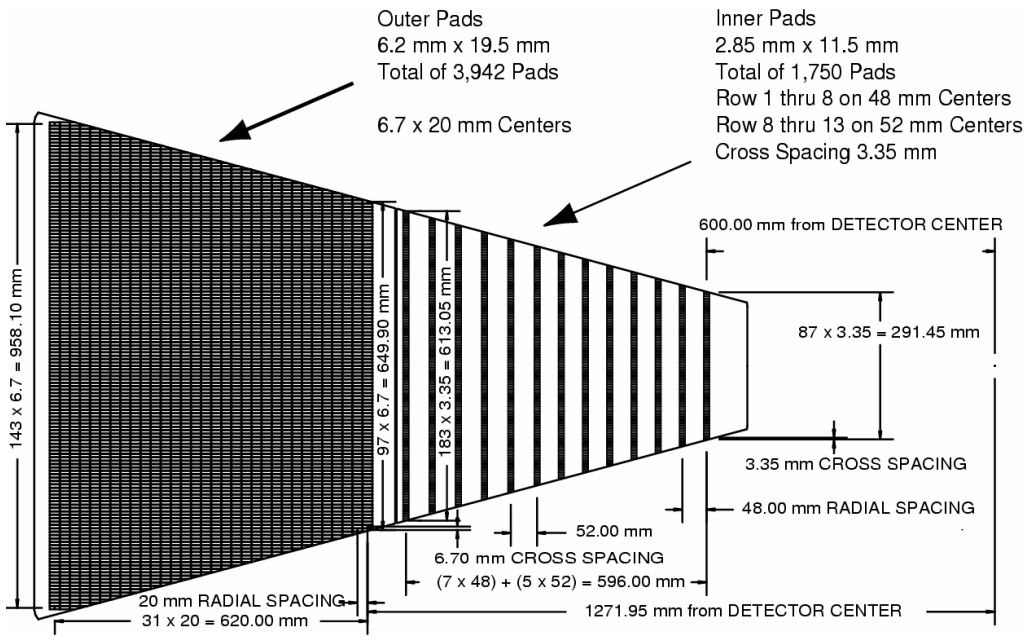

Figure 3.6: The anode pad plane with one full sector. The inner sub–sector has small pads arranged in widely spaced rows for a better two–particle resolution. The outer sub–sector is densely packed with larger pads for a better energy resolution.

3.3.1 Track reconstruction

A two step process is used to reconstruct the particle trajectories in the TPC:

1. Cluster finding: contiguous regions of ionization within the same pad–row are localized. Clusters from different tracks can overlap in case of small difference in momenta. Therefore, the algorithm searches for maxima in the selected region and a deconvolution procedure is used to separate the different contributions. The result of this process is a set of space–points where charged particles ionize the drift gas.

2. Track finding: clusters from the same particle are identified and combined in a track. The algorithm starts from the outer pads, where the cluster density is lower and it is therefore easier to identify single particle deposit. The seed cluster is then connected to the closest inner one and so on toward the beam line, resulting in a sequence of segments which are then fitted using an helix model which takes into account multiple scattering and energy loss in the detector gas. The fit segments which belong to the same track are merged.

Once the track is definite, the particle momentum is reconstructed from the helix curvature in the magnetic field. From the equivalence of the Lorentz force to the centripetal force

$$q|\vec{v} \times \vec{B}| = \frac{mv^2}{R} \tag{3.2}$$

where $\vec{v}$ is the particle velocity perpendicular to the magnetic field, q is the particle charge, R the curvature radius and $\vec{B}$ the magnetic field.

The momentum p of the particle is related to the curvature radius

$$p = qRB. \tag{3.3}$$

Therefore, the momentum resolution is determined by the spatial resolution of the TPC.

3.4 Barrel Electromagnetic Calorimeter

The STAR Barrel ElectroMagnetic Calorimeter (BEMC) is a sampling calorimeter consisting of alternate layers of lead and plastic scintillator with an energy resolution of $\Delta E/E \approx 16\%/\sqrt{E}$ GeV$^{-1/2}$. It is located behind the TPC, and it has the same acceptance of the projecting chamber (figure 3.7). It has a radius of 2.3 m and full azimuthal coverage in the pseudorapidity

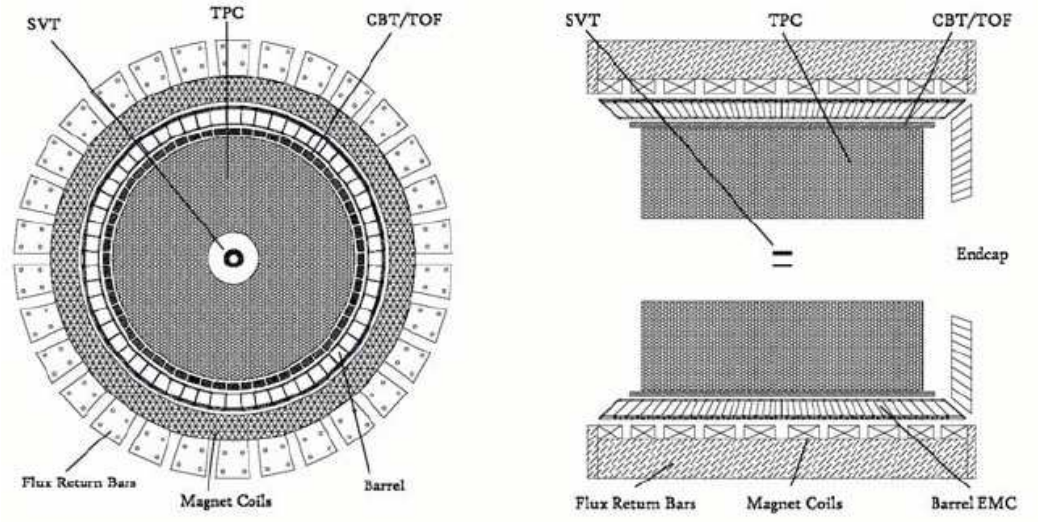

Figure 3.7: Schematic layout of the STAR BEMC. The Calorimeter is located between the TPC volume and the magnet.

range $-1 < \eta < 1$. The calorimeter is composed of 120 modules, each of them covering 6^o in azimuthal angle ϕ and 1.0 unit in pseudorapidity η; this is equivalent to a width of 26 cm and a length of 293 cm. The modules are mounted in 2 sections in η, 60 modules per section. Each module is divided into 40 towers, 2 towers in ϕ and 20 towers in η. Each tower measures 0.05×0.05 rad in the η–ϕ plane. The calorimeter is segmented into 4800 towers, each of them projecting back to the interaction area (figure 3.8). The projecting structure allows the BEMC to mimic the spherical geometry which is natural for a collision.

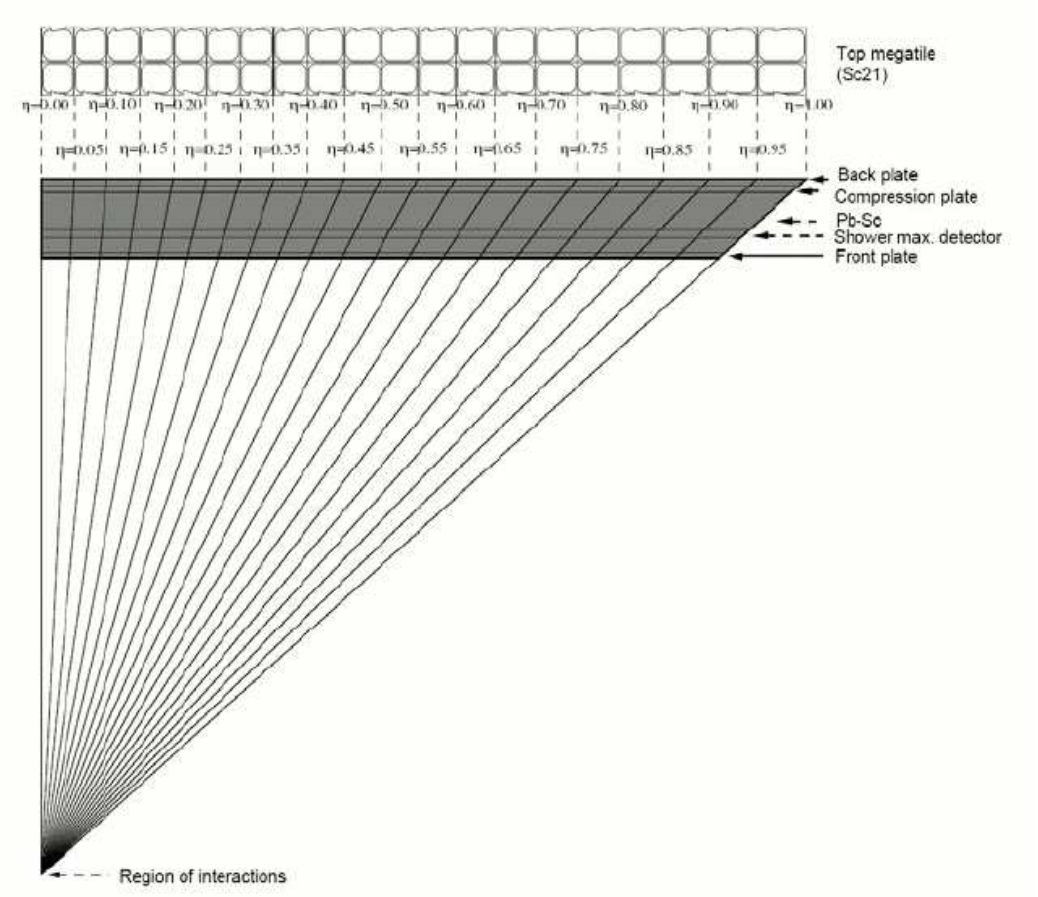

Figure 3.8: Side view of a calorimeter module showing the projective shape of the towers.

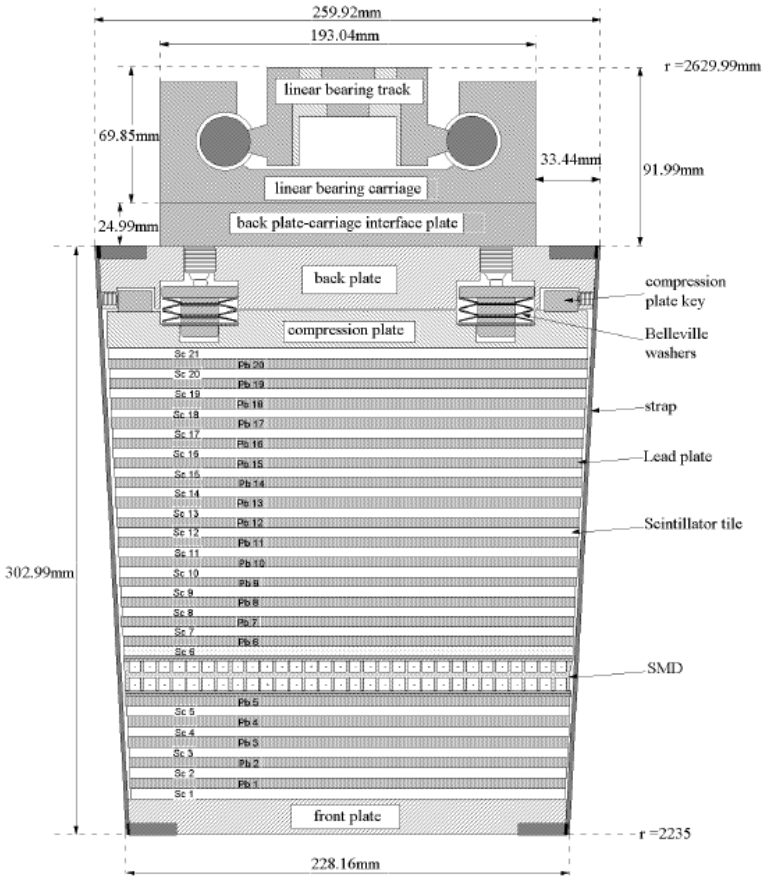

Figure 3.9: Cross section of a BEMC tower. The different layers are cleary visible, together with the mechanical assembly. At $5X_0$ from the front face the preshower detector PSD is located.

3.4.1 Towers

The cross section of one tower is shown in figure 3.9. Each module consists of 20 layers of 5 mm thick lead plates alternating with 21 layers of plastic scintillator of the same size, for an active depth of 23.5 cm or 21 radiation length (X_0). The stack is held together by 30 straps connecting the front and back plate of the tower. Each tower covers 0.05 units in pseudorapidity, and 0.05 radians (about 3^o) in azimuth. The constant size in pseudorapidity units implys an increasing size in z-direction.

A photon interacting with the first layer of lead creates an electron/positron pair, which interacts with the heavy material emitting Bremsstrahlung photons. When the emitted photons are energetic enough, they can generate

another electron/positron pair. The new pair interacts with the materials emitting again Bremsstrahlung photons and the process continues as long as the emitted photons are energetic enough to create a new pair. The number of pairs and photons increases reaching a peak near $5X_0$ into the detector, and dies out before exiting the detector. The BEMC is designed to record particles with energies up to 60 GeV, although the probability for photon or electron production with similar transverse energy is very low in $\sqrt{s_{NN}}$=200 GeV collisions.

Using fiber links, the signal of each layer of a tower is carried to a light mixer; from here the signal of the whole tower is transferred to a photomultiplier tube, which amplifies it. Finally, an ADC digitizes the signal.

3.4.2 Shower Maximum Detector

The size of a tower is larger than an electromagnetic shower, so a Shower Maximum Detector (SMD) is used to increase the spatial resolution. It is a wire proportional chamber with a unique double layer design. The two cathode planes with strips orientated along η and ϕ allow the reconstruction of a two–dimensional image of the shower (figure 3.10). The extruded aluminum profiles provide ground channels for the two planes of wires. The charge deposited in the gas by a passing particle is collected on the wires.

In the energy range between 0.5 and 5 GeV, the response of the SMD is linear with the particle energy if the SMD is placed at about $5X_0$ in the BEMC, and this is the approximate position where the showers are maximally developed.

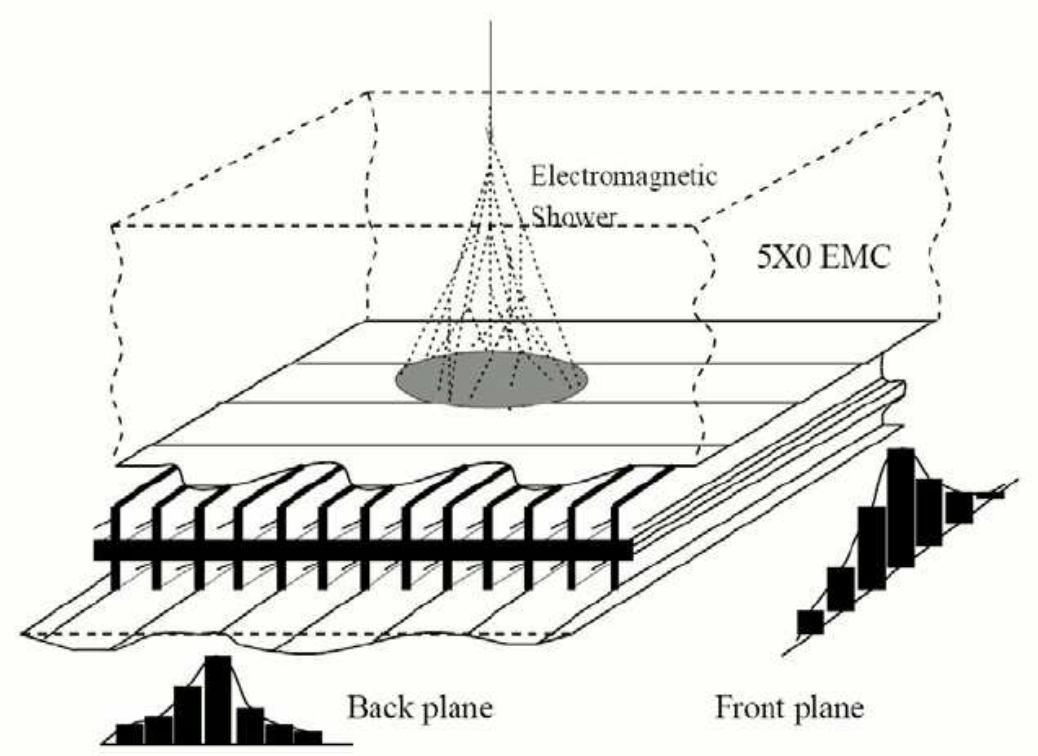

Figure 3.10: Schematic illustration of the SMD working principle. Two independent wire layers provide a bi–dimensional picture of the shower.

3.5 Trigger

3.5.1 Zero Degree Calorimeter

Located at about 18 m from the interaction point, on both sides of the detector, the Zero Degree Calorimeter (ZDC) is designed to detect neutrons emitted in the collision within a cone of $|\theta| < 2$ milli–radians around the beam axis (see figure 3.11).

Each ZDC consists of three modules. Each module consists of a series of tungsten plates alternating with layers of wavelength shifting fibers that route Cherenkov light to a photo–multiplier tube.

The energy measured by the ZDCs is proportional to the neutron multiplicity, which is known to be correlated with the event geometry and can be used to measure the centrality of the collision. However, in this analysis the ZDC is used only as minimum bias trigger in d+Au collisions, requiring at least one neutron detected along the gold direction. The acceptance of this trigger corresponds to 95±3% of the total d+Au geometric cross section.

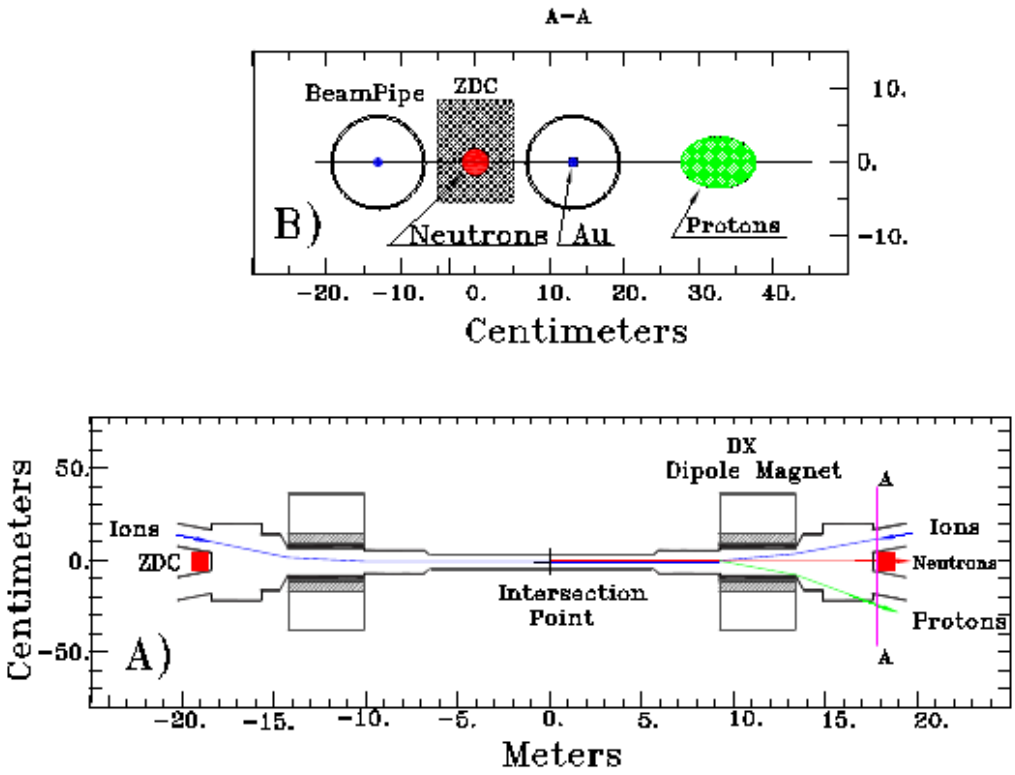

Figure 3.11: Plan view of the collision region and "beams eye" view (section A-A) of the ZDC location indicating deflection of protons and charged fragments downstream of the dipole magnet.

3.5.2 Beam-Beam Counters

The STAR Beam-Beam Counters consist of large and small hexagonal scintillator tiles as shown in figure 3.12. They are mounted around the beam pipe on the East and West sides outside the pole–tip of the STAR magnet at $\pm$3.7 m from the interaction point. A ring with a radius between 9.6 cm and 48 cm is fully covered by the array of 18 small hexagonal tiles, corresponding to the pseudorapidity region of 3.4$<|\eta|<$5.0. The ring between 38 cm and 193 cm, corresponding to a pseudorapidity region of 2.1$<|\eta|<$3.6 is covered by the 18 large tiles.

The BBCs mainly provide a minimum bias trigger for p+p collisions. In Au+Au collisions the many mid-rapidity tracks and spectator neutrons can be used as trigger, but these signatures are absent in p+p collisons. A coincidence in at least one of the 18 small BBC tiles on both sides provides a trigger for p+p collisions. The difference in the time of flight between the two

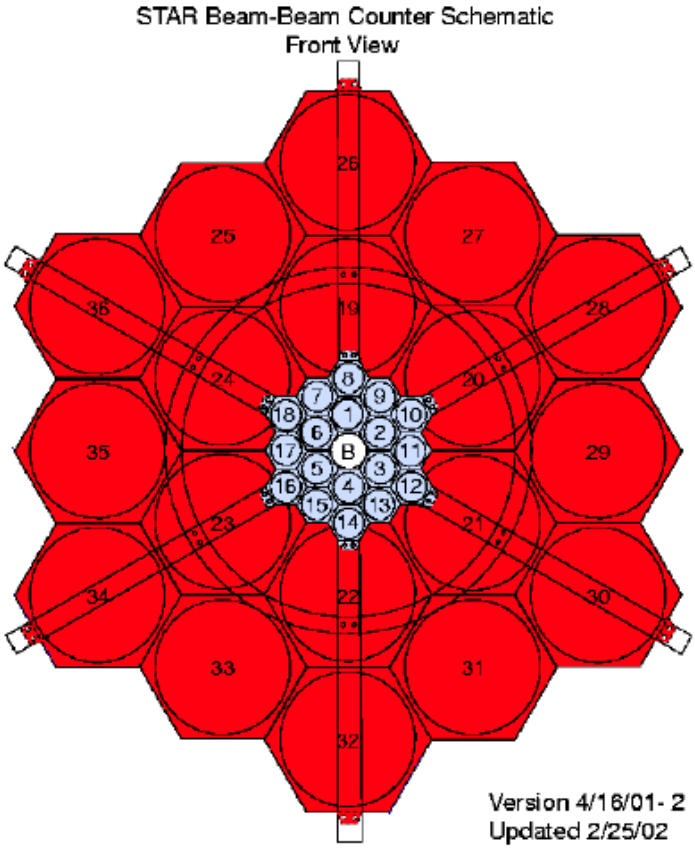

Figure 3.12: Schematic front-view of the Beam-Beam Counters.

sides of the BBC's gives also information on the interaction vertex position. Large values in time of flight are associated with the passage of beam halo and, as a conequence, the corresponding trigger is rejected.

3.5.3 High–Tower Trigger

The drift time in the TPC limits the recorded event rate to 100 Hz, while the beam crossing frequency at RHIC is 10 MHz. The trigger system processes information from fast detectors (BBC, BEMC, CTB and ZDC) to decide if an event should be recorded or not [42]. Each event is categorized according to several trigger criteria.

The datasets used in the present analysis were taken in the 2003 d+Au run (Run–3) and in the 2005 p+p run (Run–5). The following trigger conditions are required:

Minimum bias trigger in d+Au collisions. The presence of a signal corresponding to at least one neutron detected by the ZDC in the gold

beam direction triggers a minimum bias event.

Minimum bias trigger in p+p collisions. The trigger is provided by the coincidence of at least one of the 18 small BBC tiles on both sides of the interaction point.

High–tower trigger. The high–tower trigger requires the minimum bias condition and an energy deposit above a fixed threshold in at least one BEMC tower. Two thresholds are fixed at the values in table 3.1, thus, two different triggers are defined: HT1 with the lowest threshold, and HT2 with the highest.

Dataset	High–tower 1 [GeV]	High–tower 2 [GeV]
d+Au 2003	2.5	4.5
p+p 2005	2.6	3.5

Table 3.1: High–tower trigger thresholds.

3.6 Data acquisition

The data acquisition system (DAQ) is responsible for the collection of data from all detectors, the assembly of a single data block containing all detector contributions, the writing of these blocks to a file on disk, and the transfer of these files to the long term storage system [44].

Data from slow detectors, which are not part of the trigger system and are not read out for every bunch crossing, is sent to the DAQ system over optical links that end in the Receiver Boards. The Receiver Boards perform 10–to–8 bit conversion, zero suppression, cluster finding and data formatting. For each detector, there are one or more Detector Brokers (DET) which control several Receiver Boards. These DETs provide a detector independent interface to the DAQ network.

The Event Builder (EVB) collects data from all detectors, and assembles the data for one event in a structure suitable for storage in a file and offline processing. The events are saved to local disk, with each file containing several hundreds events. These files are then transferred to the RHIC Computing Facility and saved in the High Performance Storage System (HPSS).

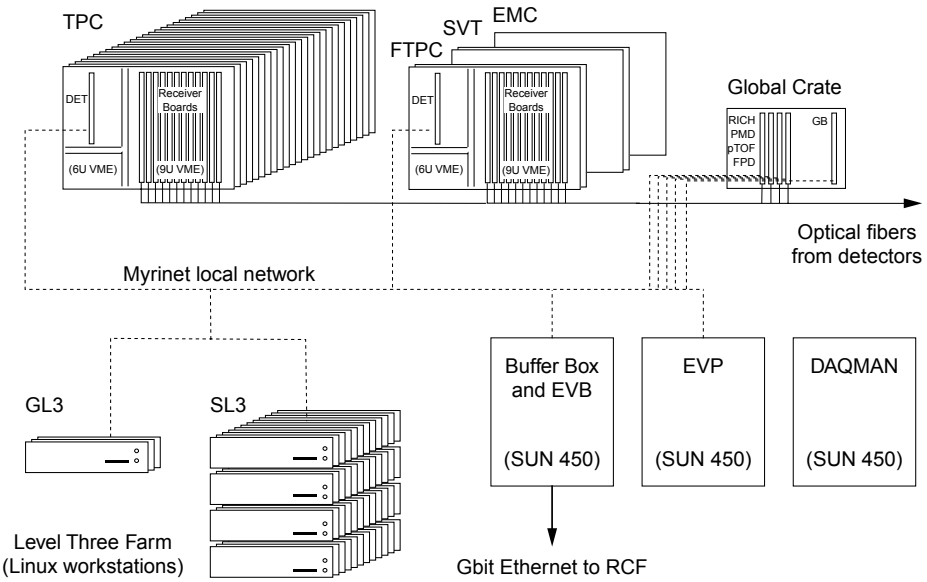

Figure 3.13: Schematic layout of the DAQ network in the STAR experiment [44].

Chapter 4

Quality assurance procedure

4.1 Event reconstruction

The first step of event reconstruction in STAR experiment is track reconstruction from TPC and FTPC signals. This procedure is summarized in section 3.3.1.

All analysis utilizing the BEMC, as the present one, are performed in a later step. Although the information provided by the BEMC and SMD can be used to fully reconstruct π^0 and η particles [17], in this analysis only single tower information is used. The detailed description of π^0 energy reconstruction can be found in section 4.4.

4.2 Event selection

4.2.1 Vertex position

The primary vertex position is found using the reconstructed TPC tracks. The accuracy along the z axis is better than one millimeter. In the present analysis only events with primary vertex position with $|z_{\text{vertex}}| < 60$ cm are included [17, 18]. The amount of material traversed by the particles increases at higher z_{vertex} values and, as a consequence, the TPC tracking efficiency drops, moreover, the towers project to z_{vertex}=0 cm. For such a vertex position the longitudinal development of the shower is confined mostly in a single tower. For very large $|z_{\text{vertex}}|$ values the geometry of the calorimeter is not well adapted.

4.2.2 High–tower trigger

The present analysis uses mainly events, which satisfy the high tower conditions described in section 3.5.3. For each event the energy of the highest tower is required to be higher than the trigger threshold. In this way the events triggered by noisy channels (called *hot towers*) are removed from the analysis.

Not all towers are suitable for this analysis. The procedure for selecting the usable towers is described in the following sections.

4.2.3 Tower selection

A quality assurance procedure is performed for the BEMC where malfunctioning detector components are removed from the data. For each run the ADC spectra of all towers are analyzed to recognize common failure modes like the malfunctioning of readout boards and crates. The result of this quality assurance procedure is a time–stamped status table, which is used as input for the physics analysis.

After applying the status table to select the functioning towers, still dead region can appear on the BEMC, caused by single dead towers or defective crates. Since the goal of this analysis is not a cross section measurement, it is not necessary to know the exact fraction of inactive BEMC regions. All inactive regions will not generate trigger particles, and will therefore be ignored implicitly.

It could happen that a tower considered weel functioning after the standard quality–check procedure on the ADC spectrum is still not working properly, usually because it fires too much. This leads to a non–uniformity in the azimuthal distribution which can be seen in figure 4.1.

If a tower triggers too much compared to the average, it is rejected as a hot tower. There are several reasons to explain the presence of hot towers, from insufficient optical isolation, to electronic problems to incorrect gain calibrations, but the result is the same: a hot tower generates trigger signals from either much less energetic particles or pure noise. To avoid the contamination of the set of trigger particles from these fake triggers, the hot towers have to be identified and excluded from the analysis.

To discriminate the hot towers, the frequency of a significant signal per tower is calculated. Towers with a frequency value 3 standard deviations larger than the average are tagged as hot and not considered in the following steps of the analysis. Figure 4.2 shows tower frequency after the hot towers have been removed. Table 4.1 summarizes how many towers have been removed because of standard quality requirements or because thy were hot

towers.

In year 2003 only half the BEMC was mounted and fully operational, for a full azimuthal angle coverage and pseudorapidity $0< \eta <1$. In 2005 the calorimeter was fully installed, for a pseudorapidity range $|\eta| <1$.

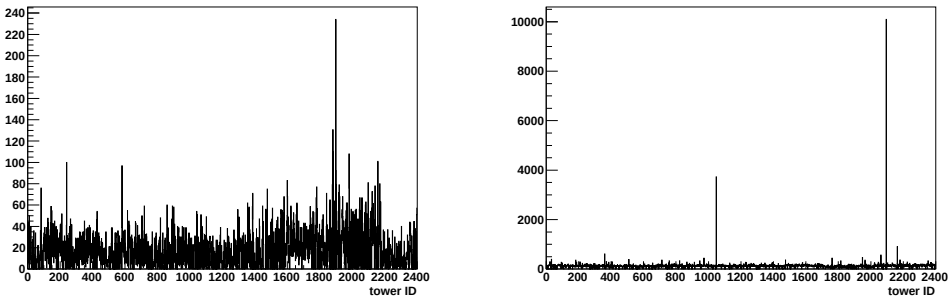

(a) d+Au collisions **(b)** p+p collisions

Figure 4.1: Trigger tower frequency distribution using the standard status table. Both in d+Au collisions (a) and p+p collisions (b) some of the towers fire much more than the average, signaling a potential calibration error.

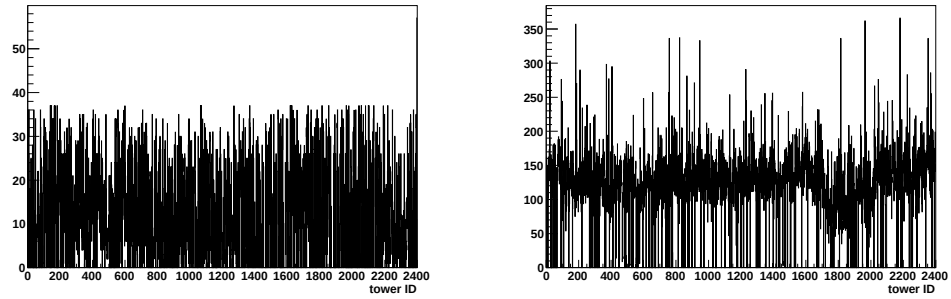

(a) d+Au collisions **(b)** p+p collisions

Figure 4.2: Trigger tower frequency distribution after towers selection. The standard status table is also taken into account. The resulting set of towers is used for the current analysis.

Dataset	standard status table	hot towers
d+Au 2003	≈10%	3.4%
p+p 2005	≈3%	2.6%

Table 4.1: Percentage of towers removed because of the standard quality requirements or because they were considered hot towers.

4.2.4 Track selection

The track reconstruction algorithm is described in section 3.3.1. In this analysis only *primary tracks* have been used. Primary tracks originate from the reconstructed primary vertex within a distance smaller than 1 cm. This means that most particles from weak decays are rejected from the analysis. To be accepted, a track must be reconstructed from at least 20 TPC hits. Finally, a pseudorapidity cut of $|\eta| < 1$ is required.

4.3 Background studies in d+Au collisions

During Run–3 data taking, corresponding to 2003 d+Au dataset, interactions of the beam with material external to the detector caused production of particles whose tracks can not be reconstructed in the TPC, since they are not originating at the collision point. Background events are thus characterized by high energy collected in the BEMC without a corresponding multiplicity in the TPC. It has also been found out that the background has a specific geometric distribution and it is possible to characterize it in several ways which will be described in the following sections.

- Ratio between TPC total p_T and BEMC total energy: background events are characterized by high energy deposit in the BEMC without a corresponding measured momentum in the TPC.
- Track multiplicity: events with no associated tracks in the TPC are rejected as background.
- Position of the trigger tower: some areas of the BEMC are more affected by background.

In d+Au collisions a stand–alone ZDC signal was sufficient to satisfy the minimum bias trigger condition. On the other side, in p+p collisions, the trigger requires a coincident signal on the BBCs which reduces the background. Therefore, p+p events are taken as reference, with the expectation they are not affected by the background. During the summer in 2006, before

the start of Run–6, additional shielding was installed on both sides of the STAR interaction region to further reduce the beam background.

A systematic study of how the cuts applied to reject beam background affect the azimuthal correlation between particles will be presented in section 5.4.

4.3.1 Energy ratio

Background events are characterized by a high energy deposit in the BEMC without a corresponding momentum measured in the TPC. In figure 4.3, the total BEMC energy per event is plotted as a function of the TPC momentum sum. Particles produced in the collisions deposit a similar energy on the TPC and on the BEMC. Background events are localized at low TPC energy.

To reject background events two different approaches are possible.

1. A cut on the minimum TPC energy removes the area where there are mainly background events. On the other side, also good events with low BEMC energy are removed. This corresponds to a vertical cut on figure 4.3(a) (solid line). In this way the events with high energy on the BEMC without a corresponding signal in the TPC are excluded.

2. Performing a cut on the ratio between the energy collected by the TPC and by the BEMC it is possible to include also low energy events. Figure 4.4 shows the ratio of the total transverse momentum measured in the TPC over the transverse energy collected by the BEMC: in d+Au events, the background is clearly characterized by a peak for small ratio values. The dashed line on figure 4.3(a) and figure 4.4 represents the cut used in the present analysis, corresponding to a ratio equal to 0.3.

On average, events with a higher multiplicity have also a higher energy deposited in the BEMC. Therefore, a cut on TPC multiplicity is equivalent to a energy cut. Since in p+p collisions the multiplicity is always low, it is preferable to consider the energy ratio between TPC and BEMC. It has been decided to use the cut on the energy ratio, because it allows to include a larger fraction of low multiplicity events. Moreover, a cut on the energy ratio ensures a balance in the energy distribution between the BEMC and the TPC which should be statistically present. This choice is in agreement with other analysis on π^0 [17] and direct photon production [18] within the same datasets used in the present work.

Section 5.4.1 will show how the cut on energy ratio affects the azimuthal correlation distribution.

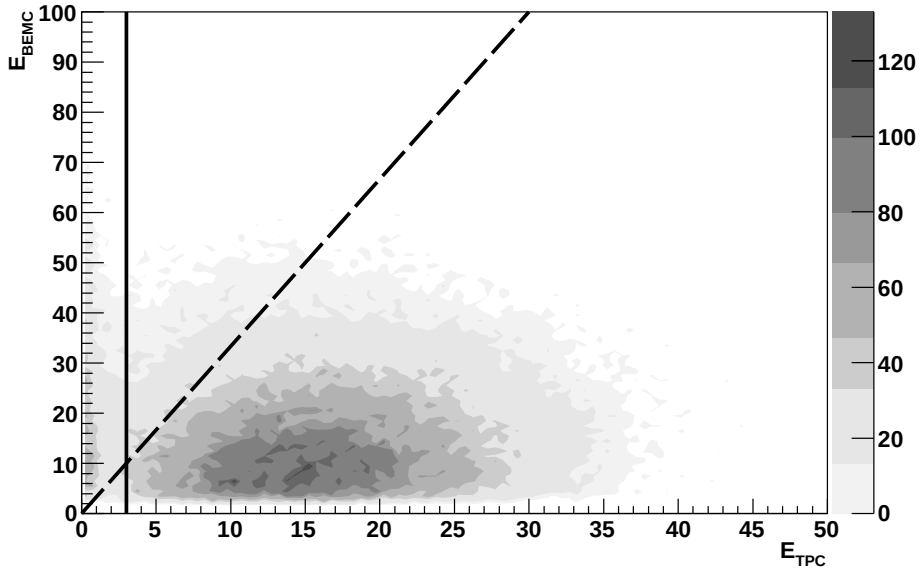

(a) d+Au collisions

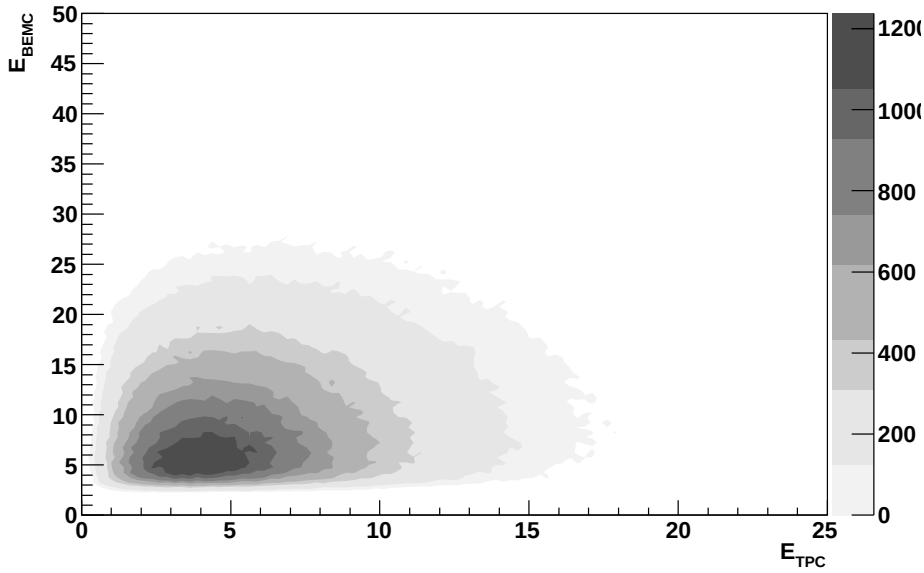

(b) p+p collisions

Figure 4.3: The energy collected by the BEMC is shown as a function of the total momentum measured by the TPC. Part of the events are characterized by a low TPC momentum, but a high BEMC energy. The vertical line represents a cut based on TPC energy alone, which is not effective in the low energy area. The diagonal dashed line indicates the cut used in the present analysis. In the lower panel, p+p events are not affected by the beam background.

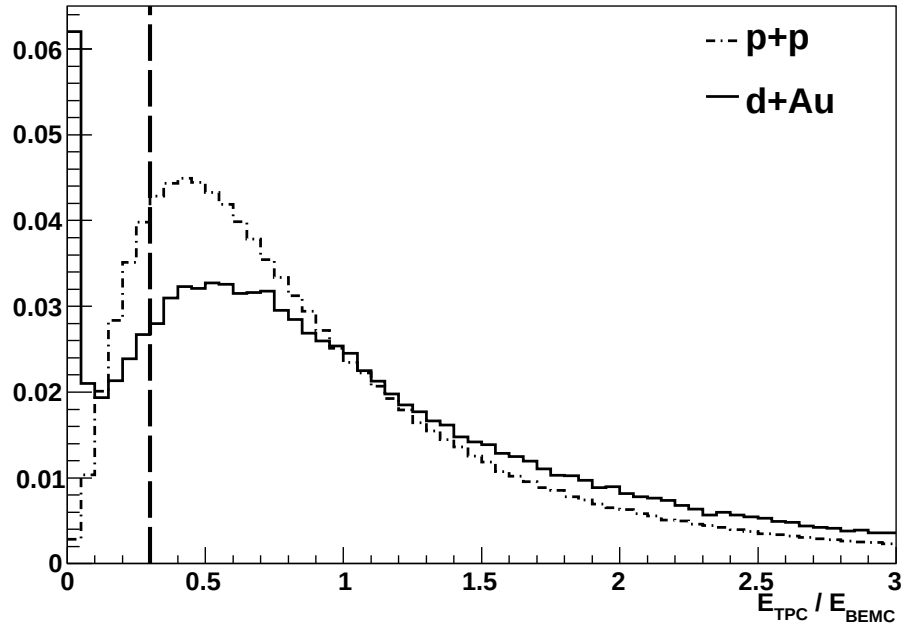

Figure 4.4: Distribution of the ratio of TPC transverse momentum to BEMC transverse energy. In d+Au events a peak at low values is caused by background events. In p+p events the low ratio peak is not present. The vertical line marks the position of the cut used in the present analysis.

4.3.2 Position of the trigger tower

Background events are characterized not only by a low transverse momentum measured by the TPC, but also by a low multiplicity. The tracking algorithm includes the vertex position in the tracks, thus tracks which do not point to the collision point can not be reconstructed. Background particles enter the TPC almost parallel to the beam axis. Therefore, although they hit the calorimeter, it is not possible to project their tracks back to the interaction point. The result is a low TPC multiplicity in the events triggered by background particles.

Because of the origin of background particles, only part of the BEMC is activated by background particles. It is possible to correlate the TPC multiplicity with the position of the trigger tower.

In figure 4.5 the TPC multiplicity is plotted as a function of the pseudorapidity of the trigger tower for d+Au and p+p events. In d+Au events (figure 4.5(a)) trigger towers associated with low multiplicity events are mainly localized at $\eta_{\text{trigger}} > 0.7$, while p+p events do not show any similar structures (figure 4.5(b)). Therefore, for d+Au events $\eta_{\text{trigger}} < 0.7$ is required. This value is marked by the dashed line in figure 4.5(a). Section 5.4.1 will show how the cut on the trigger tower pseudorapidity influences the azimuthal correlation distribution.

Similarly, also the azimuthal distribution of the trigger towers shows a correlation with the TPC multiplicity (figure 4.6). In d+Au events (figure 4.6(a)) low multiplicity events have a trigger tower mainly in $[-\pi, -2\pi/3]$ and in $[\pi/3, \pi]$, therefore this area has been excluded from the analysis and only the towers in the interval between the dashed lines are considered for trigger purpose. Also p+p events (panel (b)) show a dependence on the azimuthal angle, but it is weaker and not associated to low multiplicity events, therefore it is neglected in this analysis. Section 5.4.1 will show how the cut on the trigger tower azimuthal position affects the azimuthal correlation distribution.

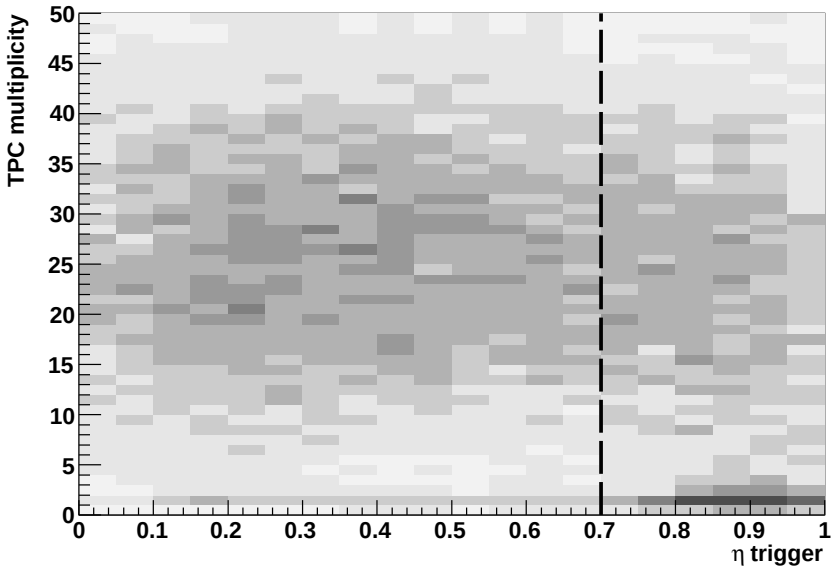

(a) d+Au events

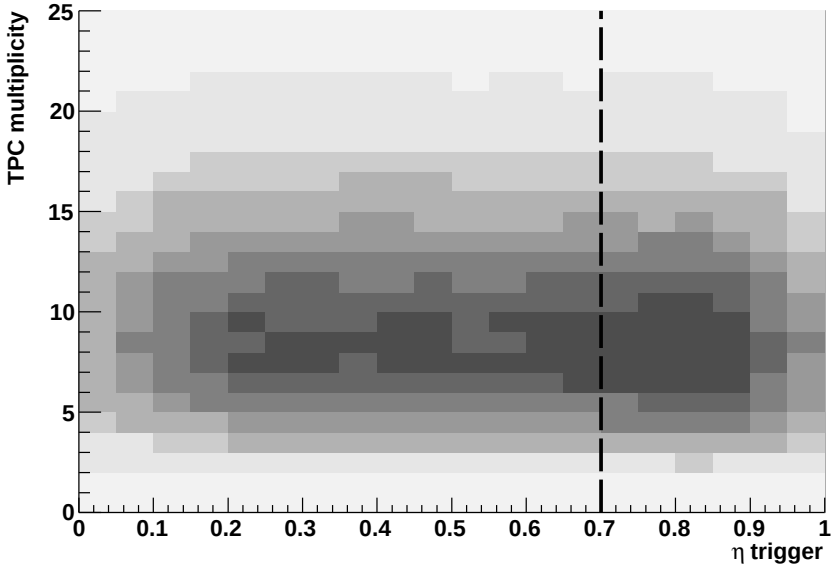

(b) p+p events

Figure 4.5: Multiplicity as function of trigger tower pseudorapidity. In d+Au events the bins at low multiplicity are populated for $\eta_{\text{trigger}} > 0.7$.

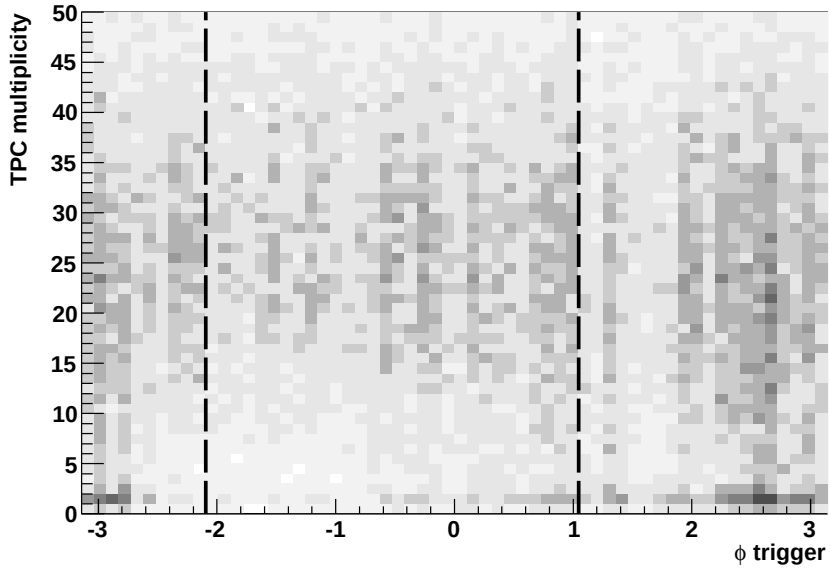

(a) d+Au events

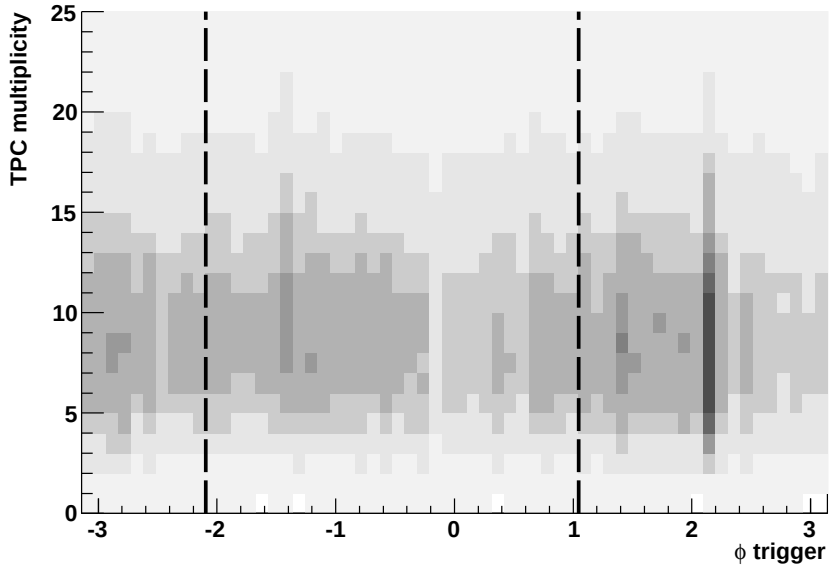

(b) p+p events

Figure 4.6: Multiplicity as function of trigger tower azimuthal angle. In d+Au events the bins at low multiplicity are populated for $\phi_{\text{trigger}} \in [-\pi, -2\pi/3]$ and $\phi_{\text{trigger}} \in [\pi/3, \pi]$.

4.4 Energy correction

The importance of γ–jet events has been explained in section 2.3. The identification of prompt photons is difficult because of the large production of decay photon. The present work focuses on inclusive photon analysis, where the main contribution is given by π^0 decay photons $\pi^0 \rightarrow \gamma\gamma$.

The method here used to study jets relies on the identification of the *leading particle* and the corresponding energy measurement. Since the main contribution is given by π^0, it is important to understand how precisely we can reconstruct their energy in a correlation context.

Figure 4.7 shows the opening angle of photons for π^0 decays as a function of transverse momentum. The horizontal line indicates the tower size. Above 6 GeV/c in most of the cases both photons are contained in a single tower. Other analysis showed that a cluster of 2×2 adjacent towers is the best choice to fully reconstruct the π^0 energy [19].

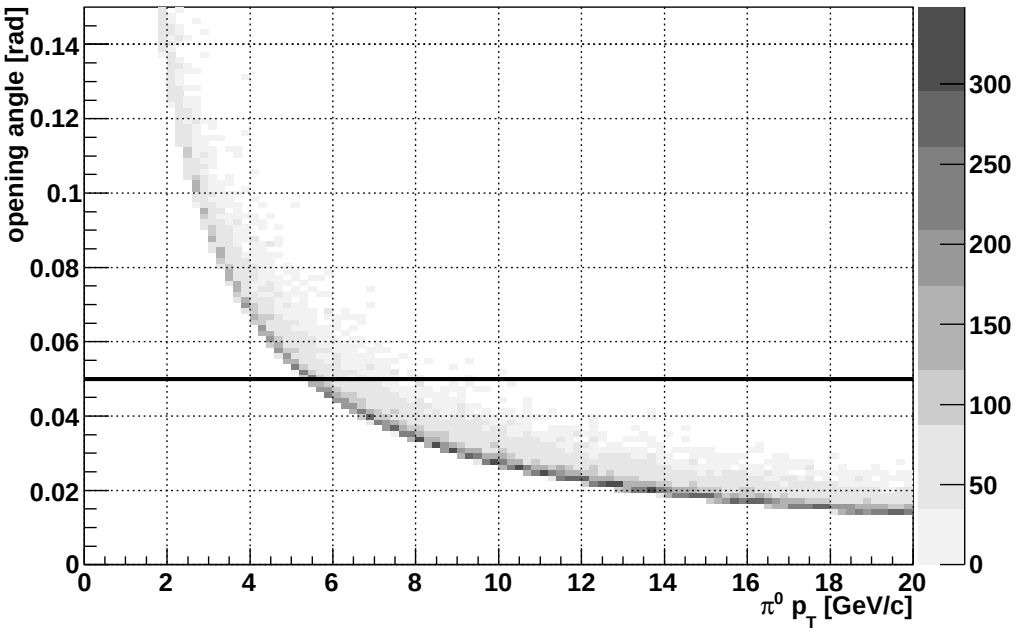

Figure 4.7: Opening angle of π^0 decay photons as a function of π^0 transverse momentum from Monte Carlo simulation. The horizontal line indicates the tower size.

Figure 4.8 shows the comparison between single towers and clusters of 4 towers for the reconstructed energy of a single π^0. The ratio between the

measurred energy and the simulated π^0 energy is plotted as a function of the measured energy. The error bar (band width) shows the root mean square deviation of the ratio distribution in each trigger energy bin. Although a single tower collects systematically less energy than the corresponding cluster, most of the energy of the simulated π^0 is collected by the trigger tower.

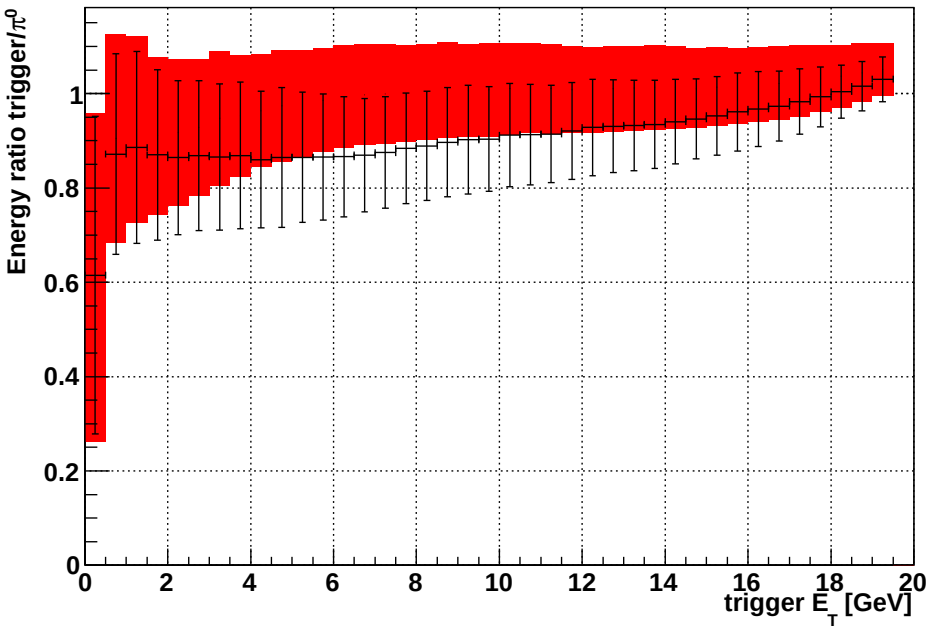

Figure 4.8: Energy ratio measured/simulated in single π^0 simulation as a function of the measured energy. The shaded boxes represent the cluster energy, while the points stand for single towers.

4.4.1 TPC veto

Particles other than π^0 could deposit energy on the triggering tower and neighbours, resulting in an overestimation of the trigger energy. To avoid an energy contamination due to other particles a TPC veto cut is applied. If the track of a charged hadron, reconstructed by the TPC, points to the trigger tower, the tower is rejected.

This procedure can modify the near–side peak, biasing the angular distribution. Moreover, as shown in [19], to fix a minimum distance between trigger tower and the closest track is much more arbitrary in p+p than in

Au+Au collisions. The multiplicity of d+Au collisions is intermediate between Au+Au and p+p collisions. Therefore, the effect of the veto is more visible in d+Au collisions compared to p+p collisions. The effects of the TPC veto on the azimuthal correlation distribution will be shown in section 5.3.

Figure 4.9 shows the distribution of primary tracks around the trigger tower. The distance in pseudorapidity is indicated as $\delta\eta$ and the distance in azimuth as $\delta\phi$. The use a small δ rather than a capital Δ should emphasize the difference from the variable $\Delta\phi$, which is frequently used for jet–like correlations, and which is measured at the vertex rather than the extrapolation to the BEMC. To express the distance from the trigger tower, the maximum norm, $\max(|\delta\phi|,|\delta\eta|)$, is preferred over the euclidian norm, $\sqrt{\delta\phi^2+\delta\eta^2}$, because it provides a square rather than a circular area, matching the shape of BEMC towers.

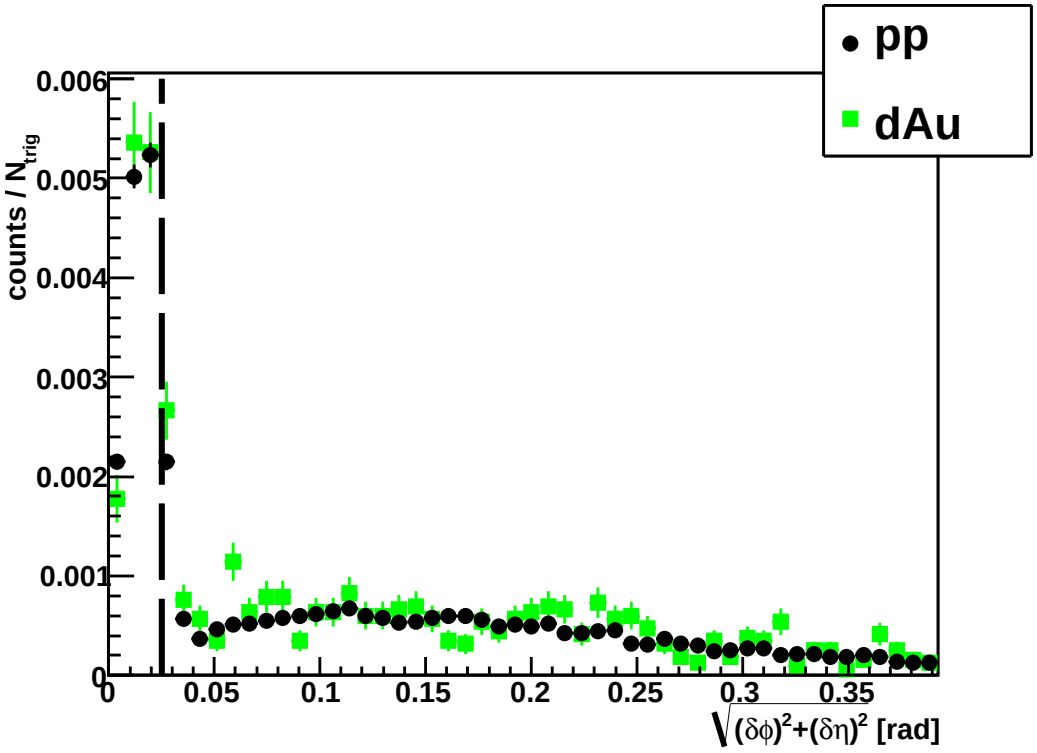

Figure 4.9: Distance of primary tracks from the center of the trigger tower in p+p and d+Au collisions. The trigger tower energy is in the interval 5.5< E_T^{trigger} <6.5 GeV, while the primary tracks momentum is greater than 1 GeV/c. The dashed line indicates the tower size.

In d+Au events as well as in p+p events, a large fraction of particles are clearly pointing to the trigger tower where they deposit a certain amount of

energy. Only towers with no tracks carrying momentum p_T>1 GeV within a distance d_{iso}=0.03 rad are considered in the present analysis, where

$$d_{iso} = \min\{\max(|\delta\phi_i|, |\delta\eta_i|) : p_T(i) > 1\text{GeV/c}\}. \quad (4.1)$$

In section 5.3 the systematic study of this cut on the azimuthal correlation distribution will be discussed.

To estimate the energy difference between the trigger tower and the π^0 activating it, p+p collision have been simulated using PYTHIA event generator [47]. The output of the PYTHIA simulation was processed with detector simulation and subsequent event reconstruction software, but also analyzed directly.

Only particles within the acceptance of the STAR TPC and the full BEMC ($|\eta|$ <1) were used. For each event a geometrical match between the most energetic π^0 (*leading* π^0) and the trigger tower has been searched. If the leading π^0 matches the trigger tower, their energies are compared. Figure 4.10 shows the comparison between single tower and cluster of 4 towers for the reconstructed energy of the leading π^0.

As shown in figure 4.8, the energy ratio measured/(simulated π^0) is plotted as a function of the measured energy. The error bar (band width) shows the root mean square deviation of the ratio distribution in each trigger energy bin. The contribution of other particles is clearly visible and the difference between single tower and cluster is less pronounced.

In this analysis the ratio extracted from figure 4.10 has been used as correction factor for the trigger tower energy. It was found to be in average

$$E_T^{\text{trigger}} = 0.94 \pm 0.03 E_T^{\pi^0}. \quad (4.2)$$

The hypotesis of constant value is reasonable, within the errors, for single tower energy as shown in figure 4.8.

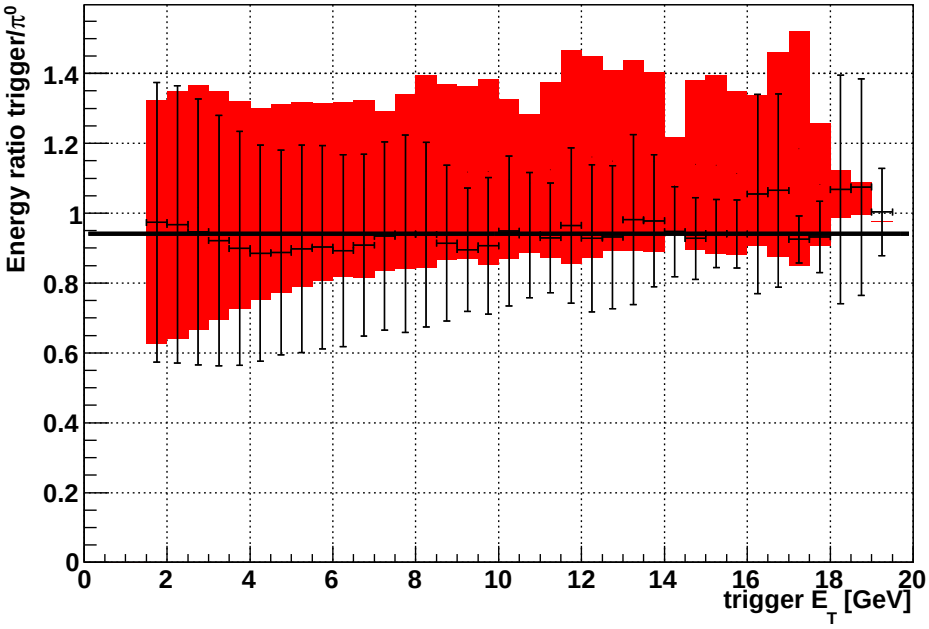

Figure 4.10: Energy ratio measured/simulated in full p+p event simulation as a function of the measured energy. The shaded boxes represent the cluster energy, while the points stand for single towers. The solid line is a linear fit on the single towers point: on average 94% of trigger π^0 energy is measured by the trigger tower

Chapter 5

Azimuthal correlation analysis

This chapter explains how the azimuthal correlation analysis is performed: in section 5.1 the azimuthal angular correlation is calculated selecting a trigger particle and associated particle from the events identified as described in chapter 4. The raw correlation distribution is analyzed as explained in section 5.2, and the results will be shown in chapter 6 for both p+p and d+Au collisions.

Section 5.3 will present a systematic study on the effects of charged particle veto on the azimuthal correlation. In section 5.4 the effects of beam background events will be studied.

5.1 Trigger and associated particle selection

Ideally one would want to select as trigger the leading particle in a jet. This is generally not possible due to trigger efficiency and limited acceptance. In this analysis a high energy deposit in the BEMC is used as trigger. This will represent in most cases a π^0, which should frequently be the leading particle. The analysis will necessary miss most cases where the leading particle is a different hadron (i.e. $\pi^{\pm}$). In these cases the π^0 will be a second leading.

For each accepted track in the event, the correlation angle with the trigger is computed $\Delta\phi = \phi_{trigger} - \phi_{associated}$. A differential analysis is performed, calculating $\Delta\phi$ as a function of E_T^{trig} and p_T^{assoc}. If $p_T^{\text{assoc}} > E_T^{\text{trig}}$, the particle is rejected. This excludes cases where the π^0 is clearly not the leading particle.

5.2 Azimuthal correlation function

The azimuthal distribution between trigger and associated particles is defined as in equation 2.1. A typical $\Delta\phi$ distribution in p+p collisions is plotted in

figure 5.1. As shown in section 2.2 the distribution has a peak at $\Delta\phi$=0 (*near side*) and one at $\Delta\phi$=π (*away side*). Between the peaks background entries due to tracks not belonging to the di–jet structure are found – the so–called underlying event.

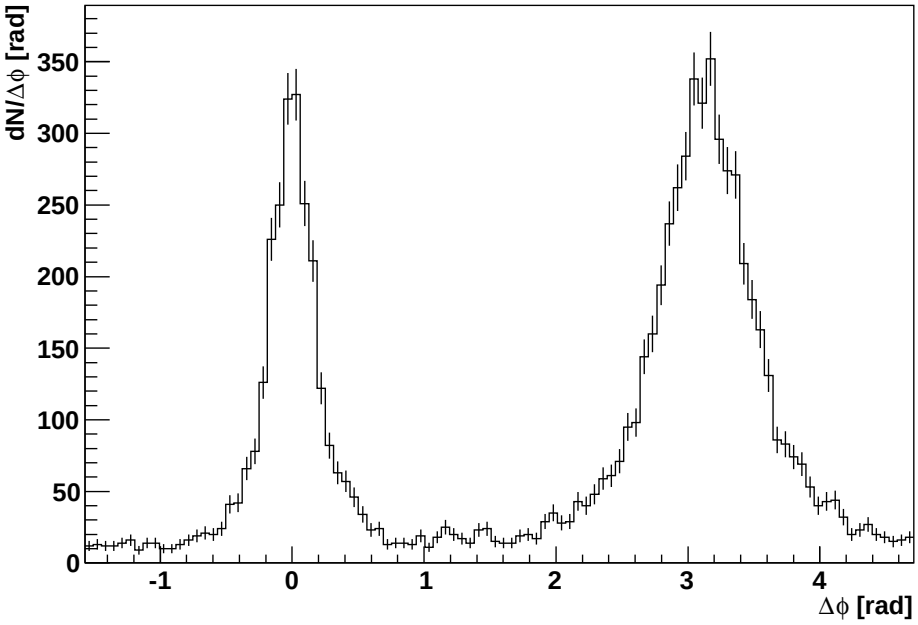

Figure 5.1: Raw azimuthal angular correlation distribution in p+p collisions for $6.5<E_T^{\text{trig}}<7.5$ GeV and $2<p_T^{\text{assoc}}<3$ GeV/c.

In the high–p_T region the peak shape can be reasonably well described with a Gaussian distribution. Therefore, the azimuthal angle distribution is parameterized as

$$D(\Delta\phi) = \frac{1}{N_{\text{trigger}}}\frac{1}{\varepsilon}\left(\frac{Y_{\text{near}}}{\sqrt{2\pi}\sigma_{\text{near}}}e^{-\frac{1}{2}\left(\frac{\Delta\phi}{\sigma_{\text{near}}}\right)^2} + \frac{Y_{\text{away}}}{\sqrt{2\pi}\sigma_{\text{away}}}e^{-\frac{1}{2}\left(\frac{\Delta\phi-\pi}{\sigma_{\text{away}}}\right)^2} + B\right) \tag{5.1}$$

where N_{trigger} is the number of trigger particles and ε=0.89 [48] is the track reconstruction efficiency in the TPC. The first term in parenthesis represents the near side peak, the second the away side peak, and the third (B) is a constant term to describe the uncorrelated background. The near–side peak position is fixed to $\Delta\phi = 0$ and the away side to $\Delta\phi = \pi$. Therefore, to fit the azimuthal distribution, only five parameters are free: the yields Y_{near} and Y_{away} of the two peaks, their width σ_{near} and σ_{away} and the constant term B.

A flat distribution, normalized to $2\pi B$, is subtracted in the whole $\Delta\phi$ interval, in order to remove the uncorrelated background. The cylindric symmetry of the detector makes the uncorrelated background along the azimuthal angle uniformly distributed. To prove this a trigger tower from one event can be correlated with the tracks from a different event. The resulting distribution is flat (figure 5.2).

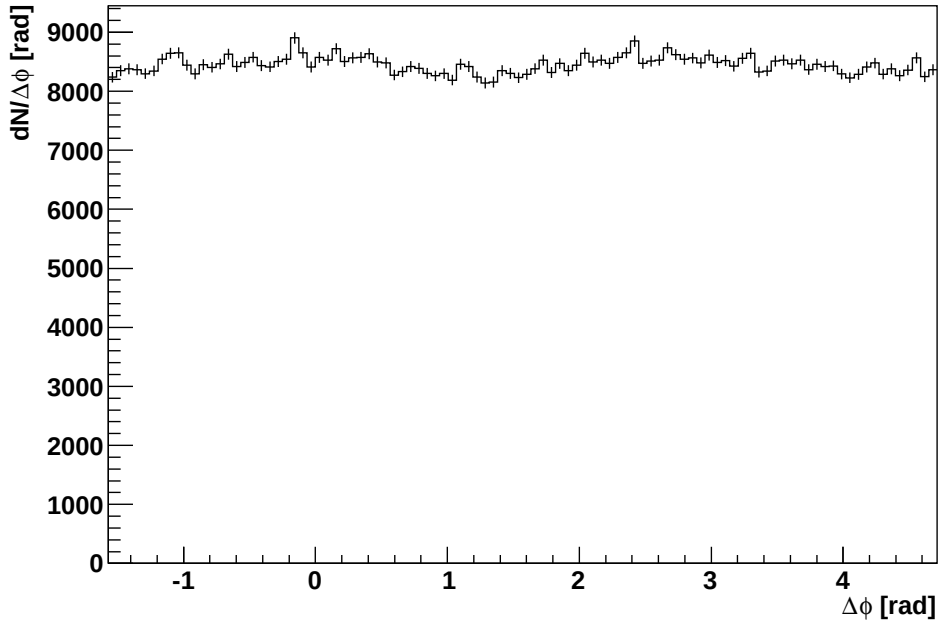

Figure 5.2: Uncorrelated background in p+p collisions for $4.5<E_T^{\text{trig}}<6.5$ GeV and $2<p_T^{\text{assoc}}<3$ GeV/c. The distribution is obtained correlating the trigger from one event with the tracks from a different one.

The $\Delta\phi$ distribution after background subtraction is normalized by the number of triggers and the track reconstruction efficiency. Figure 5.3 shows the distribution after background subtraction and after the normalization. The parameters which describe the distribution, yields and widths, can now be extracted.

The Gaussian approximation does not describe all correlation function equally well. To avoid biases due to an imperfect fit the histograms are analyzed numerically in the range $\pm 3\sigma$ of the Gaussian fit:

$$yield = \sum_{i}^{N} n_i, \tag{5.2}$$

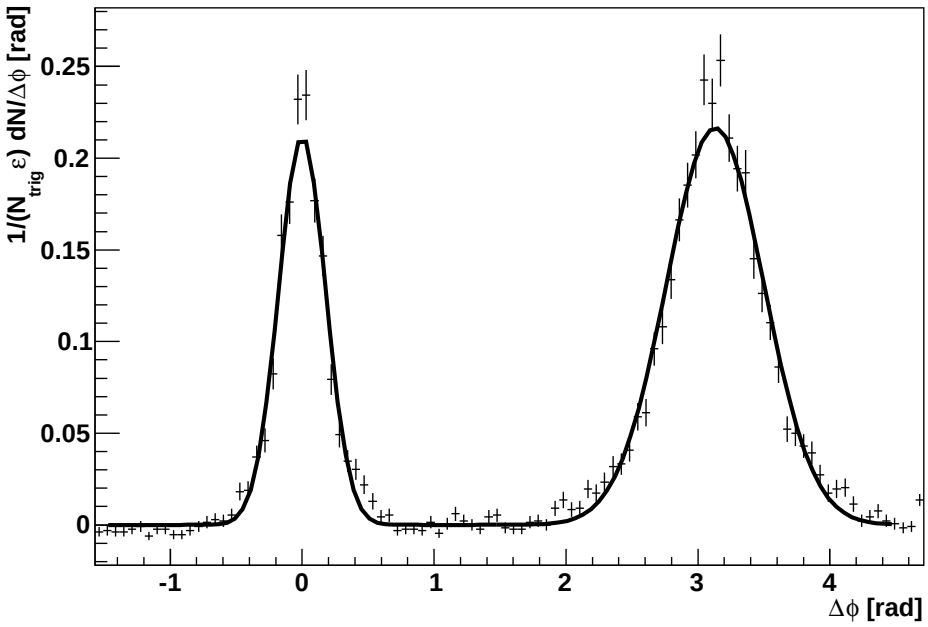

Figure 5.3: Azimuthal correlation distribution after background subtraction and normalization in p+p collisions for 6.5<E_T^{trig}<7.5 GeV and 2<p_T^{assoc}<3 GeV/c. The histogram is fitted with the function described in equation (5.1)

where n_i is the content of each bin. The width are calculated as standard deviation in the same range

$$width = \sqrt{\frac{1}{N}\sum_{i}^{N}(x_i - x_{mean})^2 n_i}, \tag{5.3}$$

where n_i is the content of each bin and x_i the postion of the bin. For the near side peak x_{mean}=0, for the away side $x_{mean} = \pi$.

In the highest E_T^{trig} and p_T^{assoc} bin (E_T^{trig}>7.5 GeV and p_T^{assoc}>6 GeV/c), where the statistic is low (less than 100 entries), the initial Gaussian fit is difficult to perform. In this case the integration range has been fixed to [-0.45,0.45] for the near side and [π-1.2,π+1.2] for the away side. These values have been chosen according to the fit results in the other energy intervals.

5.3 Effects of charged particle veto on the azimuthal correlation distribution

As seen in section 4.4.1, applying a TPC veto interferes with the charged particle distribution around the trigger tower. The veto affects the yields as much as the width of the near–side peak. Figure 5.4 shows an example of the near side width as a function of $d_{\rm iso}$ defined in equation (4.1). The widths for d+Au collisions increase for $d_{\rm iso}$ <0.03, then they stabilize. In parallel the yields decreases for $d_{\rm iso}$ <0.03 (figure 5.5), then they stabilize. This value is in agreement with previous analysis [19]. The square veto area defined by this cut measures 0.06×0.06 in $\delta\phi$ and $\delta\eta$, and is slightly larger than a single tower.

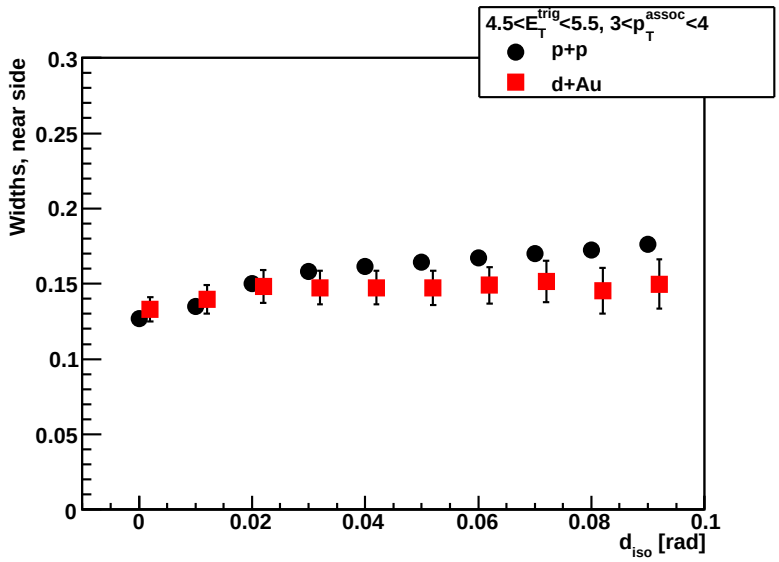

Figure 5.4: Near–side width as a function of the the minimum distance from the center of the trigger tower within no track with p_T<1 GeV/c is allowed. In this example 4.5< $E_T^{\rm trigger}$ <5.5 GeV and 3< $p_T^{\rm associated}$ <4 GeV/c. The points for d+Au are horizontally shifted for a better visualization.

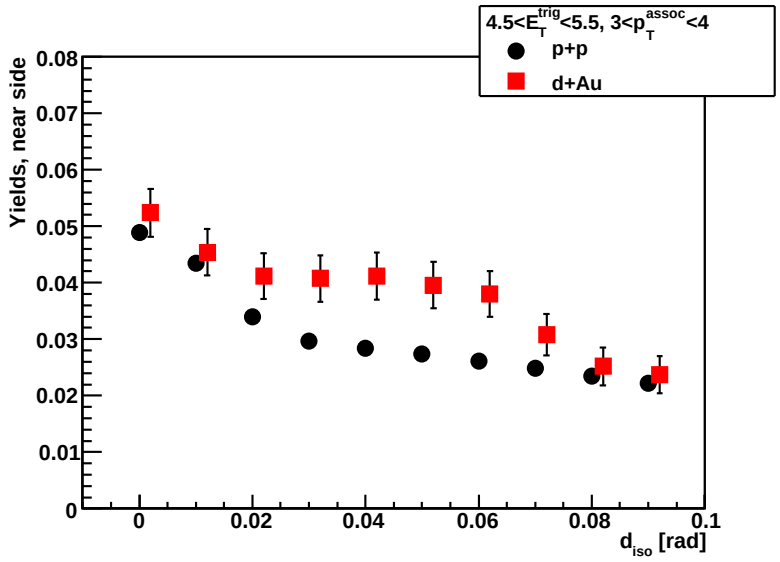

Figure 5.5: Near–side yield as a function of the the minimum distance from the center of the trigger tower within no track with p_T<1 GeV/c is allowed. In this example 4.5< E_T^{trigger} <5.5 GeV and 3< $p_T^{\text{associated}}$ <4 GeV/c. The points for d+Au are horizontally shifted for a better visualization.

As explained in section 4.4.1, the TPC veto excludes also tracks which belong to the near side jet. As consequence the yield measured for d_{iso} >0.03 is lower than the correct one. This induces a systematic error which can be evaluated comparing the values used in the analysis with the correct theoretical yield value obtained without apply any veto.

In the hypothesis that for d_{iso} >0.03 the yield decreases linearly with d_{iso}, the correct value for d_{iso} =0 is obtained evaluating the function

$$f(d_{\text{iso}}) = a \cdot d_{\text{iso}} + b. \tag{5.4}$$

The contribution ε_{cpv} of the charged particle veto to the yield measurement efficiency is defined as the ratio between $f(0)$ and the yield measured for d_{iso}=0.03. Figure 5.6 shows the reconstruction efficiency in p+p and d+Au collisions. The final results are corrected bin by bin for the appropriated ε_{cpv}. The error on ε_{cpv} value is used as estimation of the systematic error.

A similar procedure can be applied to the widths. In this case the difference between $f(0)$ and the width measured for d_{iso}=0.03 is assumed as systematic error. The estimated errors are plotted in figure 5.7 for p+p and d+Au collisions.

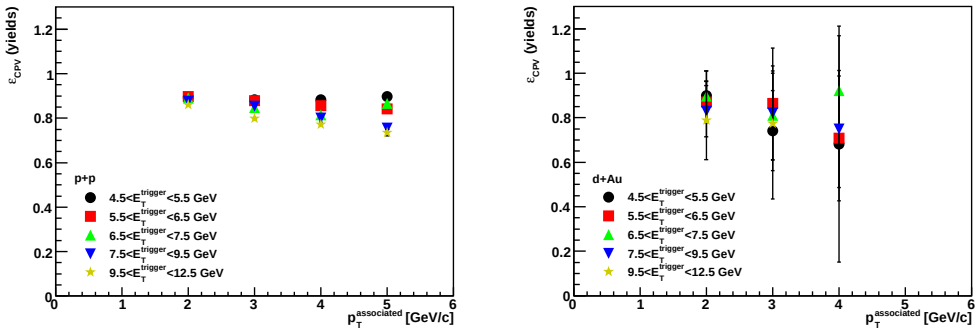

(a) p+p collisions **(b)** d+Au collisions

Figure 5.6: Charged particle veto correction in p+p (left) and d+Au (right) data. The points indicate the correction factor ε_{cpv} applied to the data.

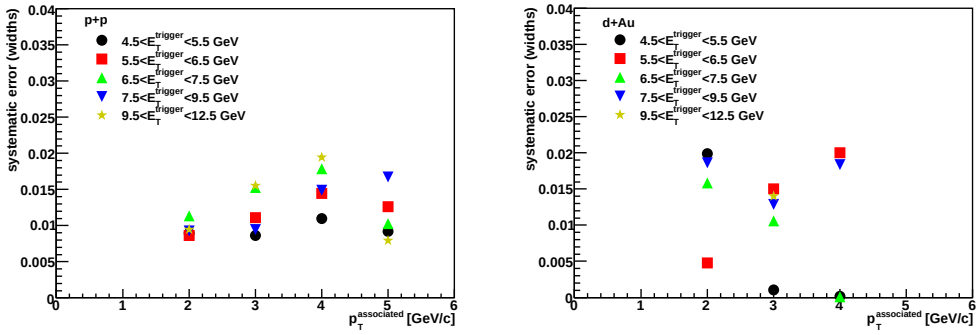

(a) p+p collisions **(b)** d+Au collisions

Figure 5.7: Systematic error on widths due to charged particle veto cut.

5.4 Effects of background on the azimuthal correlation distribution

The background described in section 4.3 is characterized by a high energy deposit on the BEMC without a corresponding deposition on the TPC. The result in term of azimuthal correlation is the increase in the number of trigger towers without associated particles and, therefore, the decrease of the yields. In the following sections the yields measured when applying a single cut will be compared to the yield measured when all the final cut on the background are applied.

5.4.1 Single cuts

Energy ratio

Section 4.3.1 explains how the background can be described as function of the TPC and the BEMC energy. Figure 5.8 shows the near–side yields and the away–side yields respectively for several E_T^{trigger} energy bin. In each E_T^{trig} bin and p_T^{assoc} bin the ratio with the yield obtained with all cut applied is calculated. Yields increase with the energy ratio. This effect is due to the reduction of the background. On the other side the cut on the energy ratio introduces a bias to higher multiplicity events. In section 5.4.2 the contribution of this bias to the systematic uncertainties will be evaluated.

The events with a ratio E_{TPC}/E_{BEMC} <0.2 are considered background events and not considered in the systematic error estimation.

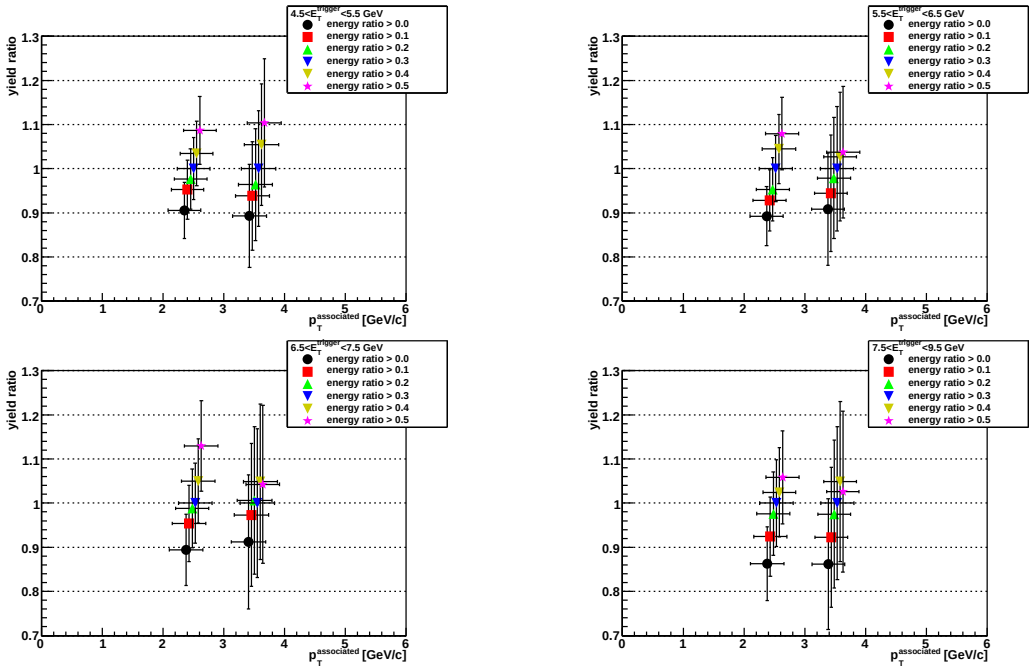

Figure 5.8: Yield ratios for different E_T^{trigger} bin as function of $p_T^{\text{associated}}$ and the energy ratio E_{TPC}/E_{BEMC}. The reference value is the yield measured once the cuts on the ratio E_{TPC}/E_{BEMC} and on the trigger tower position have been applied. The points are artificially shifted along x–axis for a better visualization.

Trigger tower position

Background events are characterized by a low TPC multiplicity as explained in section 4.3.2. The trigger towers of background events are localized in specific areas of the BEMC. In particular towers with pseudorapidity η >0.7 and azimuth $\phi \notin [-2\pi/3, \pi/3]$ are associated with low multiplicity events. For each energy bin and pseudorapidity cut the measured yield is compared to the yield obtained when all the optimal cuts are applied. The results are shown in figure 5.9.

The same procedure is applied for the azimuthal cut and the results are shown in figure 5.10. In this case the reduced size of the azimuthal range selected for each cut produces a low statistic with consequent greater errors.

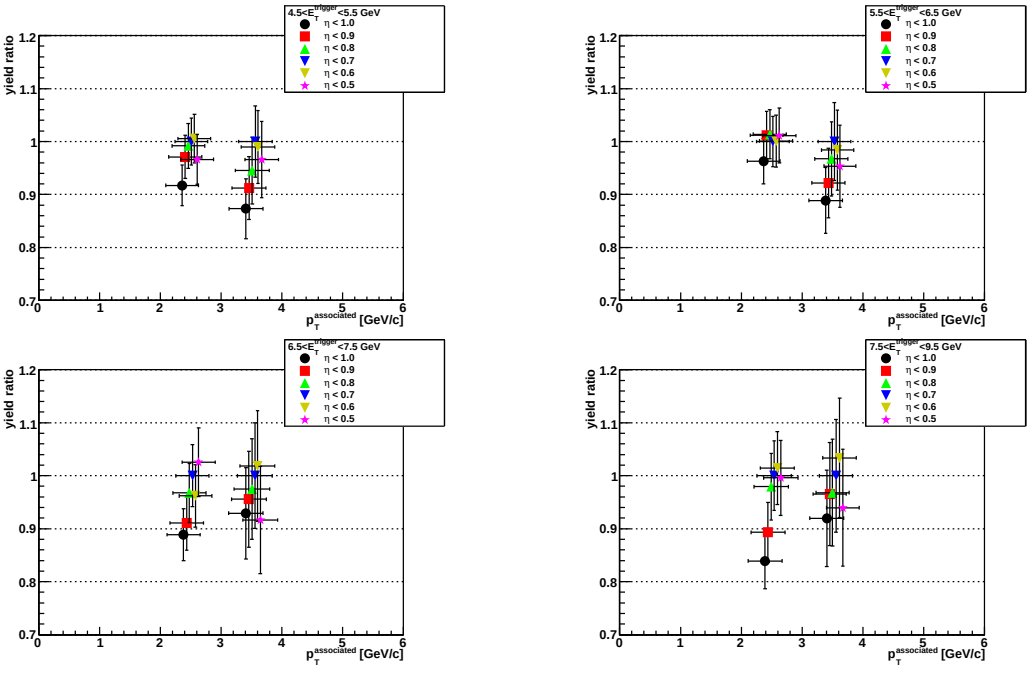

Figure 5.9: Yield ratios for different E_T^{trigger} bin as function of $p_T^{\text{associated}}$ and the cut on the trigger tower pseudorapidity η. The reference value is the yield measured once the cuts on the ratio E_{TPC}/E_{BEMC} and on the trigger tower position have been applied. The points are artificially shifted along x–axis for a better visualization.

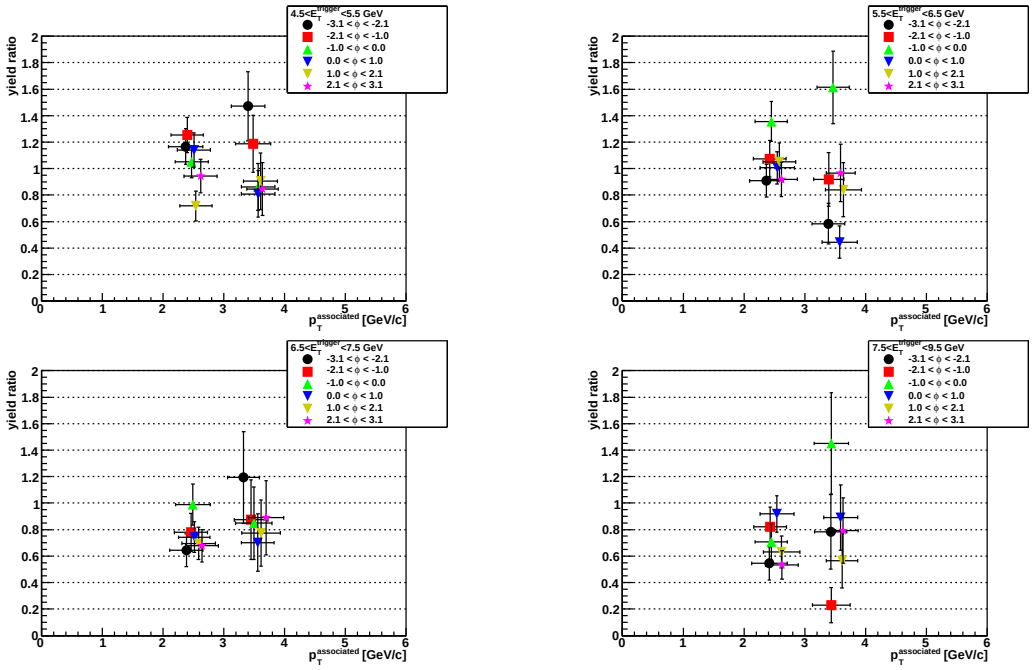

Figure 5.10: Yield ratios for different E_T^{trigger} bin as function of $p_T^{\text{associated}}$ and the cut on thr trigger tower azimuthal position ϕ. The reference value is the yield measured once the cuts on the ratio E_{TPC}/E_{BEMC} and on the trigger tower position have been applied. The points are artificially shifted along x–axis for a better visualization.

5.4.2 Conditional cuts

In the final analysis all the previous cut are applied together. Since they work in the same direction, the resulting fluctuations due to a single cut are attenuated by the other cut.

In figure 5.11 the effect of each cut is compared to the final result obtained applying all the selected cuts. For each cut the ratio

$$\frac{yield\,(r,\phi,\eta)}{yield\,(r_0,\phi_0,\eta_0)} \tag{5.5}$$

is shown, where $r = E_{TPC}/E_{BEMC}$, and the index 0 indicate the selected values. These correspond to

$$\begin{aligned} r_0 &: \; r > 0.3 \\ \phi_0 &: \; \phi \in [-2\pi/3, \pi/3] \\ \eta_0 &: \; \eta < 0.7. \end{aligned}$$

Based on the observed variations, the systematic error associated to background events is fixed to $[+11\%, -38\%]$. These errors are applied to the results that will be presented in chapter 6.

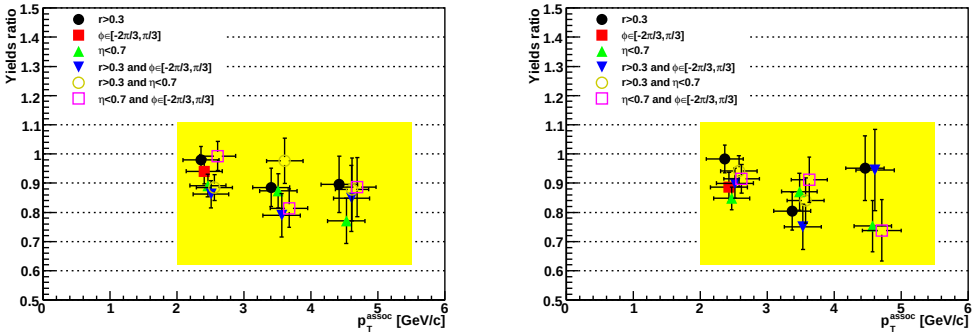

(a) 4.5<E_T^{trig}<5.5 GeV

(b) 5.5<E_T^{trig}<6.5 GeV

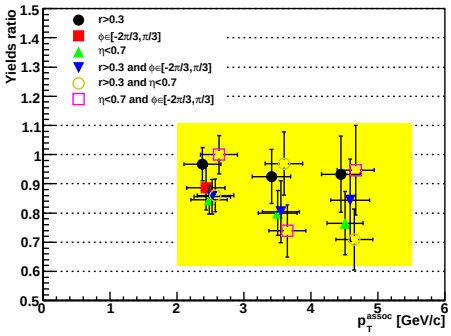

(c) 6.5<E_T^{trig}<7.5 GeV

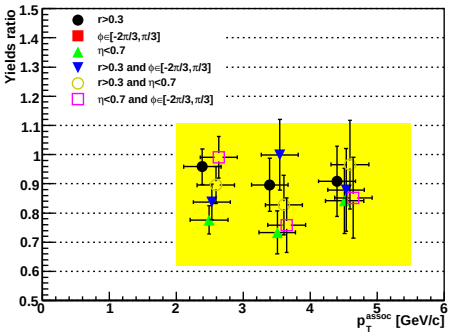

(d) 7.5<E_T^{trig}<9.5 GeV

Figure 5.11: Yields ratio for different cut E_T^{trigger} bin as function of $p_T^{\text{associated}}$. The reference value is the yield measured once the cuts on the ratio E_{TPC}/E_{BEMC} and on the trigger tower position have been applied. The points are artificially shifted along x–axis for a better visualization. The shaded band correspond to the systematic uncertainty assigned to yields.

Chapter 6

Jet properties

The previous chapter explained how the azimuthal correlation is performed and how the charged particle veto cut (see also section 4.4.1) and the backgrounds cut can modify the results. In this chapter the extracted yield and widths are compared for p+p collisions and d+Au collisions. In section 6.2 the results from γ–charged hadron correlation in p+p collisions are compared to di–charged hadron correlation in d+Au collisions.

Sections 6.3 and 6.4 will present the results for the distance $\sqrt{\langle j_T^2 \rangle}$ between the trigger particle and the initial parton, and the jet acoplanarity $\sqrt{\langle k_T^2 \rangle}$, comparing them with previous measurements.

6.1 Photon-charged hadron azimuthal correlation

Figures 6.1 and 6.2 show the azimuthal correlation function after background subtraction, normalized by the number of triggers and corrected for the efficiency as in (2.1). Panels 6.1(a) and 6.1(b) show the behavior of the distribution when changing the $E_T^{\rm trig}$ range in d+Au and p+p events respectively. Panel 6.2(a) and 6.2(b) show the behavior of the distribution when changing the $p_T^{\rm assoc}$ range in d+Au and p+p events respectively.

The distributions show the behavior expected for di–jet event, with a near–side peak centered at $\Delta\phi$=0 and an away–side peak at $\Delta\phi$=π. The peak height decreases with $p_T^{\rm assoc}$ and it increases with $E_T^{\rm trig}$ while the widths are more sensitive to $p_T^{\rm assoc}$. The observations are in qualitative agreement with expectations from di–jet fragmentation, in which most energetic particles lie closer to the leading one, and thereby the width decreases with $p_T^{\rm assoc}$. Higher $E_T^{\rm trig}$ tags more energetic jets so a greater multiplicity is expected.

Yields and widths of near–side and away–side peaks are determined as a

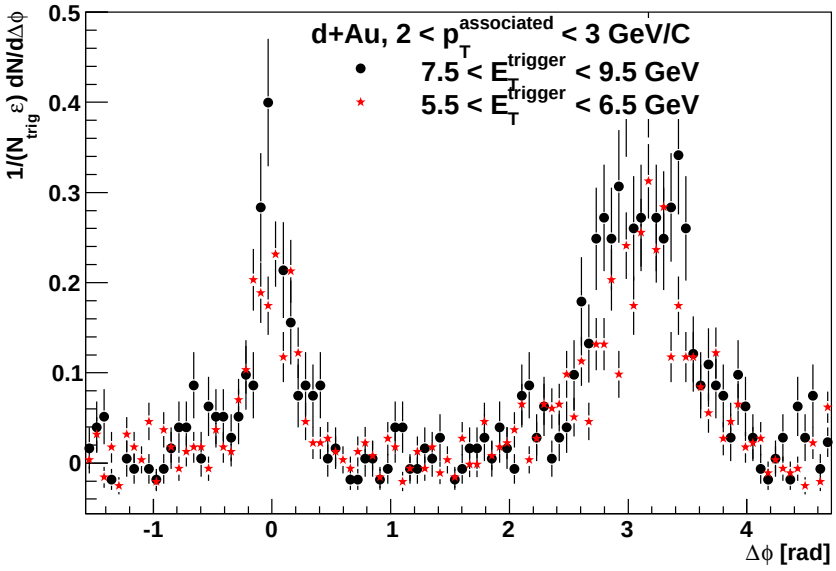

(a)

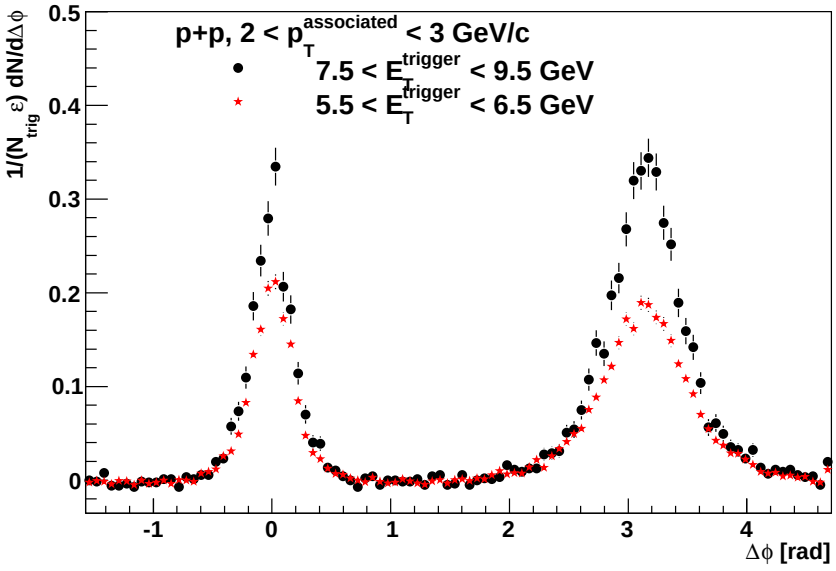

(b)

Figure 6.1: Azimuthal correlation distribution for 2< $p_T^{\text{associated}}$ <3 GeV/c and 5.5< E_T^{trigger} <6.5 GeV or 7.5< E_T^{trigger} <9.5 GeV. In panel (a) the distribution for d+Au collisions is shown. Panel (b) shows the same for p+p events.

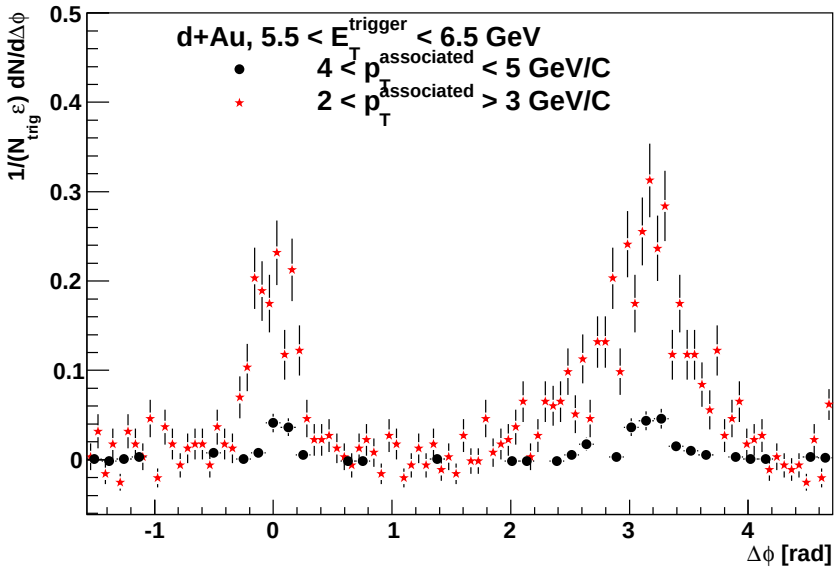

(a)

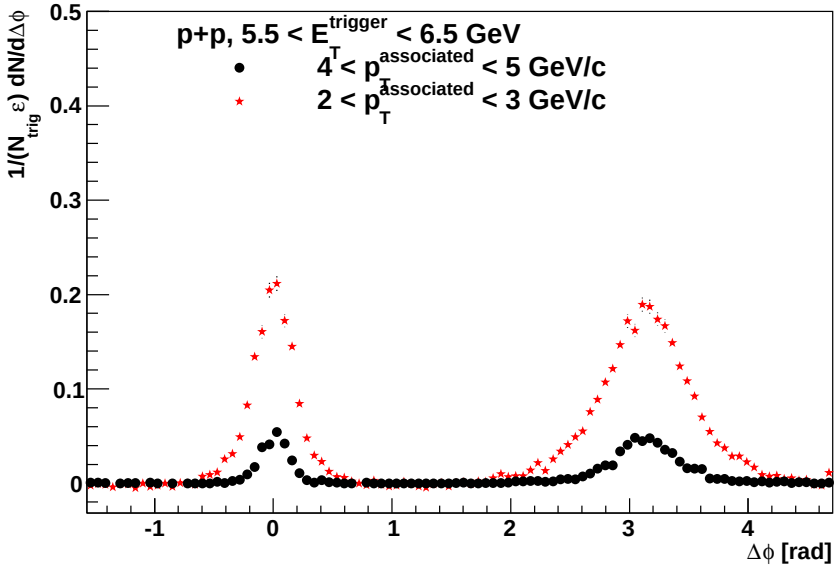

(b)

Figure 6.2: Azimuthal correlation distribution. The trigger energy is fixed (5.5< E_T^{trigger} <6.5 GeV) and the distribution is plotted for 2< $p_T^{\text{associated}}$ <3 GeV/c and 4< $p_T^{\text{associated}}$ <5 GeV/c for d+Au (panel (a)) and for p+p events (panel (b)).

function of energy of both trigger towers and associated tracks. Figure 6.3 and 6.4 show the behavior of correlation yields and width, respectively, for p+p events, while 6.5 and 6.6 show correlation yield and width for d+Au events.

The near side peak is narrower than the away-side peak in each $E_T^{\rm trig}$ and $p_T^{\rm assoc}$ bin. As observed for the raw distributions, the peak width decreases with $p_T^{\rm assoc}$: high-p_T particle are close to leading particle. The peaks get narrower with increasing $E_T^{\rm trig}$. This is consistent with the idea of getting more energetic associated particle in the more energetic jets. Moreover, for higher-p_T triggers, the trigger particle is closer to the jet axis and than it narrows the trigger-associated correlation peak. The correlation peak widths for γ-charged hadron and charged di-hadron correlations are similar (section 6.2.

The results for p+p events are compared to the results for d+Au events (figure 6.7, 6.8, 6.9 and 6.10). In all energy and p_T ranges the results for the two datasets are in agreement for the correlation yields as well as for the widths. The jet production in the two systems is equivalent. Therefore, all the conclusions of the following analysis, which are performed mainly on p+p events for statistical reasons, are valid for both datasets.

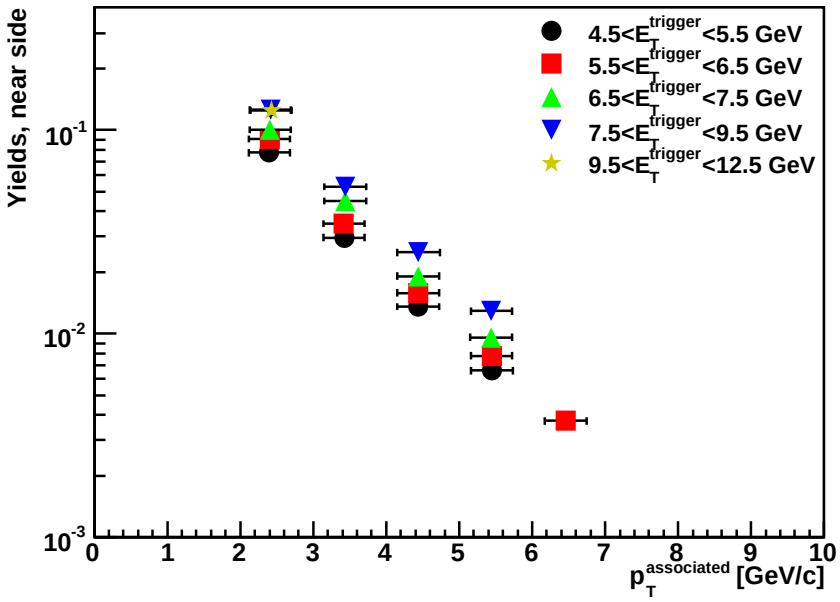

(a) near side

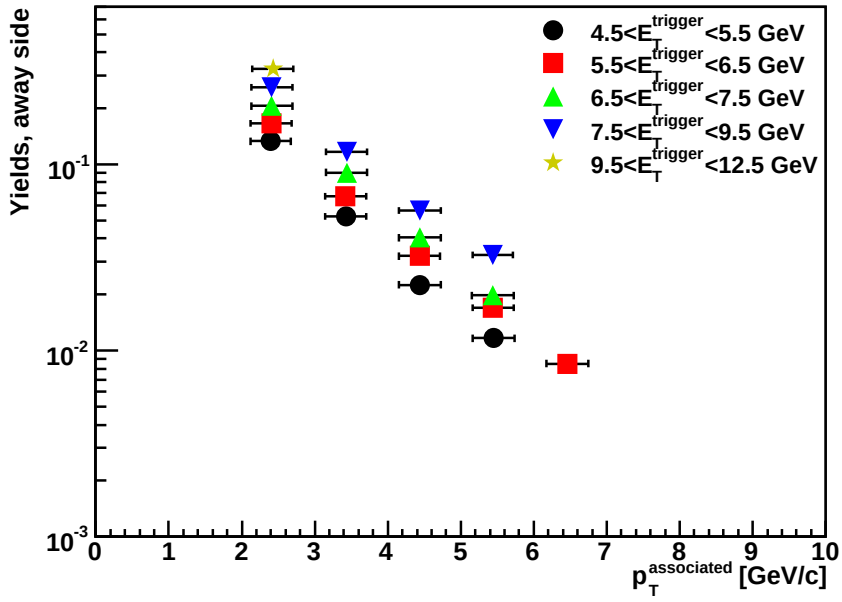

(b) away–side

Figure 6.3: Correlation yield in p+p collisions, as a function of $p_T^{\text{assoc}}$for several E_T^{trig} ranges. Figure (a) shows the yields for near–side peak, figure (b) for the away–side. Only statistical errors are shown.

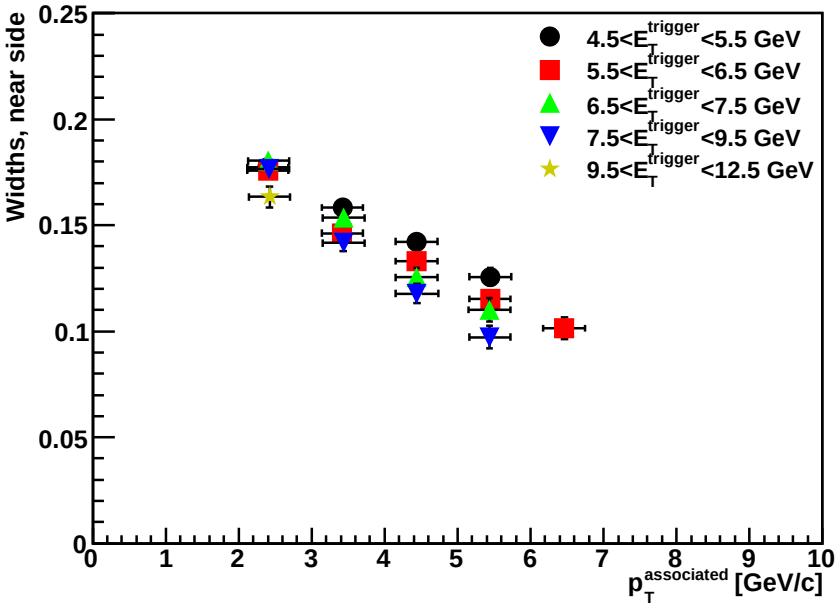

(a) width near–side

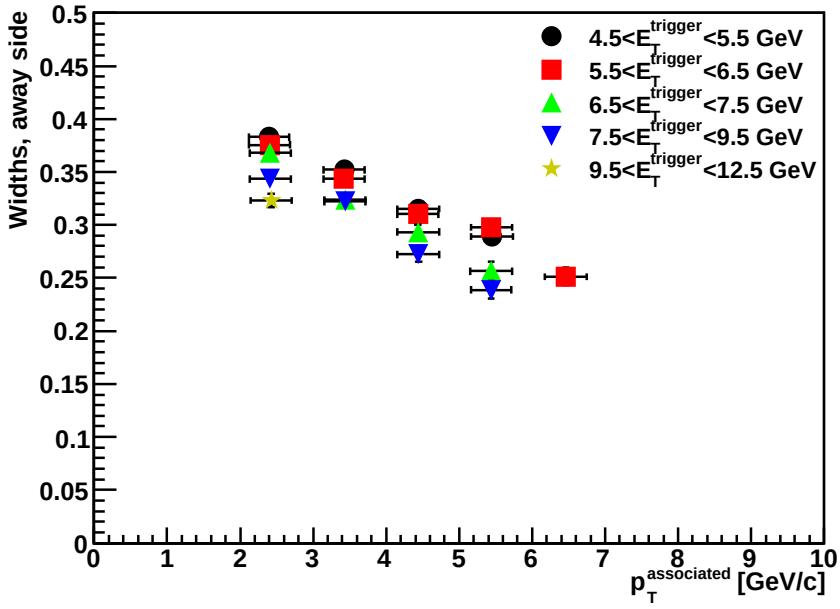

(b) width away–side

Figure 6.4: Width in p+p collisions, as a function of $p_T^{\text{assoc}}$for several E_T^{trig} ranges. Figure (a) shows the widths for near–side peak, figure (b) for the away–side. Only statistical errors are shown.

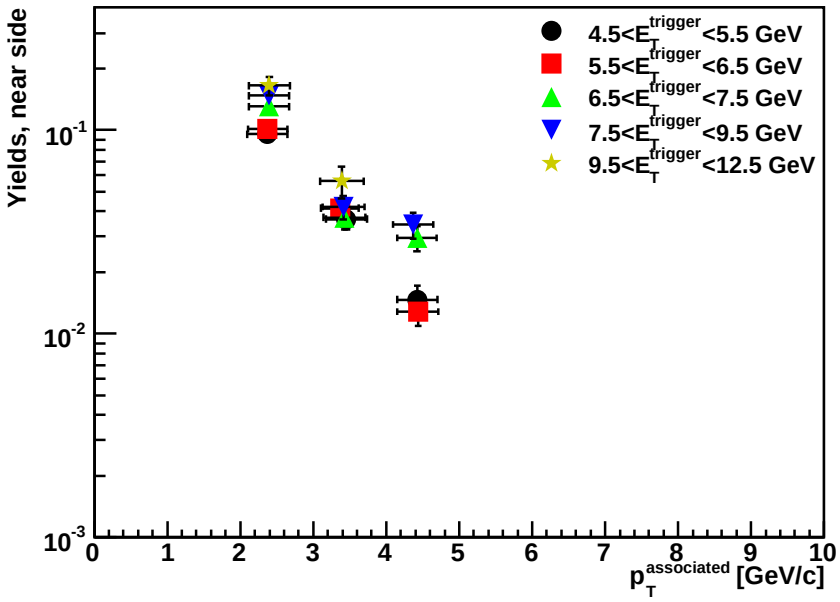

(a) near–side

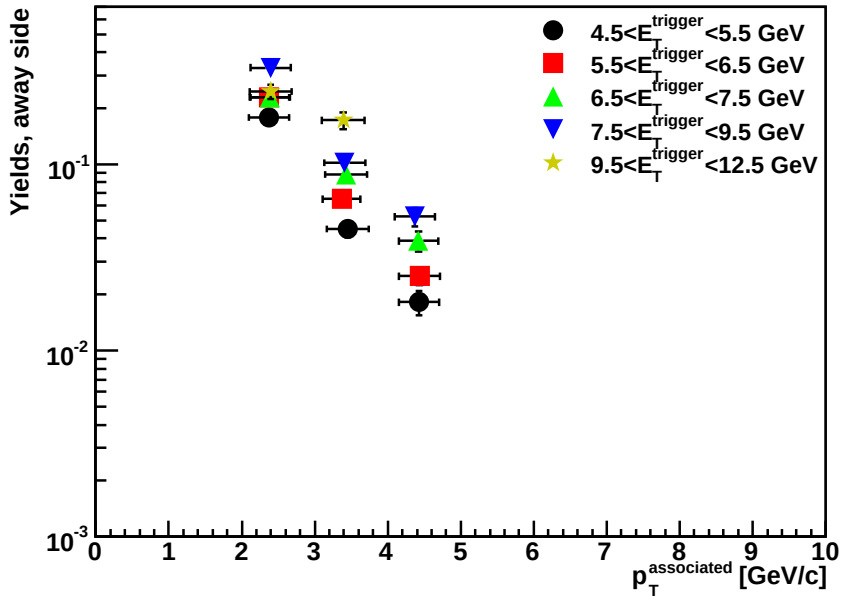

(b) away–side

Figure 6.5: Correlation yield in d+Au collisions, as a function of $p_T^{\text{assoc}}$for several E_T^{trig} ranges. Figure (a) shows the yields for near–side peak, figure (b) for the away–side. Only statistical errors are shown.

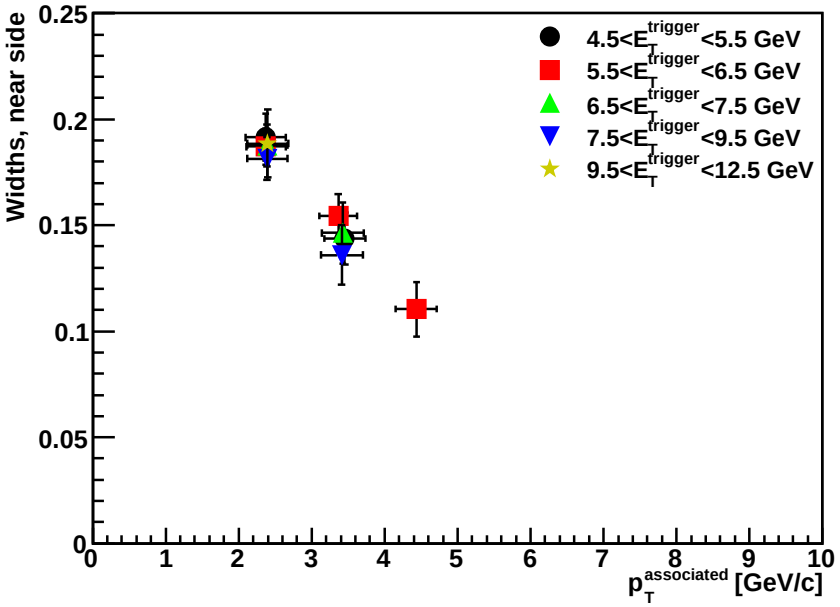

(a) width near–side

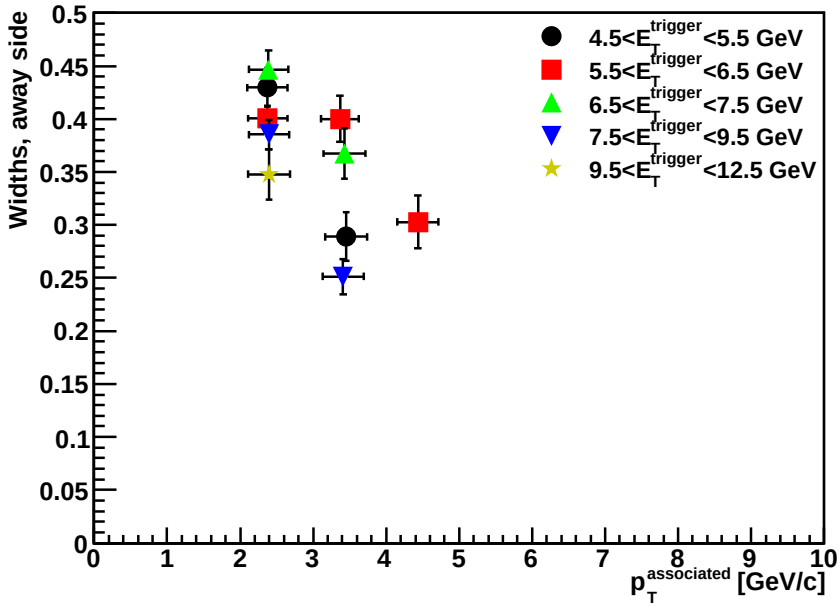

(b) width away–side

Figure 6.6: Width in d+Au collisions, as a function of p_T^{assoc} for several E_T^{trig} ranges. Figure (a) shows the widths for near–side peak, figure (b) for the away–side. Only statistical errors are shown.

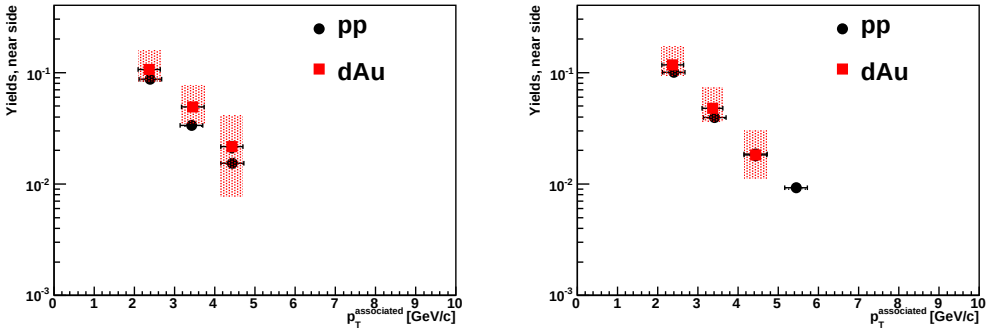

(a) 4.5<E_T^{trig}<5.5 GeV

(b) 5.5<E_T^{trig}<6.5 GeV

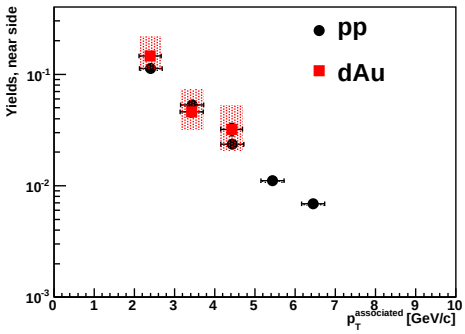

(c) 6.5<E_T^{trig}<7.5 GeV

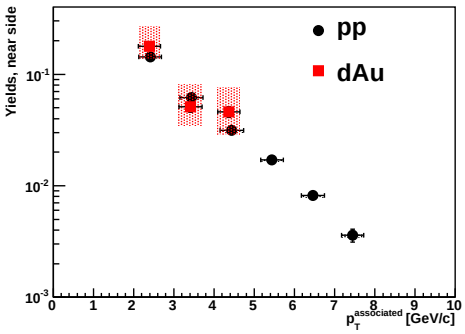

(d) 7.5<E_T^{trig}<9.5 GeV

Figure 6.7: Comparison of the near–side yields in d+Au and p+p events for different E_T^{trig} bins.

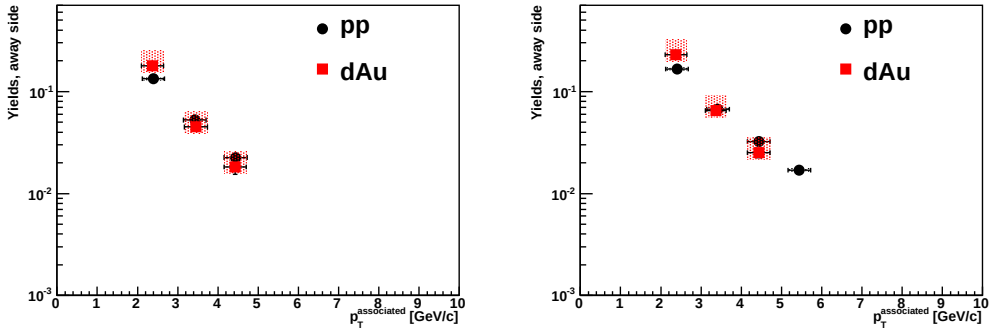

(a) 4.5<E_T^{trig}<5.5 GeV

(b) 5.5<E_T^{trig}<6.5 GeV

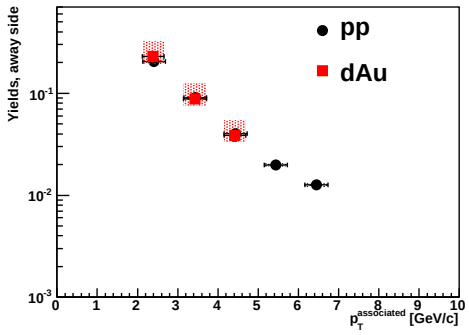

(c) 6.5<E_T^{trig}<7.5 GeV

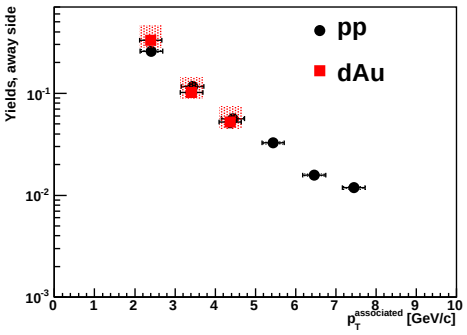

(d) 7.5<E_T^{trig}<9.5 GeV

Figure 6.8: Comparison of the away–side yields in d+Au and p+p events for different E_T^{trig} bins.

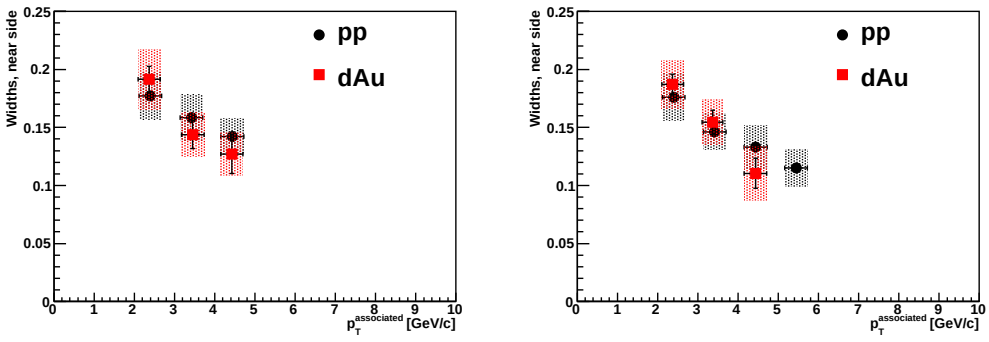

(a) 4.5<E_T^{trig}<5.5 GeV

(b) 5.5<E_T^{trig}<6.5 GeV

(c) 6.5<E_T^{trig}<7.5 GeV

(d) 7.5<E_T^{trig}<9.5 GeV

Figure 6.9: Comparison of the away–side widths in d+Au and p+p events for different E_T^{trig} bins.

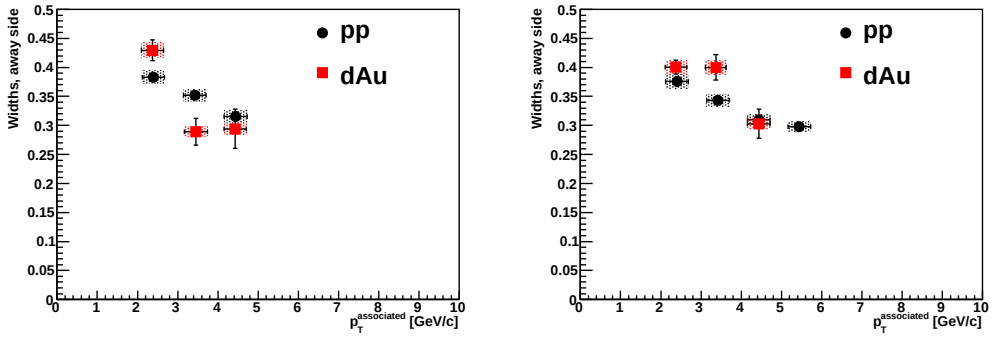

(a) 4.5<E_T^{trig}<5.5 GeV

(b) 5.5<E_T^{trig}<6.5 GeV

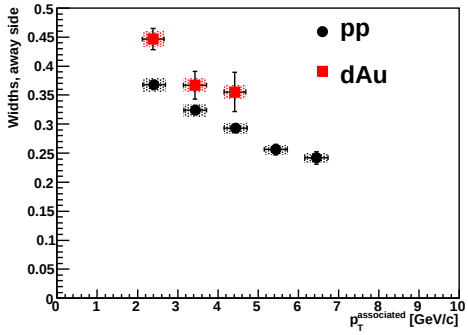

(c) 6.5<E_T^{trig}<7.5 GeV

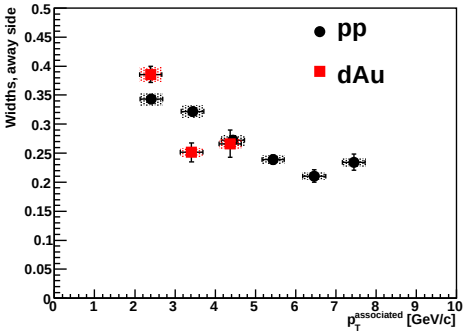

(d) 7.5<E_T^{trig}<9.5 GeV

Figure 6.10: Comparison of the away–side widths in d+Au and p+p events for different E_T^{trig} bins.

6.2 Charged hadron pair correlation

The TPC of STAR has a good momentum resolution also at high p_T, as seen in section 3.3. It allows therefore to perform correlation studies of pairs of charged hadron — called also charged–charged correlation in what follows. This allows a comparison of the behavior of jets with a neutral trigger or a charged trigger and leads to the study of isospin dependence.

Peak yields and widths are expected to be comparable in neutral–charged hadron correlation (for brevity *tower–charged correlation*) and charged–charged correlation. To make the comparison possible, minimum bias data are used. As describe in section 3.5.3, high tower trigger events, used to perform the tower–charged correlation, are characterized by an high energy deposit on the BEMC. Therefore, using them to perform a hadron-hadron correlation will imply a three–particle correlation: the two charged hadron, but also the particle activating the trigger. On the other hand, minimum bias trigger does not require any energy deposit on the BEMC and a pure two–particle correlation can be performed.

In d+Au run, the high background affects strongly the BEMC results as seen in section, but the TPC is left unaffected.

The statistic in the minimum bias dataset is lower than high tower trigger dataset, and this leads to a higher uncertainty on the results. Figure 6.11 shows an example of correlation distribution for 5.5< E_T^{trigger} <6.5 GeV.

In figure 6.12, 6.13, 6.14 and 6.15 charged–charged correlation in minimum bias d+Au events is compared to tower–charged correlation in high tower p+p events. The values obtained for charged–charged correlation are also in agreement with previous results [49, 50].

There are some minor discrepancies between p+p tower–charged and d+Au charged–charged correlation in the peak widths that were not present in a previous analysis [50]. Anyway the discrepancies remain within 2 standard deviations and can be considered statistical deviations. On the other side, the yields agree in all the considered energy bins. Since the charged trigger particle are mainly pions, the agreement is expected if the neutral trigger is a pion too.

In [50] the agreement between tower–charged and charged–charged correlation where complete within the same dataset. In the present analysis the comparison made between two dataset (see also section 6.1) shows a good consistency between tower–charged and charged–charged correlation in p+p and d+Au collisions. From the point of view of azimuthal correlation analysis, tower–charged results in p+p collisions can be used to represent also charged-charged results in p+p and d+Au collision. Therefore, the results presented in section 6.3 and 6.4 for tower–charged in p+p collisions are valid

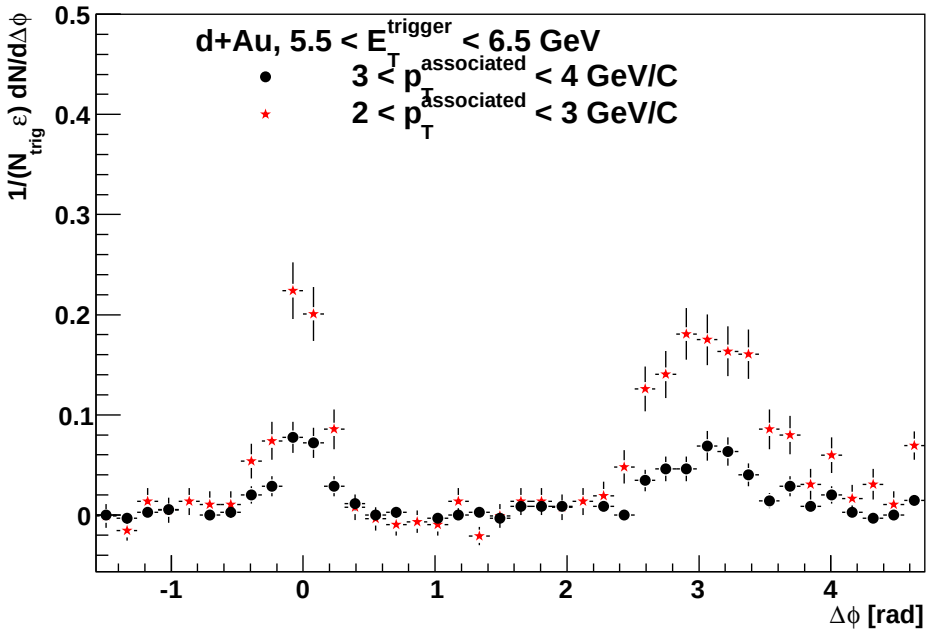

Figure 6.11: Charged pairs azimuthal correlation distribution in d+Au events. The trigger energy is fixed (5.5< E_T^{trigger} <6.5 GeV) and the distribution is plotted for 2< $p_T^{\text{associated}}$ <3 GeV/c and 3< $p_T^{\text{associated}}$ <4 GeV/c.

in general for any hadron–hadron correlation in p+p and d+Au collisions.

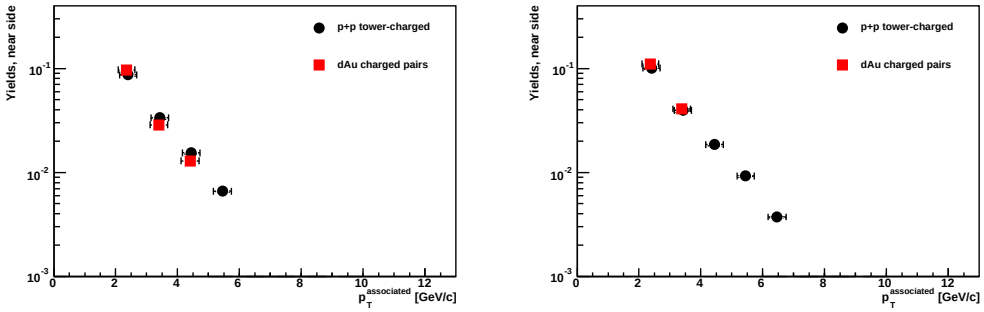

(a) 4.5<E_T^{trig}<5.5 GeV **(b)** 5.5<E_T^{trig}<6.5 GeV

Figure 6.12: Near–side yields. Comparison between charged pairs correlation in minimum bias d+Au events and γ–charged correlation in high tower p+p events for different E_T^{trig} bin.

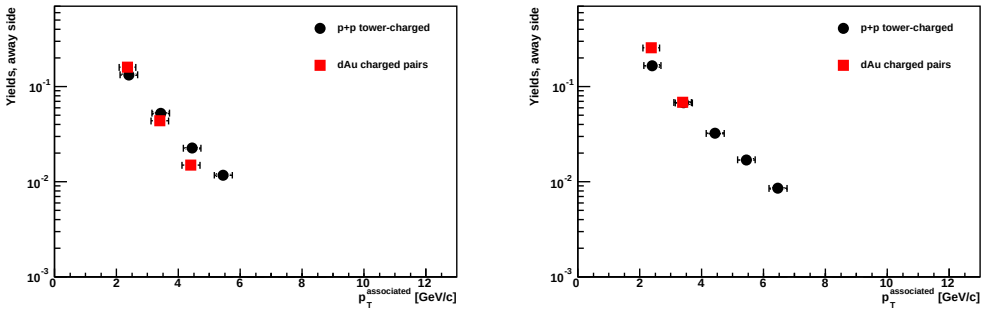

(a) 4.5<E_T^{trig}<5.5 GeV **(b)** 5.5<E_T^{trig}<6.5 GeV

Figure 6.13: Away–side yields. Comparison between charged pairs correlation in minimum bias d+Au events and γ–charged correlation in high tower p+p events for different E_T^{trig} bin.

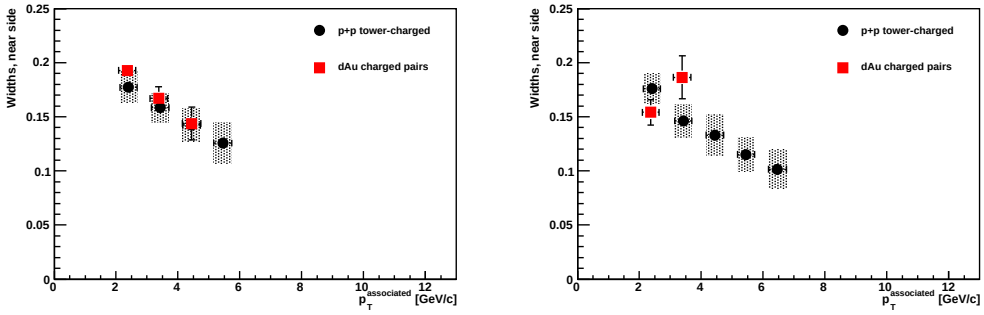

(a) 4.5<E_T^{trig}<5.5 GeV **(b)** 5.5<E_T^{trig}<6.5 GeV

Figure 6.14: Near–side width. Comparison between charged pairs correlation in minimum bias d+Au events and γ–charged correlation in high tower p+p events for different E_T^{trig} bin.

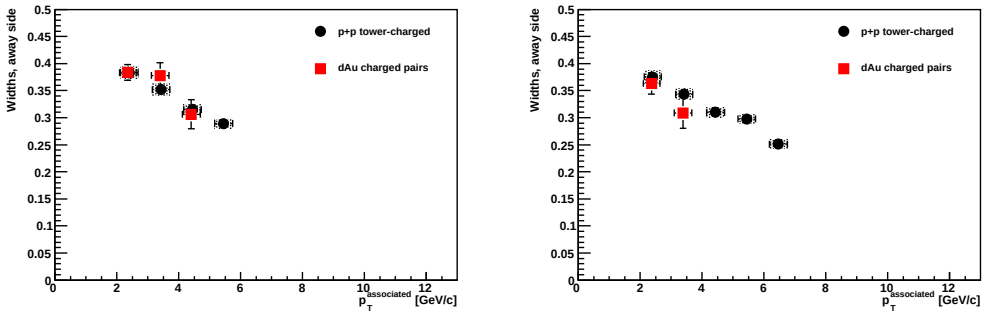

(a) 4.5<E_T^{trig}<5.5 GeV **(b)** 5.5<E_T^{trig}<6.5 GeV

Figure 6.15: Away–side width. Comparison between charged pairs correlation in minimum bias d+Au events and γ–charged correlation in high tower p+p events for different E_T^{trig} bin.

6.3 Intra–jet transverse momentum

The transverse momentum of hadrons with respect to the jet j_T is calculated according to equation (2.14) from the angular widths and yields computed in section 6.1. Previous studies measured values for $\sqrt{\langle j_T^2 \rangle}$ constant for $p_T^{\text{assoc}} > 2$ GeV [51, 29]. Figure 6.16 compares $\sqrt{\langle j_T^2 \rangle}$ values calculated in the present analysis with previous results from the PHENIX experiment [51, 29].

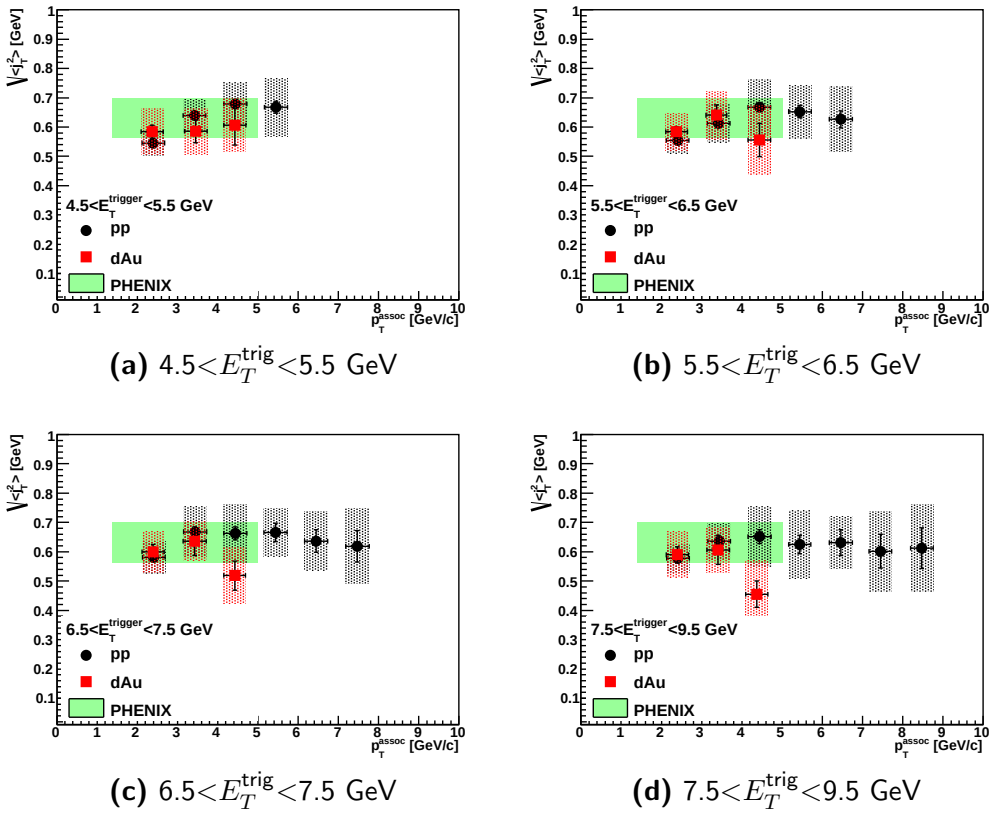

(a) 4.5<E_T^{trig}<5.5 GeV **(b)** 5.5<E_T^{trig}<6.5 GeV

(c) 6.5<E_T^{trig}<7.5 GeV **(d)** 7.5<E_T^{trig}<9.5 GeV

Figure 6.16: $\sqrt{\langle j_T^2 \rangle}$ values calculated according to equation (2.14). The values are compared to the results of the PHENIX experiment [51, 29].

The present analysis agrees with PHENIX results for $1.4 < p_T^{\text{assoc}} < 5$ GeV/c. Moreover it extents the p_T^{assoc} range up to 9 GeV/c. In each E_T^{trig} bin a linear fit performed on the plotted values allows to extract the $\sqrt{\langle j_T^2 \rangle}$ values, as reported in table 6.1. The mean value over E_T^{trig} is

$$\sqrt{\langle j_T^2 \rangle} = 592 \pm 11(\text{stat}) \pm 16(\text{sys}) \text{MeV}/c.$$

This result is in agreement with

$$\sqrt{\langle j_T^2 \rangle} = 585 \pm 6(\text{stat}) \pm 15(\text{sys}) \text{ MeV/c}$$

from [29]. The two results have been obtained with a similar procedure and their consistency is a direct consequence of that.

More interesting is the consistency with the result from [52]

$$\sqrt{\langle j_T^2 \rangle} = 612 \pm 12(\text{stat}) \pm 30(\text{sys}) \text{ MeV/c}.$$

This result has been obtained from a full jet reconstruction, which means that all jet particles have been taken in account and not only the most energetic ones. The agreement of $\sqrt{\langle j_T^2 \rangle}$ values implies that jet widths are well described analyzing only the most energetic particles of a jet.

In the perspective of studying di–jet correlation in Au+Au collisions, it is crucial to link jet properties only to energetic particles because of the difficulty of reconstructing completely a jet in that environment. As seen in section 2.2, only the most energetic jets do not disappear in the medium. In the case of γ–jet correlation the ability to recognize and characterize a jet from its more energetic components becomes even more crucial to allow a comparison with the single photon emitted on the other side.

Trigger energy range [GeV]	$\sqrt{\langle j_T^2 \rangle}$ results [GeV]
$4.5<E_T^{\text{trig}}<5.5$	0.577 ± 0.004
$5.5<E_T^{\text{trig}}<6.5$	0.579 ± 0.004
$6.5<E_T^{\text{trig}}<7.5$	0.611 ± 0.006
$7.5<E_T^{\text{trig}}<9.5$	0.601 ± 0.007

Table 6.1: $\sqrt{\langle j_T^2 \rangle}$ results. For each E_T^{trig} the linear fit on the points obtained for each p_T^{assoc} bin gives value and error for $\sqrt{\langle j_T^2 \rangle}$.

6.4 Jet acoplanarity

Knowing the $\sqrt{\langle j_T^2 \rangle}$ and p_{out} values, equation (2.26) is used to determine the jet acoplanarity κ_T. The results are plotted in figure 6.17 and compared to PHENIX results from [29]. The present work is in agreement with the previous analysis for $p_T^{\text{assoc}}<5$ GeV/c and it extends the results up to $p_T^{\text{assoc}}=9$ GeV. It has been also possible to obtain a more fine dependence on E_T^{trig} in a similar energy range.

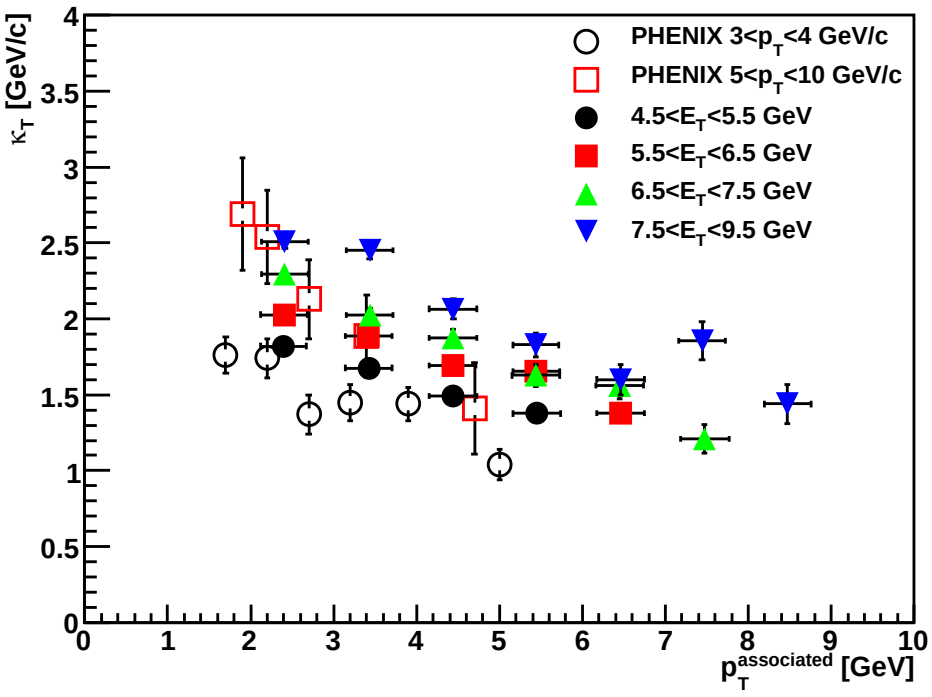

Figure 6.17: Jet acoplanarity κ_T values calculated for different E_T^{trig} ranges. They are calculated according to equation (2.26). Open points are from PHENIX experiment [29].

The p_T^{assoc} dependence of the extracted κ_T values (figure 6.17) reveals a decreasing trend. From the results of [26] it was originally expected that by fixing the value of E_T^{trig}, the kinematics of the hard scattering (i.e. $\hat{p}_T^{\text{near}} \simeq \hat{p}_T^{\text{away}}$) would be fixed, independently of the value of p_T^{assoc}. Various values of p_T^{assoc} would then sample the $\hat{p}_T^{\text{away}}$ fragmentation function, and the value of κ_T was expected to be constant. This assumption can be explained observing that $\langle z_t \rangle$ and $\hat{x}_h$ depends implicity on p_T^{assoc}, but their ratio is roughly $\simeq 1$. It is evident from the results that this assumption is not quite correct. For a fixed E_T^{trig}, κ_T decreases with p_T^{assoc}.

A similar line of argument applies also for the rising trend when p_T^{assoc} is fixed and p_T^{trig} varies. The rising trend of κ_T with $p_T^{\text{trig}}$and falling with p_T^{assoc} suggests that the variation of $\sqrt{\langle k_T^2 \rangle}$ with p_T^{trig} seen by the CCOR collaboration [26] may be indicative of the $\langle z_t \rangle \hat{x}_h^{-1}$ variation which was neglected. The model assumed in [26] hypotizes that x_E, defined as in equation (2.15), is equivalent to the jet fragmentation variable z. More recent

studies proved that this is not the case and thus, that x_E is not sensitive to the fragmentation function [53].

The reason that the x_E distribution is not very sensitive to the fragmentation function is that it is the result of the integration z_t for fixed $p_T^{\rm trig}$and $\vec{p}_T^{\rm assoc}$, which is actually an integral over the jet transverse momentum $\hat{p}_T^{\rm near}$. However since both the trigger and away jets are always roughly equal and opposite in transverse momentum, integrating over $\hat{p}_T^{\rm near}$ simultaneously integrates over $\hat{p}_T^{\rm away}$, and thus also integrates over the away jet fragmentation function.

It has been shown that $\hat{x}_h \simeq 1$ [54] because both the trigger and away jets are always roughly equal and opposite in transverse momentum. Therefore, the behavior of κ_T depends only on the fragmentation function $\langle z_t \rangle$ and the jet smearing $\sqrt{\langle k_T^2 \rangle}$.

Previous analyses measured an opposite trend for the fragmentation variable $\langle z_t \rangle$: it rises with $p_T^{\rm trig}$ and it is falling with $p_T^{\rm assoc}$ [29]. This is a consequence of two effects: competition between steeply falling final state parton spectra and increasing fragment yields with parton momentum. This alone would be sufficient to explain the behavior of κ_T and, as consequence, $\sqrt{\langle k_T^2 \rangle}$ would be independent of both $E_T^{\rm trig}$ and $p_T^{\rm assoc}$.

A more precise conclusion could be drawn only if $\langle z_t \rangle \hat{x}_h^{-1}$ is completely understood and evaluated. Although this goes beyond the goal of the present work, a short overview on a possible approach will be given.

The values of $\langle z_t \rangle$ could be extracted directly from the data [52], but in order to use it for $\sqrt{\langle k_T^2 \rangle}$ calculation one should remember its dependence on $\sqrt{\langle k_T^2 \rangle}$ itself. On the other hand, $\hat{x}_h$ must be evaluated theoretically since it is not possible to measure directly the initial parton behavior. The approach used in [29] proposes to calculate $\langle z_t \rangle$ and $\hat{x}_h$ iteratively, integrating the invariant cross section for inclusive hadron production from jets. The crucial input in this approach is the accurate knowledge reconstruction of the shape of the fragmentation function $D(z)$. This has been done using the Large Electron–Positron Collider (LEP) data [55], where the fragmentation functions of gluon and quark jets were measured in e^+e collisions at $\sqrt{s}$=180 GeV.

The measurement of the fragmentation functions at LEP was done separately for quark and gluon jets and the slopes of these two $D(z)$ distributions are different. Quark–jets produce a significantly harder spectrum than gluon–jets. Since the relative abundance of quark and gluon jets at $\sqrt{s}$=200 GeV is not known, for the final results it has been assumed that the numbers of

quark and gluon jets are equal; the final $D(z)$ uses the averaged parameter values between quark and gluon and the difference can be used as a measure of the systematic uncertainty.

It is important to notice the results obtained with the above method are in agreement with the jet acoplanarity values obtained with a full jet reconstruction approach [52].

Chapter 7

Conclusions and outlook

Azimuthal correlation in di–jet events is a powerful tool to study QGP properties. In particular the focus on γ–jet events allows to measure precisely the energy loss of a jet in the medium. In Au+Au collisions the high multiplicity makes it difficult to have a clear picture of the jet structure. Therefore, it is crucial to characterize jets properly in a much clearer environment, such as p+p and d+Au collisions.

In the present work jets have been studied using the two–particle azimuthal correlation method. In this way the yields and widths of jets have been measured, with a particular emphasis on their dependence on the energy of the particles involved over the entire range in p_T which is aviable at RHIC with present statistics.

The yields increase with the trigger energy and decrease with associated particle momentum. The expectation for di–jet fragmentation predicts the more energetic particles to tag the more energetic jets, which have a higher multiplicity. Also the widths decrease with increasing associated particle momentum, because more energetic particles lie closer to the jet axis.

The correlation distributions' widths have been used to calculate the momentum $\sqrt{\langle j_T^2 \rangle}$ between the trigger particle and the initial parton. Previous experiments proved $\sqrt{\langle j_T^2 \rangle}$ to be constant with the trigger particle energy and the associated particle energy for p_T^{trig} <9 GeV/c and $p_T^{\rm assoc}$<5 GeV/c [29, 51, 52]. The present work extends the limit to $E_T^{\rm trig}$=9.5 GeV * and $p_T^{\rm assoc}$=9 GeV/c and is in agreement with previous works in the overlap region.

For the jet acoplanarity the limit where κ_T is measured have been extended to higher p_T, too. The fragmentation variable z_t must be disentangled from the ratio of the associated parton transverse momentum to the trigger

*In this case the use of the transverse energy is preferable since the trigger is given by photons, hence the energy, not the momentum, is the measured quantity.

parton transverse momentum $\hat{x}_h$ in order to better understand the behavior of κ_T. This procedure require a more deep theoretical approach than the one of the present work.

The aim of the present and previous works [17, 18], is to better characterize the photon emission in p+p collisions. In particular the π^0 and η spectra are analyzed, as well as direct photon spectra. This information could be used together with the present work in order to discriminate γ–jet events from di–jet events.

To study the interactions of jets with the medium via their energy loss it is important to charaterize γ–jet events. Some studies in this direction have already be completed [19]. A better statistic and a better characterization of the detector already allowed a γ–jet analysis to be performed in Au+Au collisions [56]. The information provided by the study of p+p collisions can be crucial to properly understand the properties of the medium produced in heavy–ion collisions.

Summary

The goal of high–energy heavy–ion physics is the full characterization of the quark–gluon plasma (QGP), which is a phase of strongly interacting matter where quarks and gluons are no longer confined in the nucleons and can move freely over longer distances. Such a phase probably existed shortly after the Big Bang, and can be produced in laboratory by heavy–ion collisions at a sufficiently large energy density. This new phase of matter is distinctly different from usual hadronic matter.

Several signatures have been proposed to probe the QGP. The focus of the present work is on jet production. Jets are collimated beams of particles emitted in the collision. The case in which one jet is associated with the emission of a single direct photon (γ–*jet event*) is of particular interest. Photons go through the medium without interacting. For momentum conservation, the energy of the photon is equal to the energy of the initial jet. On the other side, jet particles interact with the medium, losing energy. The energy loss is an important parameter to characterize the medium density.

Due to the high multiplicity in heavy–ion collisions, it is difficult to identify the case of γ–jet production. There are many sources of photons, the most relevant of which is the decay of neutral mesons (mainly π^0 and η). Analyzing the simplest case, that is p+p collisions, gives a necessary baseline measurement for γ–jet correlation studies in Au+Au collisions. This work focuses on di–hadron correlation, seen as a background study for γ–jet correlation. The proprieties of jets in p+p and d+Au collisions are analyzed. In this way, di–jet events are completely characterized, providing a reference frame for the study of γ–jet events.

In the present analysis p+p and d+Au data, collected at the STAR experiment, have been studied. The detectors mainly used are the Barrel Electromagnetic Calorimeter (BEMC) and the Time Projection Chamber (TPC). The BEMC is a lead–scintillator sampling calorimeter located at mid–rapidity ($|\eta| < 1$) and covering the full azimuthal angle. The signals from this detector are used to reconstruct the positions and the energies of the photons. The TPC is used to measure the trajectory and the momentum

of charged particles in the same azimuthal and pseudorapidity range.

The data for d+Au collisions were affected by background due to the interaction of the beam with the material located outside the detector. The first stage of this analysis is the characterization of the background in order to obtain a clean dataset. The second stage consists in calculating the azimuthal correlation distribution of the particles belonging to the jets.

The parameters which describe the jet shape can be extracted from the azimuthal correlation distribution. A differential analysis has been performed to study the dependence of the jet shape on the energy of the particles which compose the jet. In particular, the width of the intra–jet transverse momentum distribution $\sqrt{\langle j_T^2 \rangle}$ has been evaluated.

It is possible to study the relations between the two jets of a di–jet event from the parameters describing a single jet shape. The di–jet acoplanarity $\sqrt{\langle k_T^2 \rangle}$ is measured with an azimuthal particle correlation approach. In this thesis the results for $\sqrt{\langle j_T^2 \rangle}$ and $\sqrt{\langle k_T^2 \rangle}$ have been extended to higher associated particle p_T compared to previous measurements from other experiments, results obtained with charged hadrons and full jet reconstruction. In the overlap region the present results agree with all the previous ones.

The results of the present work constitute a solid baseline for further studies of azimuthal correlation in a high–p_T contest. The use of a neutral trigger is particularly significant in the perspective of γ–jet events studies both in low multiplicity condition, like p+p and d+Au collisions, and more complex systems such as Au+Au collisions.

Samenvatting

Het doel van hoogenergetische zware–ionenbotsingen is het volledig karakteriseren van het Quark–Gluon Plasma (QGP), een fase van quarks en gluonen, de fundamentele deeltjes van de sterke kernkracht, waarin deze niet opgesloten zijn in hadronen, maar vrij kunnen bewegen over langere afstanden. Deze fase, waarin ook het heelal kort na de Oerknal verkeerde, kan in het laboratorium gemaakt worden door met zware–ionenbotsingen een hoge ernegiedichtheid te produceren. Het Quark Gluon Plasma verschilt duidelijk van gewone hadronische materie.

Er zijn verschillende signalen voorgesteld om het QGP te bestuderen. In dit proefschrift ligt de nadruk op jet–productie. Jets zijn gecollimeerde deeltjesbundels die worden geproduceerd in de botsing. Van bijzonder belang zijn botsingen waarin een jet wordt geproduceerd samen met een enkel direct foton (γ–*jet event*). Fotonen bewegen zich door het medium zonder noemenswaardige interacties. Vanwege impulsbehoud is bovendien de transversale energie van het foton gelijk aan die van de jet bij de initiële productie. De jet verliest echter energie tijdens de propagatie door het medium. Dit energieverlies is een belangrijke maat voor de eigenschappen van het medium.

Vanwege het grote aantal deeltjes (multipliciteit) dat in een zware–ionenbotsing wordt geproduceerd, is het moeilijk γ–jet events te identificeren. Er zijn vele andere bronnen van fotonen naast directe fotonen. De voornaamste achtergrond is het verval van ongeladen mesons (vooral π^0 en η). De analyse van p+p botsingen is eenvoudiger en levert een belangrijke referentiemeting voor toekomstige metingen in Au+Au botsingen. In dit proefschrift gaat het vooral om 'di–hadron' correlaties, welke een achtergrond zijn voor γ–jet correlaties. In deze studie worden jets in p+p en d+Au botsingen volledig gekarateriseerd en wordt dus de basis gelegd voor γ–jet metingen.

De metingen voor dit proefschrift zijn verricht met de STAR detector, met name de Barrel Electromagnetic Calorimeter (BEMC) en de Time Project Chamber (TPC). De BEMC is een gelaagde lood–scintillator calorimeter met volledige azimutale acceptantie op mid–rapidity ($|\eta| < 1$). Deze detector

wordt gebruikt om de energie en bewegingsrichting van fotons te meten. De TPC wordt gebruikt om sporen te meten van geladen deeltjes en de impuls te reconstrueren in hetzelfde gebied in azimuth en pseudo–rapidity als de BEMC.

In de d+Au data is een achtergrond aanwezig die veroorzaakt wordt door interacties van de bundel met materiaal buiten de detector. De eerste stap in de analyse is het karateriseren van deze achtergrond om deze te kunnen onderdrukken in de verdere analyse. Vervolgens worden azimutale correlaties berekend voor de deeltjes die van jets afkomstig zijn.

De parameters die de verdeling van deeltjes in de jets beschrijven worden berekend op basis van de gemeten correlaties. Hierbij zijn de metingen tevens verricht als functie van de impuls van de verschillende deeltjes. Met name de breedte van de transverse impulsverdeling binnen de jet $\sqrt{\langle j_T^2 \rangle}$ is bestudeerd.

Het is ook mogelijk om de relaties tussen de twee jets in een di-jet te bestuderen op basis van de jet-verdelingen. Zo meten we de di-jet acoplanariteit $\sqrt{\langle k_T^2 \rangle}$ aan de hand van di-hadron correlaties. De metingen van $\sqrt{\langle j_T^2 \rangle}$ en $\sqrt{\langle k_T^2 \rangle}$ worden in dit proefschrift voortgezet naar hogere p_T dan in vorige metingen met zowel di-hadron correlaties als met volledige jet–reconstructie. Het deel van de resultaten in dit proefschrift dat in hetzelfde kinematische gebied valt, geeft gelijke resultaten als vorige metingen.

Dit onderzoek vormt een gedegen basis voor verder onderzoek met azimutale correlaties van hoog–energetische deeltjes. Vooral het gebruik van de BEMC trigger is belangrijk voor metingen aan γ–jet events, zowel in het geval van lage multipliciteit, zoals p+p en d+Au botsingen, als in Au+Au botsingen, waarvan de hoge multipliciteit een extra complicatie vormt.

Appendix A

First and second moments of normally distributed quantities

Let x be a one–dimensional variable with normal (Gaussian) distribution and $r = \sqrt{x^2 + y^2}$ is a two–dimensional variable with x and y of normal distribution. Then the following relations can easily be derived

$$\begin{aligned} \langle x \rangle &= 0 & \langle r \rangle &= \sqrt{\frac{\pi}{2}}\sigma \\ \langle |x| \rangle &= \sqrt{\frac{2}{\pi}}\sigma & \langle |r| \rangle &= \langle r \rangle \\ \langle x^2 \rangle &= \sigma^2 & \langle r^2 \rangle &= 2\sigma^2 \end{aligned}$$

Both $\vec{j}_T$ and $\vec{k}_T$ are two dimensional vectors. If x and y components are Gaussian distributed, the mean value $\langle k_{T_x} \rangle$ and $\langle k_{T_y} \rangle$ is equal to zero. The non–zero moments of two–dimensional Gaussian distribution are the root mean squares $\sqrt{\langle j_T^2 \rangle}$ and $\sqrt{\langle k_T^2 \rangle}$ or the mean absolute values of the $\vec{j}_T$, $\vec{k}_T$ projections into the perpendicular plane to the jet axes $\langle |j_{T_y}| \rangle$ and $\langle |k_{T_y}| \rangle$. There is a trivial correspondence

$$\sqrt{\langle k_T^2 \rangle} = \frac{2}{\sqrt{\pi}} \langle k_T \rangle = \sqrt{\pi} \langle |k_{T_y}| \rangle. \tag{A.1}$$

Appendix B

Abbreviations and acronims

AGS Alternate Gradient Sincrotron

BBC Beam Beam Counter

BEMC Barrel ElectroMagnetic Calorimeter

CCOR CERN Columbia Oxford Rockefeller (collaboration)

CTB Central Trigger Barrel

DAQ Data Acquisition

DET Detector Brokers

EVB Event Builder

HPPS High Performance Storage System

ISR Intersecting Storage Rings

LEP Large Electron–Positron Collider

pQCD perturbative QCD

QCD Quantum Cromo–Dynamic

QGP Quark Gluon Plasma

RHIC Ring Heavy Ion Collider

SMD Shower Maximum Detector

SPS Super Proton Synchrotron

ABBREVIATIONS AND ACRONIMS

STAR Solenoidal Tracker At RHIC

TPC Time Projection Chamber

ZDC Zero Degree Calorimeter

Bibliography

[1] D. E. Groom et al. Review of particle physics. *Eur. Phys. J.*, C15(1), 2000.

[2] CTEQ Coll. Handbook on perturbative QCD. *Rev. Mod. Phys.*, 67:157–248, 1995.

[3] F. Karsch et al. QCD thermodynamics: The numerical study of strongly interacting matter under extreme conditions. In *NIC Symposium 2001, Juelich, Germany*, December 2001.

[4] W.-M. Yao et al. Review of particle physics. *J. Phys. G 33*, G33(1), 2006.

[5] N. Cabibbo and G. Parisi. Exponential hadronic spectrum and quark liberation. *Phys. Lett.*, B59(67), 1975.

[6] Z. Fodor and S. D. Katz. Lattice determination of the critical point of QCD at finite t and μ. *JHEP*, 03(014), 2002.

[7] R. J. Fries and B. Muller. Heavy ions at LHC: Theoretical issues. *Eur. Phys. J.*, C34:s279s285, 2004.

[8] K. H. Ackermann et al. Elliptic flow in Au+Au collisions at $\sqrt{s_{NN}}$=130 GeV. *Phys. Rev. Lett.*, 86:402407, 2001. nucl-ex/0009011.

[9] M. Gyulassy I. Vitev and X. N. Wang. High–p_t azimuthal asymmetry in noncentral A+A at RHIC. *Phys. Rev. Lett.*, 86:25372540, 2001. nucl-th/0012092.

[10] C. Adler et al. Disappearance of back-to-back high–p_t hadron correlations in central Au+Au collisions at $\sqrt{s_{NN}}$=200 GeV. *Phys. Rev. Lett.*, 90(082302), 2003.

[11] J. Adams et al (STAR Collaboration). Experimental and theoretical challenges in the search for the quark-gluon plasma: The STAR collaboration's critical assessment of the evidence from RHIC collisions. *Nucl. Phys.*, A(757):102.

[12] OPAL experiment. http://opal.web.cern.ch/Opal/welcome.html.

[13] D. Schiff R. Baier and B. G. Zakharov. Energy loss in perturbative QCD. *Ann. Rev. Nucl. Part. Sci.*, 50:37–69, 200.

[14] J. Adams et al. Evidence from d+Au measurements for final state suppression of high–p_t hadrons in Au+Au collisions at RHIC. *Phys.Rev.Lett.*, 91(072304), 2003.

[15] D. Magestro. Direct observation of dijets in central Au+Au collisions with STAR. *Nuclear Physics A*, 774:573–576, 2006.

[16] J. Adams et al. Direct observation of dijets in central Au+Au collisions at $\sqrt{s_{NN}}$=200 GeV. *Phys.Rev.Lett*, 97(162301), 2006.

[17] O. Grebenyuk. *Neutral meson production in d+Au and p+p collisions at $\sqrt{s_{NN}}$ = 200 GeV in STAR.* PhD thesis, NIKHEF and Utrecht University, 2007.

[18] M. J. Russcher. *Direct photon measurement in proton–proton and deuteron–gold collisions.* PhD thesis, NIKHEF and Utrecht University, 2008.

[19] Thomas Dietel. *Azimuthal Correlations of High-p_T Photons and Hadrons in Au+Au collisions at STAR.* PhD thesis, University of Frankfurt, 2006.

[20] J. D. Bjorken S. M. Berman and J. B. Kogut. Inclusive processes at high transverse momentum. *Phys. Rev.*, D4(3388), 1971.

[21] J. F. Owens and J. D. Kimmel. Parton-transverse–momentum effects and the quantum–chromodynamic description of high-p_t processes. *Phys. Rev.*, D18(3313), 1978.

[22] E. Reya J. F. Owens and M. Gluck. Detailed quantum–chromodynamic predictions for high-p_t processes. *Phys. Rev.*, D18(1501), 1978.

[23] G. C. Fox R. P. Feynman, R. D. Field. Quantum–chromodynamic approach for the large–transverse–momentum production of particles and jets. *Phys. Rev.*, D18(3320), 1978.

[24] G. Bunce et al. Prospects for Spin Physics at RHIC. *Ann.Rev.Nucl.Part.Sci.*, pages 525–575, 2000. hep-ph/0007218v1.

[25] D. Sivers R. Cutler. Quantum–chromodynamic gluon contributions to large–p_T reactions. *Phys. Rev.*, D(17):196–211, 1978.

[26] A. L. S. Angelis et al. (CERN-Columbia-Oxford-Rockefeller). A measurement of the transverse momenta of partons, and of jet fragmentation as a function of $\sqrt{s}$ in p+p collisions. *Phys. Lett.*, B97(163), 1980.

[27] K. Adachi et al. (TOPAZ). Measurement of the jet width in $\gamma\gamma$ collisions and in e+e – annihilation process at TRISTAN. *Phys. Lett.*, B451(256), 1999.

[28] S. Eidelman et al. (Particle Data Group). Review of particle physics. *Physics Letters*, B592(1), 2004,2005,2006.

[29] S.S. Adler et al. (PHENIX collaboration). Jet properties from dihadron correlations in p+p collisions at $\sqrt{s_{NN}}$=200 GeV. *Phys.Rev.*, D74(072002), 2006.

[30] M. Della Negra et al. (CERN-College de France-Heidelberg-Karlsruhe). Observation of jet structure in high p_t events at the ISR and the importance of parton transverse momentum. *Nucl. Phys.*, B117(1), 1977.

[31] G. C. Fox R. P. Feynman, R. D. Field. Correlations among particles and jets produced with large transverse momenta. *Nucl. Phys.*, B128(1), 1977.

[32] K.H. Ackermann et al. STAR detector overview. *Nuclear Instruments and Methods in Physics Research*, A499:624632, 2003.

[33] PHENIX experiment. http://www.phenix.bnl.gov/.

[34] PHOBOS experiment. http://www.phobos.bnl.gov/.

[35] BRAHMS experiment. http://www4.rcf.bnl.gov/brahms/WWW/.

[36] M. Anderson et al. The STAR time projection chamber: a unique tool for studying high multiplicity events at RHIC. *Nucl. Instrum. Methods Phys. Res.*, A499:659678, 2003.

[37] M. Beddo et al. The STAR Barrel Electromagnetic Calorimeter. *Nucl. Instrum. Methods Phys. Res.*, A 499:725–739, 2003.

[38] R. Bellwied et al. The STAR Silicon Vertex Tracker: A large area Silicon Drift Detector. *Nucl. Instrum. Methods Phys. Res.*, A 499:640–651, 2003.

[39] L. Arnold et al. The STAR silicon strip detector (SSD). *Nucl. Instrum. Methods Phys. Res.*, A 499:652–658, 2003.

[40] C. E. Allgower et al. The STAR endcap electromagnetic calorimeter. *Nucl. Instrum. Methods Phys. Res.*, A 499:740–750, 2003.

[41] K. H. Ackermann et al. The forward time projection chamber in STAR. *Nucl. Instrum. Methods Phys. Res.*, A 499:713–719, 2003.

[42] F.S. Bieser et al. The STAR trigger. *Nuclear Instruments and Methods in Physics Research*, A499:766777, 2003.

[43] F. Sauli. Principles of operation of multiwire proportional and drift chambers. Technical Report CERN 77-09, CERN, 1977.

[44] J. M. Landgraf et al. An overview of the STAR DAQ system. *Nuclear Instruments and Methods in Physics Research Section A*, 499(2-3), 2003.

[45] Thomas Dietel. Energy resolution. In *Azimuthal Correlations of High-p_T Photons and Hadrons in Au+Au Collisions at STAR* [19], chapter 5.3.2.

[46] Thomas Dietel. Correction of track veto cut. In *Azimuthal Correlations of High-p_T Photons and Hadrons in Au+Au Collisions at STAR* [19], chapter 5.5.3.

[47] Torbjorn Sjostrand et al. High–energy–physics event generation with PYTHIA 6.1. *Comput. Phys. Commun.*, 135:238259, 2001. hep-ph/0010017.

[48] Subhasis Chattopadhyay Jana Bielcikova. Private comunication.

[49] Jana Bielcikova. Private comunication.

[50] F. Benedosso. Jet properties from two-particle azimuthal correlations in d+Au collisions at $\sqrt{s_{NN}}$=200 GeV at STAR. *Eur. Phys. J. C*, 49(1):61–64, 2006.

[51] S.S. Adler et al. (PHENIX collaboration). Jet structure from di-hadron correlations in d+Au collisions at $\sqrt{s_{NN}}$=200 GeV. *Phys.Rev.*, C73(054903), 2006.

[52] Thomas William Henry. *Reconstruction and attributes of jets observed in $\sqrt{s}$=200 GeV proton–proton and deuteron–gold collisions at STAR.* PhD thesis, Texas A&M University, 2006.

[53] M. J. Tannenbaum. Why the x_E distribution triggered by a leading particle does not measure the fragmentation function but does measure the ratio of the transverse momenta of the away–side jet to the trigger–side jet. In *19^{th} International Conference on Ultra–Relativistic Nucleus–Nucleus Collisions*. Quark Matter, 2006. nucl-ex/0702037v1.

[54] Michael J. Tannenbaum. Review of hard scattering and jet analysis. In *Correlations and Fluctuations in Relativistic Nuclear Collisions*, Florence, Italy, 2006. nucl-ex/0611008v2.

[55] P. Abreu. et al. Measurement of the gluon fragmentation function and a comparison of the scaling violation in gluon and quark jets. *Eur. Phys. J.*, C13:573–589, 2000.

[56] Ahmed M. Hamed. Direct photon-charged hadron azimuthal correlations. arXiv:0806.2190v1 [nucl-ex].